Politecnico di Torino

Corso di Laurea Magistrale
in Ingegneria Aerospaziale

Tesi di Laurea Magistrale

Design and Performance Measurements of a Long Channel Hall Thruster for Air-Breathing Electric Propulsion

Relatori
Prof. Lorenzo Casalino, Politecnico di Torino
Prof. Mark A. Cappelli, Stanford University

Candidato
Francesco Marchioni

Anno Accademico 2019-2020

“Remember to look up at the stars and not down at your feet. Try to make sense of what you see and wonder about what makes the universe exist. Be curious.”

- Stephen Hawking

A mio nonno.

Abstract

The focus of this research is to introduce, design and measure the propulsive performance of a long channel Hall thruster concept to enable the efficient use of molecular propellants for electric propulsion. In order to do so the research addresses the issues faced with air-breathing electric propulsion, highlighting both the benefits and limitations of this prospective technology.

In order to devise effective modifications, the properties of molecular propellants are explored and compared to typical options for electrostatic propulsion, such as xenon. In particular, the disadvantages of these propellants are addressed, principally residing in a reduction of ionization rate as a result of higher first ionization energy, lighter mass and possibility of dissociative reactions.

Having identified the characteristics of molecular propellants, design modifications were presented and explained, entailing a longer ionization chamber encompassing an extended magnetic field peak, with the principal focus of enhancing ionization and increasing neutral residence time. This design was modelled and simulated, then tests were conduced in Stanford's Large Vacuum Facility to validate the findings. The thruster was mounted on a thrust stand, which allowed for immediate thrust measurements, and operated on a pure nitrogen flow.

The results demonstrate the effectiveness of these modifications, as a stable plasma discharge was maintained on pure nitrogen. Analysis of the results showed a substantial performance improvement when compared to shorter channel thrusters running on molecular propellant mixtures. Encouraging positive trends were noticed when magnetic filed density was increased, highlighting the importance of electron confinement. The low efficiencies measured illustrate the still inadequate ionization region length when compared to nitrogen mean free path, incentivising further optimization and channel extension.

Acknowledgments

Vorrei esprimere i miei più sentiti ringraziamenti al Professor Casalino cui devo il merito di avermi fatto appassionare alla propulsione spaziale e al Professor Cappelli per il suo entusiasmo travolgente, per le mille idee innovative e per i consigli preziosi che mi ha dispensato. Un grazie particolare, inoltre, per avermi accolto nel suo laboratorio concedendomi una fantastica, inattesa opportunità. Ringrazio entrambi i Professori per il sostegno e la fiducia che mi è stata accordata.

Un grazie a tutto il team dello Stanford Plasma Physics Lab: Andrea, Fabio, Will, Adura, Taemin e tutti gli altri. Ho avuto la fortuna di conoscere tante persone fantastiche e disponibili che mi hanno accolto da subito e con cui è stato un piacere collaborare. Un ringraziamento particolare vorrei dedicarlo ad Andrea che, nonostante fosse diventato padre, ha trovato sempre il tempo per risolvermi dubbi e incertezze e a Fabio, i cui consigli preziosi sono secondi solo alle sue feste.

In questi mesi ho avuto la fortuna di conoscere e rincontrare: Alberto, Edoardo, Lukas, Francesco con le quali ho sviluppato e consolidato una profonda amicizia. Con loro mi sono trovato sempre a casa, anche tra i deserti della Death Valley e i casinò di Las Vegas. Voglio ringraziarli, non solo per feste cui mi hanno portato, ma anche per le volte che hanno cucinato la pizza quando più avevo nostalgia di casa, oltre che per i viaggi in Uber alle 4 di mattina e per tutti i momenti che hanno reso questo viaggio indimenticabile.

Inoltre, un immenso grazie va tutti i miei amici italiani: Andrea, Luca, Alberto, Francesco, Alessandro, Josef e tutti gli altri, ci vorrebbe una seconda tesi solo per citarli tutti. Anche da lontano, non hanno mai smesso di sostenermi e fare il tifo per me. Li ringrazio per le mille avventure passate insieme, i mille viaggi in giro per il mondo ma soprattutto per avermi spronato a dare sempre il meglio. Un grazie a Martina per esserci sempre, con gli infiniti passaggi in macchina, gli aperitivi, le telefonate ed i mille messaggi.

Il ringraziamento più grande di tutti va alla mia famiglia. A mia madre e mio padre che hanno creduto in me in questi anni pieni di gioia e sforzi, che mi hanno dato la possibilità di fare questa meravigliosa esperienza e che si sono sempre fidati di me. Un grazie a mia sorella e alle mie nipotine, Caterina e Sofia, la cui gioia mi riempie il cuore ogni volta che le vedo. Un grazie ai miei zii e cugini per l'immancabile sostegno, le risate e le cene infinite. Un ultimo grazie va ai miei nonni, a mia nonna per l'infinito affetto che mi da e a mio nonno, il cui ricordo rimane indelebile.

Motivation and objectives

Orbiting at Very Low Earth Orbit (VLEO) altitudes represents both a great opportunity and an extreme challenge. Such extreme altitudes would benefit resolution, signal latency and reduce transmission power requirements, ideal aspects for satellite based internet services and Earth observation. Lower altitudes also signify faster orbits therefore the possibility of passing over a desired target more times per day and with better image resolution, essential for military intelligence. Orbiting at such low altitudes would also provide the means for in situ measurements of atmospheric properties such as density or chemical composition, an aspect of growing importance in determining the effects of climate change.

These benefits however, are inaccessible to modern technology, as such extreme low altitudes (below 300 kilometers) are characterized by an atmosphere too dense for non-propelled orbits, yet not dense enough for conventional jet engines. The use of traditional space thrusters to provide thrust would entail unfeasibly big propellant tanks, it is clear that new designs, capable of harvesting in situ resources, must be engineered.

The concept of air-breathing electric propulsion would allow dedicated systems to operate at VLEO altitudes for prolonged periods through continuous drag compensation and account for a noticeable reduction in tank and propellant weights and costs. This task is achieved via a specifically designed system composed of an air intake, which would collect residual atmospheric particles to serve as propellant, and an electric thruster, responsible for the ionization and acceleration of the collected propellant to guarantee continuous drag compensation.

Inspired from the works of Andreussi et al [1], in which a representative VLEO environment has been reproduced and used to test a primitive air-breathing concept system, this research has concentrated on the possibility of optimizing a Hall thruster design to enhance performance when operating with molecular propellants. In addressing this concept, a feasibility study conducted by Davina et al [2] on behalf of the European Space Agency (ESA), has identified the following issues that must be investigated in order for the correct and efficient functioning of air-breathing technology:

1. Capability to collect the mass flow rate needed to generate the required thrust with an inlet aperture of size compatible with the dimensions of a reference spacecraft;
2. Capability to collect the particles flow with properties as required by the thruster;
3. Choice of an Electric Propulsion thruster that guarantees the required thrust to perform altitude compensation;
4. Capability of the thruster to work with the encountered flow mixture composition or with selected species;
5. Capability of the thruster to work with variable inlet conditions caused by different altitudes, solar activities, local time;

6. Capability of the thruster to operate within the power and mass constraints of a typical Earth observation mission.

The objective of this research is to provide initial solutions to the third and fourth points identified by the ESA report, therefore the capability of the electric thruster to correctly function with molecular propellants present in the atmosphere and produce required amounts of thrust at VLEO altitudes, in the hopes of making this technology feasible in a near future.

Throughout this study, the possibility and limitations of using molecular propellants for Hall thrusters shall be explored. Through dedicated models and simulations the performance and behaviour of these propellants will be analysed.

As a result of the simulations, specific design modifications aimed at optimizing the performance of Hall thrusters operating on molecular propellants shall be designed, simulated and ultimately tested. The performance of a new modified long channel Hall thruster shall be measured in order to explore the feasibility of the air-breathing electric propulsion concept.

A different use of molecular propellants for electric thrusters other than VLEO missions is the concept of a hybrid dual-propulsion rocket for deep space exploration. This technology would entail a high-thrust liquid rocket for launch and orbit injection and a high specific impulse N_2 optimized electric thruster for in-space propulsion. This system would exploit a shared propellant storage as molecular nitrogen is the major constituent and by-product of hydrazine, a common fuel for chemical rockets.

Structure of the thesis

In order to effectively design and present the results and performance of a long channel Hall thruster, this study has been divided in seven chapters. Chapter 1 introduces the fundamental concepts of electric propulsion, as well as the basics of plasma theory. Chapter 2 shall concentrate on the workings and design of typical Hall thrusters, introducing the governing equations that shall be used to evaluate the performance. Chapter 3 introduces the use of molecular propellants for electrostatic propulsion, weighing their benefits and disadvantages and evaluating their performance through simulations and previous experiments. Further emphasis shall be placed on atmospheric modelling and orbit optimization for air-breathing electric propulsion mission concepts. Chapter 4 explores the design modifications to enhance Hall thruster performance on molecular propellants, followed by simulations and models to estimate the benefits of these adaptations. Chapter 5 introduces the experimental facility and codes used to acquire and analyse the data during thruster operation. Finally, in chapters 6 and 7 the results shall be presented and discussed. Comparisons to previous experiments shall be made and errors analysed in order to pave the way for future works and further optimization with the hopes of making this technology feasible.

Contents

List of Figures

List of Tables

Concepts of Propulsion

1.1 Introduction to propulsion

1.1.1 Principles of thrust

Propulsion is the act of changing the motion of a body with respect to an inertial reference frame. Propulsive systems, as such, provide forces that are capable of moving bodies initially at rest, changing their velocity or overcoming external forces [3].

It is with this goal, that numerous propulsive systems have been devised over the years, technologies capable of lifting a spacecraft from ground and propelling it to the depths of space. These technologies all rely on the same fundamental principle, internally accelerating and expelling a certain amount of mass, or propellant, to gain velocity exploiting Newton's laws of dynamics.

A simple explanation to this phenomenon can be obtained considering an isolated system, comprised of a mass (m) travelling at a constant speed (v), as illustrated in Figure 1.1.

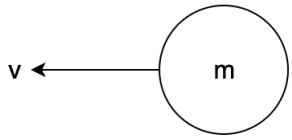

Figure 1.1: Mass travelling at a constant speed

In order to accelerate the spacecraft, the thruster must expel a certain quantity of propellant (dm_p) with a certain exit speed (c), greater than the spacecraft's initial speed (v), this will cause an increase in velocity (dv), as demonstrated in Figure 1.2.

Having considered an isolated system, thus in the absence of external forces, it is possible to apply the momentum conservation equation:

$$mv = (m - dm_p)(v + dv) - dm_p(c - v) \tag{1.1}$$

Simplifying the expression:

$$mdv = dm_p c \tag{1.2}$$

Figure 1.2: Ejection of propellant and increase in speed

This expression considers a discrete expulsion of propellant, in order to account for a continuous ejection the *mass flow rate* of propellant ($\dot{m}_p$) can be introduced by dividing the above equation by time (dt).

$$T = m\frac{dv}{dt} = \dot{m}_p c \tag{1.3}$$

It is immediate to observe that the left hand side resembles Newton's second law of dynamics, therefore representing a force, or *Thrust*, generated by accelerating and expelling a flow of propellant.

This definition neglects the effect of a pressure differential between the inside of the thruster and the outside environment ($A_e(p_e - p_o)$). This is valid for space propulsion systems operating in a vacuum and maintaining a very low internal pressure to facilitate plasma discharge. Such a hypothesis is also valid during testing as these thrusters are operated in high quality vacuums. However, as shall be explained throughout the study, this equation is no longer correct for air-breathing propulsion, in which the propellant is no longer initially at rest but already travelling at an initial speed relative to the spacecraft and correction of the above equation is necessary.

Another key parameter to consider when characterising performance is the *Specific Impulse* (I_{SP}). This allows to quantify effectiveness of propellant usage and facilitates comparison between different classes of thrusters as a result of the scaling of thrust with the weight, at sea-level ($g_0 = 9.81 m/s^2$), of propellant used. It is defined as:

$$I_{SP} = \frac{I_T}{m_p g_0} \tag{1.4}$$

In which the *Total Impulse* (I_T) is defined as the integral of thrust during the thrusters' total activation time:

$$I_T = \int_0^t T dt \tag{1.5}$$

Moreover, considering a constant thrust during operation, which is a valid approximation especially for electric thrusters, the above expression can be simplified to:

$$I_T = T\Delta t \tag{1.6}$$

Substituting this expression in (1.4) and considering both thrust and mass flow rate con-

stant:

$$I_{SP} = \frac{T\Delta t}{\dot{m}_p \Delta t g_0} \tag{1.7}$$

Finally, substituting (1.3) in the above equation, a direct relation between specific impulse and exhaust velocity is observed:

$$I_{SP} = \frac{c}{g_0} \tag{1.8}$$

These are the principle parameters, along with the efficiencies that shall be later discussed, with which the propulsive performance of thrusters can be evaluated.

1.1.2 Thruster classification

A useful insight to distinguish the various propulsive technologies can be achieved by introducing the kinetic power of thrust:

$$P_T = \frac{1}{2}\dot{m}_p c^2 = \frac{Tc}{2} \tag{1.9}$$

The source of such power, which generates the acceleration of propellant, allows us to discern the fundamental engines in space propulsion [3]:

- Chemical: energy from the combustion reaction of chemical propellant is used to heat gasses, this thermal energy is then converted into kinetic energy by a nozzle.
- Electrothermal: similar to chemical, gasses are heated and accelerated through a nozzle, in this case however, thermal energy is produced by passing a current through the propellant, thus exploiting the Joule effect.
- Electrostatic: the neutral propellant is first ionized, then the ions are accelerated by electric fields and expelled at very high velocities.
- Electromagnetic: similarly a plasma is created, accelerated through electric and magnetic fields and expelled at high velocities and specific impulses.

Examples of different thruster technologies and their performances are reported in Table 1.1. For space propulsion, thrust is needed to propel a spacecraft carrying a payload, to

Thruster type	Specific Impulse (s)	Input Power (kW)	Efficiency (%)	Typical propellant
Chemical (monopropellant)	150-225	-	-	N_2H_4, NH_3
Chemical (bipropellant)	300-450	-	-	$LO_2 + H_2, LO_2 + RP1$
Resistojet	300	0.5-1	65-90	N_2H_4, NH_3
Arcjet	500-600	1-2.5	25-45	N_2H_4, NH_3
Ion thruster	2500-6000	0.5-4.5	40-80	Xe, Ar, Kr
Hall thruster	1500-2000	0.5-4.5	35-60	Xe, Ar, Kr
PPT	850-1200	<0.2	7-13	Teflon
MPD	2000-5000	100-1000	30-50	Ar, Xe, H_2, Li

Table 1.1: Summary of the main propulsive technologies [4]

a destination. In such way the mission objective determines the velocity increment, or Δv, requirement to escape Earth's gravitational field and reach the desired destination. This Δv can be associated to the minimum theoretical propellant needed to achieve such mission through the *Tsiolkovsky's rocket equation*:

$$\Delta v = c \ln \left(\frac{m_0}{m_f} \right) \tag{1.10}$$

Tsiolkovsky's equation presents an exponential relation between Δv and propellant, this greatly hinders the mission's achievability within a reasonable amount of fuel. It is therefore paramount that, to minimise the propellant required, exhaust velocities (c) are the highest possible, providing the *raison d'être* for electric propulsion [5].

Since the beginning of the 20th century, chemical rockets have been the primary choice for space propulsion, having reached high levels of performance and providing fairly simple technology to generate high thrust-to-mass ratios necessary to lift from ground [6].

As exploration progresses and humankind craves new knowledge, missions with growing Δv's are required, thus the burden of thrust generation must shift from high rates of ejection of propellant mass to greater exhaust velocities. Chemical rockets are intrinsically hindered by the combustion reaction and material heat tolerances to exhaust speeds of a few thousand meters per second, too low for many proposed modern day missions, some fundamentally different concepts, relying on new technologies for the acceleration of propellant mass, are required [7].

1.2 Electric propulsion

1.2.1 History of electric propulsion

As of 2019, over 500 spacecrafts propelled by electric thrusters operate throughout the solar system [8]. Yet the history of electric propulsion starts more than a century earlier, when space travel was no more than a mere dream. In 1911, one of the earliest pioneers of rocketry, Konstantin Tsiolkovsky, envisioned the use of electricity to accelerate particles to speeds greater than those achieved by the ordinary products of combustion. Having derived the *rocket equation*, he, above all, understood the significant advantages of exhaust velocity on propellant consumption [9].

Tsiolkovsky's pioneering deductions on the propulsive use of charged particles and electricity were later extrapolated and elaborated by American scientist and inventor, Robert Goddard. Goddard, unlike his predecessor Tsiolkovsky, possessed a solid theoretical and practical background in the field of electromagnetism. This allowed him to investigate the physics behind such form of propulsion, ultimately culminating in his patented work entitled "Method of and means for producing electrified jets of gas" [10]. In such work Goddard produces the world's first documented electrostatic ion accelerator for propulsive

purposes [5], a representation of his work can be seen in Figure 1.3. Goddard states, referring to the charged particles, that: *"These velocities are the greatest that have yet been produced in any way with masses of gas of appreciably large magnitude"*.

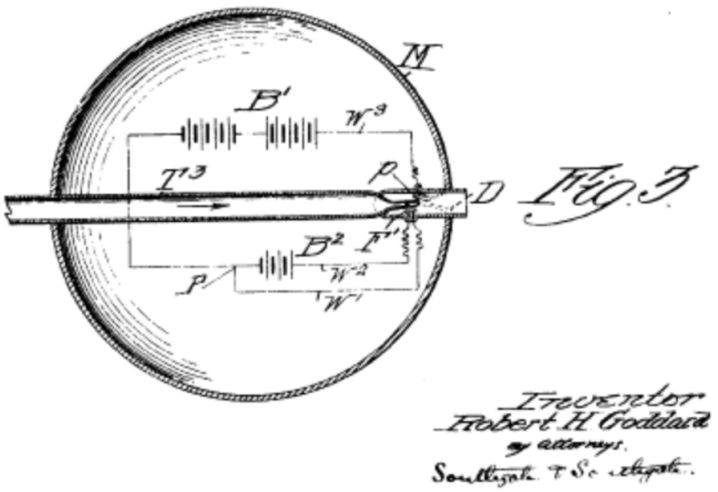

Figure 1.3: Schematic of Goddard's ion accelerator, patented in 1917 [10]

It was Hermann Oberth, German engineer and pioneer, who first unambiguously defined electric propulsion as a plausible and worthy pursuit in astronautics. In his 1929 work on astronautics and spaceflight [11], he dedicated an entire chapter, titled *Das elektrische Raumschiff* (The electric spaceship) envisioning the mass saving advantages and capabilities for in-space propulsion this technology would have in the future [5].

In order to appreciate the first technological developments of electric propulsion space enthusiast had to wait until 1964, year in which Ernst Stulinger, inspired by the proclamations of his aforementioned predecessors, published a thorough design of an ion engine, in his work "Ion Propulsion" [12].

That same year the first electrically propelled spacecraft, the SERT-1 (Space Electric Rocket Test), was successfully launched and tested. Unlike the failed test two years earlier, it's Gridded Ion Engine ran for a total of 31 minutes and 16 seconds after having been lifted to a 4000km ballistic orbit on a scout rocket [13]. This marked a milestone for electric propulsion, demonstrating the feasibility and readiness of such technology and paved the way for perhaps the most iconic of electrically propelled space missions to date, Deep Space 1 in 1998, propelled by the NSTAR Gridded Ion Engine to the flyby of the 9969 Braille asteroid.

Meanwhile, on the other side of the Iron Curtain, far from the eyes of the western world that had previously discarded it, Hall Effect technology thrived. Scientists and engineers in the USSR were actively designing functioning models of HETs, with promising efficiencies as high as 50% [14]. In 1971, the Institute of Atomic Energy, together with the bureau

"Fakel" and the All-Union Scientific Research Institute of Electromechanics successfully tested and launched the first Hall Thruster propelled satellite, the Meteor-18 [15]. This was followed by 118 Hall thruster propelled missions in the two following decades [16], consolidating Soviet leadership in such technology.

It wasn't until the fall of the Soviet Union, that information on such major progress in Hall Effect propulsion was divulged to the western world as teams of European and American scientists flew to the now Russian Federation to visit their laboratories. As the US and Europe realized the functionality and advantages of this technology, numerous companies, such as SNECMA and Loral struck deals with former Soviet aerospace industries to exploit such innovative technology.

1.2.2 Principles of electrostatic propulsion

The primary attraction of electric propulsion lies in the efficient utilization of propellant mass. Such a reduction in propellant supply allows for greater payloads to be transported to greater distances thanks to the achievement of exhaust velocities inaccessible to chemical rockets [17].

As common to all propulsive efforts, in order to generate thrust, a mass must be accelerated and expelled. Contrary to classical chemical rockets however, in which a nozzle converts thermodynamic energy to kinetic energy, the desired acceleration is now generated as a result of electromagnetic body forces. Such forces allow for the ejected particles to attain speeds far greater than in their chemical predecessors. Therefore, as clearly stated in Equation (1.10), missions requiring Δv's previously unattainable, would now result plausible.

Hence in electric thrusters, differently from chemical rockets, the power is external to the propellant, supplied by a source or generator. Such source must be capable of providing the required power for the whole duration of the mission, a typical solution for space applications are solar panels and possibly in some near future, nuclear reactors. These power source however, are heavy and largely inefficient, it is therefore evident that these pose strong limitations to the effectiveness of this propulsive principle. The evolution of this technology has been hindered by the frustrating lack of high levels of electric power in space [5].

A generic electric thruster technology must convert electrical energy, provided by the power source, into kinetic energy as the flow of propellant ($\dot{m}_p$) is accelerated. A preliminary power balance, accounting for generic losses (η), can be made:

$$\eta P_E = \frac{1}{2}\dot{m}_p c^2 \tag{1.11}$$

It is therefore possible to express the exhaust velocity in electric thrusters:

$$c = \sqrt{2\eta \frac{P_E}{\dot{m}_p}} \tag{1.12}$$

It is important to notice that, albeit increasing the exhaust velocity, directly related to the specific impulse as described by Equation (1.8), results in a reduction of propellant consumption, there is an optimal value of (c), or specific impulse, deriving from the power supply weight penalty.

In order to better visualize this concept, the total mass of the spacecraft (m_t) can be divided in three elements: the payload (m_u), power source (m_s) and propellant (m_p).

$$m_t = m_u + m_p + m_s \tag{1.13}$$

Given a fixed total mass, generally as a constraint of the launch vehicle, the goal is to maximise the payload fraction. An increase in the exhaust speed results not only in a reduction of mass of propellant, but also in the increase of power (P_E) required to accelerate the propellant, which inevitably leads to heavier power sources. It follows that there is an optimum value for specific impulse, or exhaust speed, determined by each mission.

Workings of electric thrusters

A charged particle in an electric field is affected by the *Coulomb force*, this is responsible for the acceleration of the particle parallel to field lines. The direction of motion depends on the particle's charge, if positive, therefore an ion, it will be concordant to the field, vice versa, if it's an electron, it will move opposite to the field.

The velocity of a charged particle in an electrostatic field can be obtained immediately. Applying a potential difference between an anode (V_A) and a cathode ($V_C < V_A$), it is possible to calculate the velocity of a charged particle by observing the energy balance:

$$\frac{1}{2}m_i v_A^2 + qV_A = \frac{1}{2}m_i v_C^2 + qV_C \tag{1.14}$$

Considering the particle initially at rest ($v_A = 0$) it is possible to obtain the velocity as a result of the acceleration between a potential difference:

$$v = \sqrt{2\frac{q}{m}\left(V_A - V_C\right)} \tag{1.15}$$

In order to generate thrust, it is fundamental that all the charged particles accelerate and are ejected in a net direction. It is evident that accelerating both ions and electrons in an electric field, would result in no net force acting on the thruster.

Therefore, to assure the generation of thrust, it is fundamental to apply a potential difference in a region populated by charged particles, yet accelerate and eject only one desired charge, for such, the workings of an electrostatic thruster can be divided in three separate stages:

1. Ionization:
   In order to obtain charged particles, an initially neutral propellant must be ionized to

generate a *plasma*. This quasi-neutral state of matter consists of positively charged ions and negatively charged electrons, susceptible to the electric field. Such ionization is obtained by providing a certain amount of energy, called *ionization energy* (ε_i), to the atom. This level of energy excites the outer electron enough to separate it form the atom, leaving a positively charged ion behind.

2. Acceleration:
   Once the atom is ionized, it consists of charged particles which, as stated earlier, are susceptible to an electric field, therefore applying a potential difference would result in the desired acceleration of the ionized propellant. However, in order to generate thrust it is fundamental to accelerate and eject only one species of charged particles. For propulsive reasons, which shall be elucidated shortly, only ions are ejected, whereas the electrons remain trapped in the thruster. In a Hall thruster, this selection is achieved by the addition of a magnetic field ($\overrightarrow{B}$), the details of such procedure will be thoroughly analysed in the following section.

3. Neutralization:
   Having accelerated and expelled the ions, it is fundamental to neutralize the ion beam by ejecting the same number of opposite charged particles, or electrons. If this were not done, the expulsion of only positive charges would result in the thruster acquiring a negative charge and the ions be attracted back inside the thruster, cancelling the propulsive effect.

Having briefly explored the principles of electrostatic propulsion, it is possible to introduce some preliminary considerations. In order to ionize the propellant, a certain amount of energy must be supplied to the atom, at least equal to its ionization energy, called *ion production cost* (ε_b). Therefore not all of the energy supplied accelerates the propellant, it is possible to express this concept by defining an *ideal efficiency*, considering the achieved kinetic energy of the accelerated ion and the total energy input:

$$\eta_{ID} = \frac{\frac{1}{2} m_i v_i^2}{\frac{1}{2} m_i v_i^2 + \varepsilon_b} \tag{1.16}$$

Dividing by the kinetic energy:

$$\eta_{ID} = \frac{1}{1 + \frac{2\varepsilon_b}{m_i v_i^2}} \tag{1.17}$$

To maximise this ideal efficiency, the ion production cost (ε_b) must be low, therefore the propellants must be easily ionizable, and the mass of the accelerated particle must be high, typical choices are Xenon and Argon. An electron weighs at least 10^3 times less than an ion, for such reason ions are accelerated instead of electrons.

A final consideration can be made, observing that the exhaust speed (v_i) cannot be chosen arbitrarily in order to maximise the efficiency. In fact it is related directly to the specific impulse, which is optimized for each mission as a result of the power supply penalty. This exhaust speed impacts the ideal efficiency, It becomes evident therefore that electrostatic propulsion is efficient only for missions requiring high specific impulses.

1.3 Introduction to plasma physics

1.3.1 Properties of plasma

Electric thrusters achieve thrust by accelerating charged particles through electromagnetic field, it is therefore evident that this technology relies fundamentally on the generation of a *plasma* through the ionization of propellant. Plasma is often referred to as the fourth state of matter, accounting for over 99% of the known matter in the universe. It occurs when atoms constituting the gas have been energized to such an extent that at least one of the negatively charged electrons are stripped from the atom, leaving behind a positively charged ion. A vacuum must be present to efficiently sustain a plasma discharge as in the presence of air, the plasma would cool and the ions and electrons would recombine. For such reason plasma is vastly present in the universe, yet our experience of it on Earth is limited.

Plasma is defined as *a quasi-neutral gas of charged and neutral particles which exhibits collective behaviour* [18]. As the charged particles move throughout the plasma, they interact and collide with one another through Coulomb forces, acting even at great distances and giving rise to internal electromagnetic fields. These fields in turn influence particle motion, therefore the term *collective behaviour* can be defined as the phenomena by which mean particle motion is dependant not only on local conditions, but on remote plasmonic regions as well [18].

Supposing that two electrodes are placed inside a plasma as to apply an external electric field, the charged particles would immediately be attracted by the oppositely charged electrode, as highlighted by Figure 1.4. It is evident that the presence of an oppositely charged sheath in proximity to the electrodes obscures the electric field applied throughout the rest of the body, shielding the potential. Neglecting thermal motion the shielding would be perfect and the electric field within the plasma would be zero. In reality however, a minimum particle temperature guarantees the existence of a slight electric field as charged particles are subject to thermal drift.

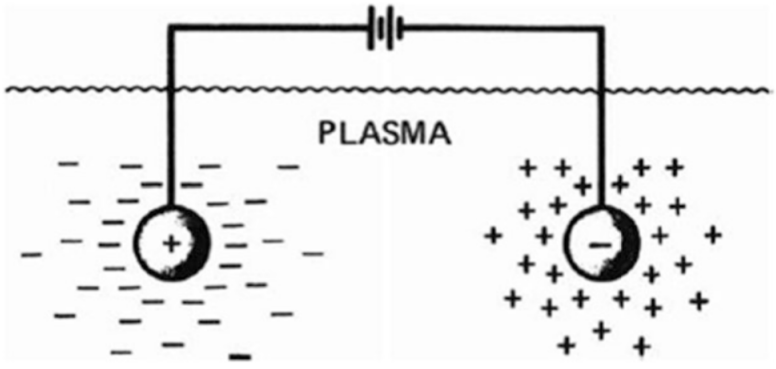

Figure 1.4: Example of Debye shielding [18]

This ability to shield a potential is defined as *Debye shielding* and the related Debye length (λ_D) can be defined as a measure of the thickness of the sheath, given by:

$$\lambda_D = \sqrt{\frac{\epsilon_0 k_B T}{nq^2}} \tag{1.18}$$

Such parameter is inversely proportional to the plasma density (n), as intuitively an increase in the number of charged particles results in more effective shielding, as more particles are present in the sheath. On the other hand λ_D is proportional to the square root of the energy, or temperature, as more energetic particles are more liable to escape the sheath resulting in less efficient shielding.

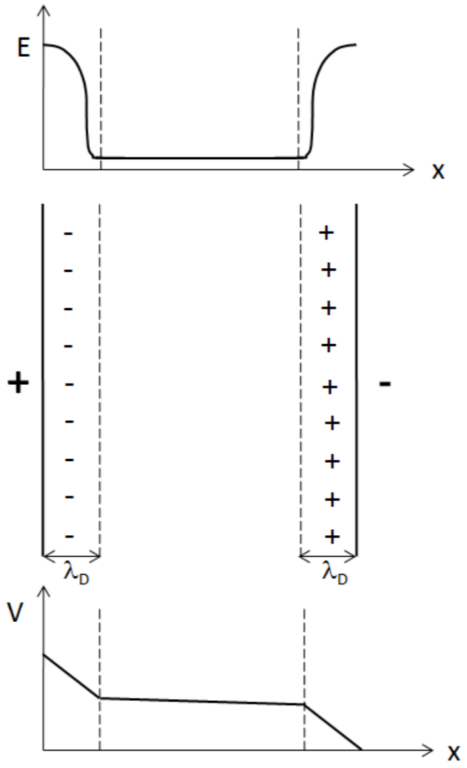

Figure 1.5: Electric field and potential between two electrodes in a plasma

Consequently the term *quasi-neutrality* can be defined, in fact, if the spatial dimension of the plasma is greater than the Debye length ($\lambda_D << L$), it is evident that throughout the volume of the plasma the density of ions created as a result of ionization is roughly equal to that of the electrons [18]:

$$n_e \approx n_i \tag{1.19}$$

1.3.2 Particle collision and ionization

According to quantum mechanics, an electron can occupy only discrete energy levels whilst "orbiting" the nucleus of its atom, the energy spectrum is therefore said to be *quantized*. The electrons tend to occupy the lowest, less energetic, state possible, known as the *ground*

state or level a, yet an absorption of energy by the system would result in the electrons occupying higher energy states, therefore the system is said to be *excited*.

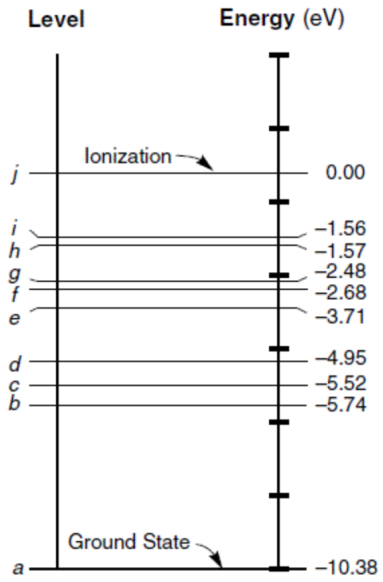

Figure 1.6: Example of energy levels in a Mercury atom

By introducing a high enough level of energy to the system, known as *ionization energy* (ε_i), the electron would be so far from the positive nucleus that it would no longer be bound to the atom by the electrostatic potential, leaving behind a positively charged ion:

$$\mathrm{X} + \varepsilon_{\mathrm{i}} \rightleftharpoons \mathrm{X}^{+} + \mathrm{e}^{-} \tag{1.20}$$

Therefore ionization occurs as a result of the addition of energy at least equal to the ionization energy, there are numerous ways of doing so:

1. Inelastic collision:
   the atoms are ionized as a result of a collision with an energetic particle, typically an electron, which, interacting electrostatically with the electronic shell of the atom, transferring energy to the atom and ionizes it.

   $$X + e^{-} \longrightarrow X^{+} + 2e^{-} \tag{1.21}$$

2. Photoionization:
   the atom is hit by an electromagnetic wave, as a result, photons of frequency ν collide with the atom, transferring energy $h\nu$ to the atom. If the frequency of the wave is great enough this will be sufficient to ionize the atom.

   $$X + h\nu \longrightarrow X^{+} + e^{-} \tag{1.22}$$

   The term h is defined as Planck's constant ($h = 6.6262 \times 10^{-34} Js$) and associates energy to an electromagnetic wave of frequency ν.

3. Field effect:
   if an electric field is applied to the atom, this will polarize it, causing the electrons to be attracted to high potentials and the nucleus to the lower potential. Applying sufficiently strong fields would "rip" the electron from the atom.

The process of ionization is defined by an equilibrium, as the inverse process, known as recombination is also possible. Therefore considering a generic ionization equation:

$$\mathrm{A} \rightleftharpoons \mathrm{A}^+ + \mathrm{e}^- \tag{1.23}$$

An equilibrium constant can be defined:

$$K(T) = \frac{n_+ n_e}{n_A} \tag{1.24}$$

In which n is defined as the volumetric particle density:

$$n = \frac{number\ of\ particles}{volume} \tag{1.25}$$

Equation (1.24) presents three unknowns, the particle densities, whereas the equilibrium constant can be calculated knowing the plasma conditions, as later explained. Two additional equations must be introduced to resolve the system, these derive from considerations on the plasma, such as the equations of conservation of charge and mass, respectively:

$$n_+ = n_e \tag{1.26}$$

$$n_{A_0} = n_A + n_e \tag{1.27}$$

The term n_{A_0} represents the initial number of neutral atoms, whereas n_A is the number of neutral atoms at equilibrium. As aforementioned, the equilibrium constant (K) is known as a result of statistical considerations deriving from the *Maxwell-Boltzmann distribution*. This function defines the probability distribution of energy, or speed, of a generic particle inside a thermodynamic system in equilibrium:

$$P(v) = \left(\frac{m}{2\pi k_B T}\right)^{1/2} \cdot e^{\left[-\frac{mv^2}{2k_B T}\right]} \tag{1.28}$$

As illustrated in Figure 1.7, the Maxwell-Boltzmann distribution is dependant on the energy, or temperature, of the system and defines the most probably distribution of said energy within the thermodynamic system in equilibrium.

The integration of Equation (1.28) results in the average energy per particle in the three degrees of freedom:

$$\varepsilon_{avg} = 3 \cdot \frac{1}{2} k_B T \tag{1.29}$$

The introduction of a partition function (f) allows to define the probability of a generic particle to have a certain energy level associated to each of its degrees of freedom. Similarly, the total partition function for each particle species present in the plasma can be defined

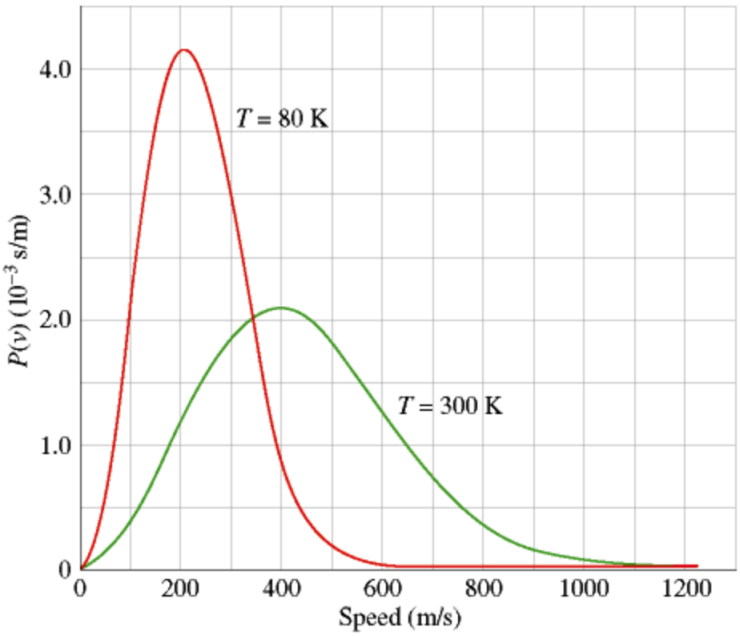

Figure 1.7: Maxwell-Boltzmann distribution for a thermodynamic system in equilibrium

as a product of the single partition functions associated to each degree of freedom (g):

$$F = \prod_g f \tag{1.30}$$

The equilibrium constant can then be expressed as a ratio of such total partition functions:

$$K = \frac{F_+ F_e}{F_A} = 2\frac{(2\pi k_B T m)^{3/2}}{h^3}\frac{\sum_k g_k e^{-\frac{\bar{\varepsilon}_k}{k_B T}}}{\sum_j g_j e^{-\frac{\varepsilon_j T}{k_B T}}} e^{-\frac{\varepsilon_i}{k_B T}} \tag{1.31}$$

Similarly, the *ionization fraction* of a plasma is defined as the number of ions created divided by the initial number of neutrals:

$$\alpha = \frac{n_+}{n_{A_0}} = \frac{n_e}{n_{A_0}} \tag{1.32}$$

After identical statistical considerations, the ionization fraction of a gas in thermal equilibrium can be calculated as a function of the thermodynamic conditions and densities of a plasma through Saha's equation:

$$\frac{\alpha^2}{1-\alpha^2} = 2\frac{(2\pi m)^{3/2}(k_B T)^{5/2}}{p h^3}\frac{f_{iA}}{f_{i+}} e^{-\frac{\varepsilon_i}{k_B T}} \tag{1.33}$$

As better illustrated in Figure (1.8) the ionization fraction tends to an asymptotic value of 1 as temperature is increased, therefore as more energy is introduced to the system, whereas an increase in pressure or density would result in less energy per particle, therefore less ionization.

It is important to realize the extremely high amount of energy required to sustain decent

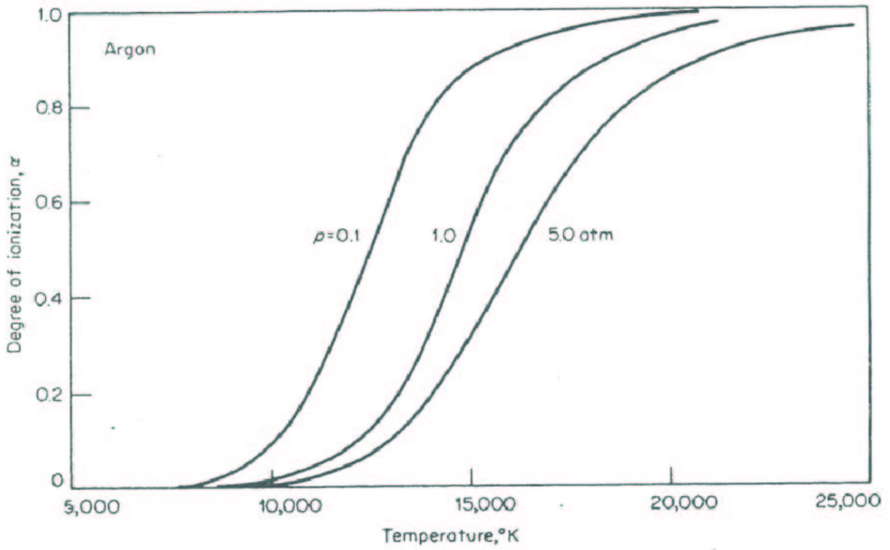

Figure 1.8: Ionization fraction for Argon [17]

levels of ionization when the system is in equilibrium. In electric propulsion the key to achieve the desired level of ionization is to work in non-equilibrium conditions through continuous electron bombardment, thus obtaining a more dense plasma at lower temperatures than that defined by Saha's equation.

Moreover, the temperatures of the species constituting the plasma in Hall thrusters is generally not equal. The lighter and more mobile electrons undergo many collisions as a result of their longer stay in the thruster, they also achieve higher temperatures after being heated up and emitted from the cathode as a result of the thermionic effect. The heavier ions however, are less confined by the magnetic field, their lower residence time in the thruster signifies they undergo less collisions thus achieve lower temperatures. As a result, Hall thrusters are usually characterized as having high electron to ion temperatures ($T_e/T_i \approx 10$).

1.3.3 Plasma modelling

As a result of the enormous number of particles present in plasma, the study of single particle motion would be an unfeasable task. Instead, the plasma behaviour, especially in Hall thrusters, can be modelled as a fluid of neutral particles and electrical charges with Maxwellian distribution functions [19].

Continuity equation

The continuity equation describes the conservation of particles or charge through a generic control volume and can be defined as:

$$\frac{\partial n}{\partial t} + \nabla \cdot (n\overrightarrow{v}) = \dot{n}_s \tag{1.34}$$

In which $\dot{n}_s$ is a source, or sink, of particles in the plasma and the cause of the variations in particle density (n).

Momentum conservation equation

In order to formulate a fluid dynamics equation for the conservation of momentum all forces acting on charged particles within the plasma must be identified. The first is the *Lorentz force*, it acts on all charged particles immersed in electromagnetic fields:

$$\overrightarrow{F}_L = q\left(\overrightarrow{E} + \overrightarrow{v} \times \overrightarrow{B}\right) \tag{1.35}$$

Within the plasma, particles are also subject to pressure gradients as a result of thermal motion. The force exerted by the surrounding fluid, or plasma, on a generic element is defined as:

$$\overrightarrow{F}_p = -\frac{\nabla p}{n} = -\frac{\nabla(nk_BT)}{n} \tag{1.36}$$

Assuming a spatially constant distribution of temperature, the above equation can be simplified to obtain:

$$\overrightarrow{F}_p = -k_BT\frac{\nabla n}{n} \tag{1.37}$$

Finally the particles will collide with other species present in the plasma (namely electrons and ions) thus varying the overall momentum of the single species, such concept will be better explained in the following chapter. The force arising as a result of the interpenetration of these two fluids or species can be defined as:

$$\overrightarrow{F}_{COLL} = -m\overrightarrow{v}_i\nu_c \tag{1.38}$$

In which v_i is the relative velocity between the two particles colliding and ν_c is the collision frequency. These three forces generate a variation in momentum, which can be expressed as:

$$mn\frac{D\overrightarrow{v}}{Dt} = mn\left[\frac{\partial\overrightarrow{v}}{\partial t} + (\overrightarrow{v}\cdot\nabla)\overrightarrow{v}\right] = qn(\overrightarrow{E} + \overrightarrow{v} \times \overrightarrow{B}) - \nabla p - mn\overrightarrow{v}_i\nu_c \tag{1.39}$$

Such equation allows to evaluate how the electrons, acting as a fluid, behave within the plasma. In fact following simplifications to the momentum conservation equation, it is possible to obtain the *Boltzmann relationship for electrons*:

$$n_e = n_{e0}e^{\frac{e\phi}{k_BT_e}} \tag{1.40}$$

The term ϕ represents the potential relative to that in location n_{e0}. Such relation describes the electron response to electrostatic fields, in which their density (n_e) will vary to preserve the pressure of the system [19].

Energy conservation equation

Neglecting viscous heating of the species and considering the transport of heat only by conduction ($\Theta_j = k_j \Delta T_j$) in which k is the thermal conductivity of the species j, it is possible to formulate the energy balance:

$$\frac{\partial}{\partial t}\left(n_j m_j \frac{v_j^2}{2} + \frac{3}{2} p_j\right) + \nabla \cdot \left(n_j m_j \frac{v_j^2}{2} + \frac{5}{2} p_j\right) \overrightarrow{v}_j + \nabla \cdot \Theta_j \tag{1.41}$$

$$= q_j n_j \left(\overrightarrow{E} + \frac{\overrightarrow{R}_j}{q_j n_j}\right) \cdot \overrightarrow{v}_j + Q_j - \Psi_j \tag{1.42}$$

The term $\overrightarrow{R}_j$ represents the mean change in the momentum of particles of species j as a result of collisions with all other particles. Moreover the heat-exchange term Q_j represents the heat generated or lost as a result of elastic collisions, whereas Ψ_j is the energy lost as a result of inelastic collision, typical in ionization processes [19].

Through the equations described so far, it is possible to model the plasma response to changes in its environment. These variations are linked to the *plasma frequency*. This fundamental parameter defines how variations and disturbances propagate within the plasma and is defined as:

$$\omega_p = \sqrt{\frac{n_e q^2}{\varepsilon_0 m}} \tag{1.43}$$

The plasma frequency explains the response of the plasma to variations, such as incident electromagnetic waves. If the frequency of the incident wave is lower than that of the plasma ($\omega < \omega_p$), the electrons are able to respond to the variation and the wave is absorbed by the plasma. This phenomenon is typical in microwave thrusters in which the energy of the wave is absorbed and ionizes the propellant. On the other hand, if the frequency of the incident wave is too high ($\omega > \omega_p$) the particles are no longer able to respond to the variations and the wave travels through the plasma undisturbed as if it were a vacuum.

Hall Thrusters

2.1 Hall effect

2.1.1 Dynamics of charged particles

In order to understand the workings of a Hall thruster, it is fundamental to study the motion of charged particles in electric and magnetic fields. A charged particle within a plasma is subject to numerous forces, resulting from electromagnetic fields applied and collisions between the various species.

The electric and magnetic fields generated in a Hall thruster obey Maxwell's equations formulated for a vacuum:

$$\nabla \cdot \overrightarrow{E} = \frac{\rho}{\varepsilon_0} \tag{2.1}$$

$$\nabla \times \overrightarrow{E} = -\frac{\partial \overrightarrow{B}}{\partial t} \tag{2.2}$$

$$\nabla \cdot \overrightarrow{B} = 0 \tag{2.3}$$

$$\nabla \times \overrightarrow{B} = \mu_0 \left(\overrightarrow{j} + \varepsilon_0 \frac{\partial \overrightarrow{E}}{\partial t} \right) \tag{2.4}$$

In which ρ is the charge density, ε_0 is the electric permittivity in a vacuum, $\overrightarrow{j}$ is the current density and μ_0 is the magnetic permeability in free space. As described earlier, the Lorentz force acts on charged particles as a result of electromagnetic fields and is given by:

$$\overrightarrow{F}_L = q\left(\overrightarrow{E} + \overrightarrow{v} \times \overrightarrow{B}\right) \tag{2.5}$$

Collisions between a particle and other species inside a plasma result in a reduction of the momentum of the charged particle. Evaluating the single collisions for each particle in the plasma would be an unreasonable task, it is possible however, to consider the mean motion of particles and represent the collisions as an overall damping effect on the momentum of the swarm [17].

The frequency with which the momentum of the charge particle drops to zero as a result of collisions is defined as *collision frequency* (ν_c) and depends on the density (n_j), the momentum transfer cross-sectional area of the particle ($Q_{ij}^{(p)}$) and the mean scalar speed

between the particle and the other species with which it collides (v_j):

$$\nu_c = \sum_j n_j Q_{ij}^{(p)} v_j \tag{2.6}$$

Therefore, considering the momentum of a generic charged particle i:

$$P_i = m_i \overrightarrow{v}_i \tag{2.7}$$

This will be damped, as illustrated by the minus sign in Equation (2.8), as a result of collisions:

$$\frac{dP_i}{P_i} = -n_j Q_{ij}^{(p)} v_j dt \tag{2.8}$$

Introducing the collision frequency and rearranging the expression, it is possible to observe the variation of momentum, which as by Newton's laws is a force:

$$\overrightarrow{F}_{COLL} = -\frac{dP_i}{dt} = -m_i \overrightarrow{v}_i \nu_c \tag{2.9}$$

Considering both contributions, it is possible to obtain a differential equation which can be regarded as the equation of motion for a fictitious average particle in the swarm [17]:

$$\dot{\overrightarrow{v}} = \frac{q}{m}\left(\overrightarrow{E} + \overrightarrow{v} \times \overrightarrow{B}\right) - \overrightarrow{v}\nu_c \tag{2.10}$$

It is evident that the above equation resembles the conservation of momentum equation explored in the earlier chapter, in which the pressure gradient has been neglected. The solution to such equation describes the motion of a charged particle in the presence of an electric field, magnetic field and collisions. Solutions to Equation (2.10), for cases inherent to electric propulsion, will be examined in the following sections.

Uniform electric field

Considering Equation (2.10), and simplifying it to account for the presence of an electric field only ($\overrightarrow{B} = 0, \nu_c = 0$), *Coulomb's law* is obtained:

$$\overrightarrow{F}_E = q\overrightarrow{E} \tag{2.11}$$

An electric *potential* (V) can be defined for a conservative electrostatic field:

$$\overrightarrow{E} = -\nabla V \tag{2.12}$$

It is immediate to observe that the force, therefore acceleration, acts parallel to the field lines and the direction of motion is determined by the sign of the electric charge of the particle (q). An ion ($q > 0$) will accelerate concordant to the field lines, from high potentials to lower ones, whereas an electron ($q < 0$) will move in the opposite direction, towards higher potentials.

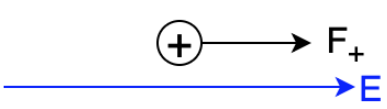

(a) Ion in an electric field

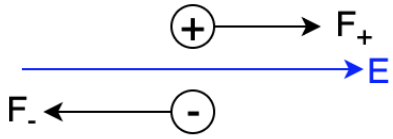

(b) Ion and electron in an electric field

Figure 2.1: Charged particles in an electrostatic field

Uniform magnetic field

From Equation (2.10), considering the case of a charged particle in a magnetic field ($\overrightarrow{E} = 0, \nu_c = 0$), the magnetic force is obtained:

$$\overrightarrow{F}_B = q\left(\overrightarrow{v} \times \overrightarrow{B}\right) \tag{2.13}$$

The force acts perpendicular to the velocity of the particle ($\overrightarrow{v}$) and the magnetic field ($\overrightarrow{B}$). Assuming an area of constant and steady magnetic field and a positively charged particle travelling with a certain velocity ($\overrightarrow{v} = \overrightarrow{v}_{\parallel} + \overrightarrow{v}_{\perp}$), the magnetic force acts in a centripetal direction, causing the particle to travel in a circular orbit, otherwise known as *Larmor motion*, on a plane perpendicular to the magnetic field lines as illustrated in Figure 2.2. It is important to note that, if the velocity has a component parallel to the magnetic field ($\overrightarrow{v}_{\parallel}$), this is unaffected by the magnetic force.

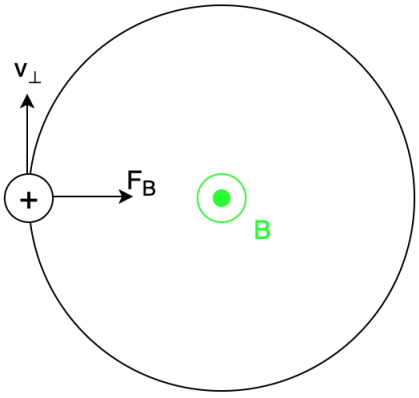

Figure 2.2: Motion of a charged particle in a constant and steady magnetic field

Analysing this cycloidal motion in a reference system rotating with the particle with angular velocity ω, the centripetal magnetic force must be balanced by a centrifugal force [19] such as:

$$q(\overrightarrow{v} \times \overrightarrow{B}) = \frac{mv^2}{r} \tag{2.14}$$

Considering the perpendicular component of the velocity ($v_{\perp}$), from the above equation it is possible to obtain the radius of rotation of the charged particle, known as the Larmor

radius:

$$r_L = \frac{mv_\perp}{qB} \tag{2.15}$$

Similarly, the angular velocity of rotation can be expressed as:

$$v_\perp = \omega r_L \tag{2.16}$$

Substituting into Equation (2.15), it is possible to observe the cyclotron, or Larmor, frequency:

$$\omega_L = \frac{qB}{m} \tag{2.17}$$

In a constant magnetic field, a moving charged particle will rotate around the field lines with a constant angular velocity (ω_c), therefore, unless the particle has a velocity component parallel to the magnetic field lines ($v_\parallel$), there is no net movement. Moreover, the frequency and radius depend on the mass (m) of the particle, this aspect is crucial in Hall thrusters.

2.1.2 E × B fields

Without collisions

Considering the existence of steady electric and magnetic fields, perpendicular to each other and the absence of collisions from Equation (2.10), the motion of the charged particle in such field will be described as a result the Lorentz force:

$$\dot{\overrightarrow{v}} = \frac{q}{m}\left(\overrightarrow{E} + \overrightarrow{v}_\perp \times \overrightarrow{B}\right) \tag{2.18}$$

The solution to this vectorial differential equation can be easily found by considering a reference frame moving with a constant *drift* velocity ($\overrightarrow{v}_d$). It is therefore possible to express the absolute velocity of the particle as a relative velocity to the frame ($\overrightarrow{v}'_\perp$) plus the speed of the reference frame itself ($\overrightarrow{v}_d$) so that:

$$\overrightarrow{v}_\perp = \overrightarrow{v}'_\perp + \overrightarrow{v}_d \tag{2.19}$$

As per hypothesis, having chosen the reference frame to have a constant velocity, differentiating the above expression:

$$\dot{\overrightarrow{v}}_\perp = \quad \dot{\overrightarrow{v}}'_\perp \tag{2.20}$$

Substituting into Equation (2.18), a differential equation whose solution describes the motion of the charged particle in the reference frame moving with constant speed ($\overrightarrow{v}_d$) is obtained:

$$\dot{\overrightarrow{v}}'_\perp = \frac{q}{m}\left(\overrightarrow{E} + \overrightarrow{v}'_\perp \times \overrightarrow{B} + \overrightarrow{v}_d \times \overrightarrow{B}\right) \tag{2.21}$$

If the drift velocity is chosen accordingly, the first and last terms cancel, leaving:

$$\dot{\overrightarrow{v}}'_\perp = \frac{q}{m}\left(\overrightarrow{v}'_\perp \times \overrightarrow{B}\right) \tag{2.22}$$

This differential equation has a known solution, studied in the previous section. It describes the circumferential motion, with larmor frequency, that a particle follows as a result of an external magnetic field. In order to obtain such a solution one must impose the condition that:

$$\overrightarrow{E} + \overrightarrow{v}_d \times \overrightarrow{B} = 0 \tag{2.23}$$

To satisfy the above condition, the drift velocity must be given by:

$$\overrightarrow{v}_d = \frac{\overrightarrow{E} \times \overrightarrow{B}}{B^2} \tag{2.24}$$

With magnitude:

$$|v_d| = \frac{E}{B} \tag{2.25}$$

The complete solution, in a fixed frame, is a helix motion in the $\overrightarrow{E} \times \overrightarrow{B}$ direction, given by the superimposition of a circumferential motion with Larmor frequency (ω_L) and a drift velocity ($\overrightarrow{v}_d$). This curving motion of the particle results in a net movement of charge in the $\overrightarrow{E} \times \overrightarrow{B}$ direction, known as the *Hall effect*. Figure 2.3 shows the cycloidal movement of a positively charged ion.

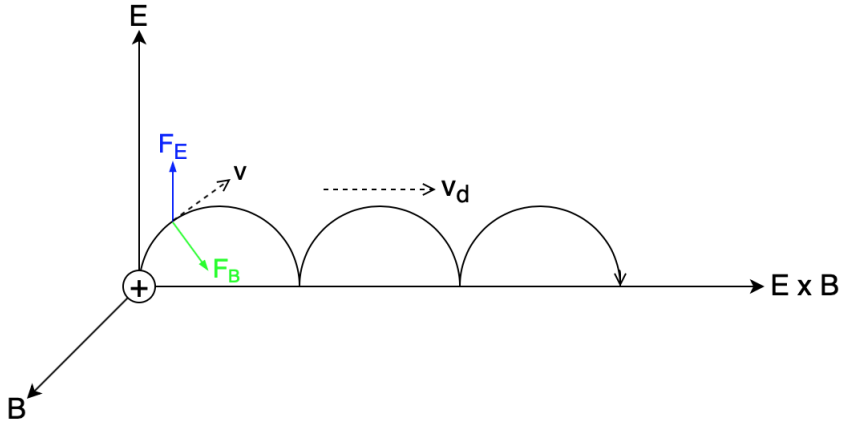

Figure 2.3: Motion of a positively charged particle in an E × B field

If the particle were negatively charged, the net movement would be in the same direction as the positively charged ion. Indeed, as by Equation (2.24), the drift velocity depends solely on the external electric and magnetic fields applied.

With collisions

As previously described, collisions can be incorporated by considering the overall damping effect they have on the momentum of the population of particles. In order to determine the response of the particle to $\overrightarrow{E} \times \overrightarrow{B}$ fields, the *Hall parameter* is introduced:

$$\Omega = \frac{\omega_L}{\nu_c} = \frac{qB}{mnQv} \tag{2.26}$$

This parameter allows to compare the frequency of cycloids with the frequency of collisions, it can therefore be seen as the ratio between $\vec{E} \times \vec{B}$ motion determined by the cycloids and drift along $\vec{E}$ as a result of collisions. Two extreme cases can be observed:

1. $\Omega >> 1$: If the Larmor frequency results much larger than the collision frequency, the charges will follow numerous cycloids before being disrupted by a collision [17], this can be visualized in Figure 2.4.

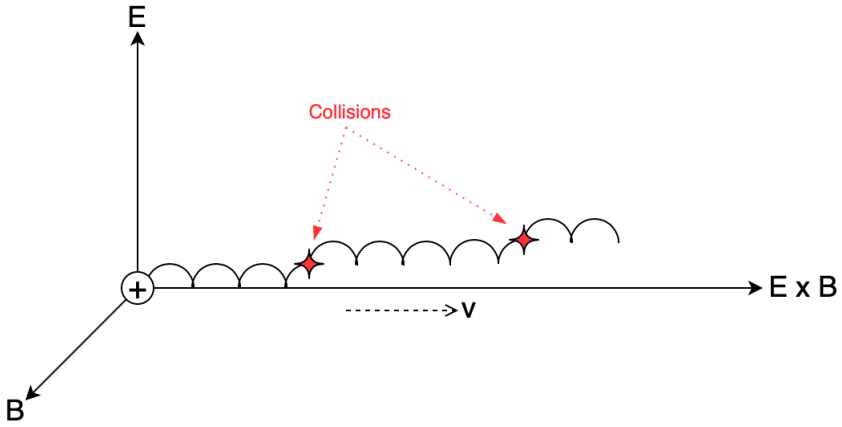

Figure 2.4: Charged particle in E × B field with $\Omega >> 1$

The charged particle follows predominantly the $\vec{E} \times \vec{B}$ direction, as the collisions are negligible, generating a *Hall current*.

2. $\Omega << 1$: The frequency of collisions results much greater than the Larmor frequency, therefore the particle will collide before the completion of the first cycloid. This results in a cross-field motion, with a predominant $\vec{E}$ direction, as highlighted by Figure 2.5.

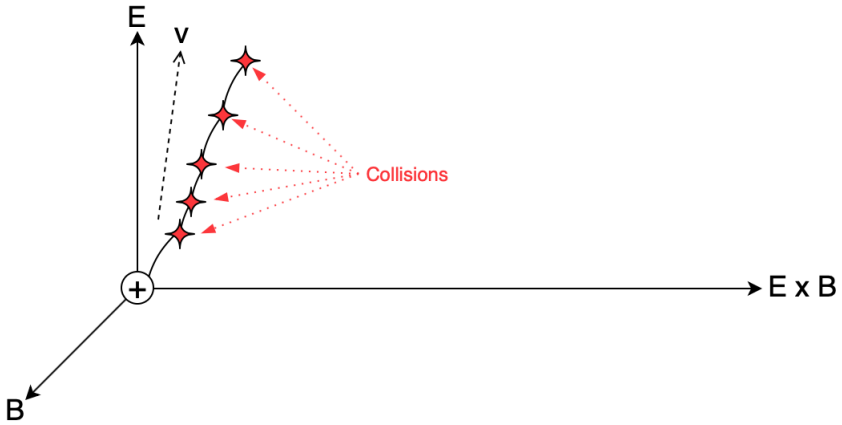

Figure 2.5: Charged particle in E × B field with $\Omega << 1$

The elevated number of collisions results in a net motion of charge in the $\vec{E}$ direction. It is as if the high number of collisions shadow the presence of a magnetic field as the resulting current follows the electric field.

2.2 Geometry and operation

2.2.1 Principles of Hall thruster operation

A Hall thruster consists of an annular channel called discharge chamber, an anode which produces an axial electric field and a magnetic circuit to produce a radial magnetic field [19]. As the name suggests, this thruster exploits the previously mentioned Hall effect by passing the electron current across the radial magnetic field to trap the electrons in an azimuthal drift, or *closed electron drift* [22], around the cylindrical thruster, while the ions are accelerate and ejected by the axial electric field, generating thrust.

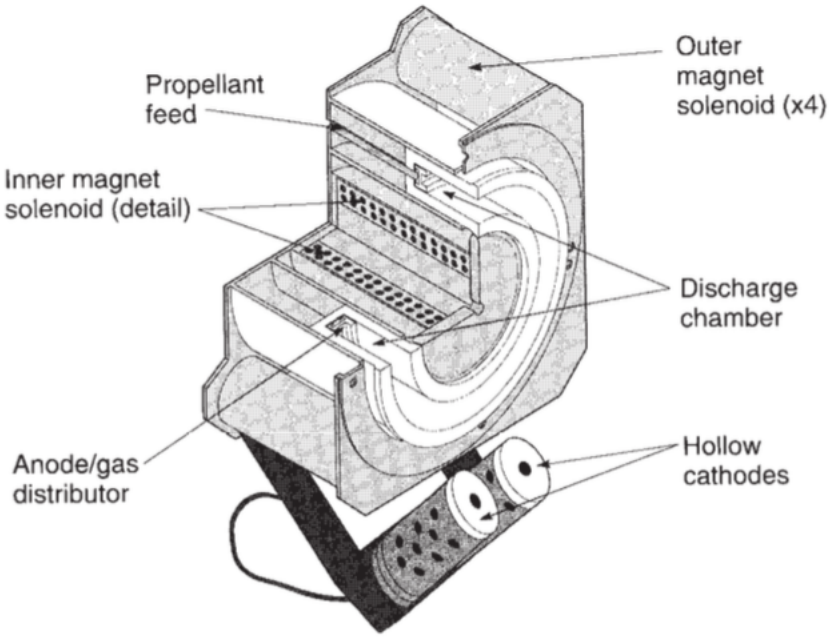

Figure 2.6: Structure of a Hall thruster [3]

A hollow cathode is responsible for the emission of electrons, a small yet crucial part of these enter the thruster in an attempt to follow the axial electric field towards the anode. Upon entering the region with a radial magnetic field, these start moving in an azimuthal $\overrightarrow{E} \times \overrightarrow{B}$ direction, as evident in the simulations illustrated in Figure 2.7, producing a Hall current (j_θ). The electrons are said to be *magnetized*, affected by the magnetic field they are forced to follow many orbits before colliding with a neutral or ion, resulting in cross-field diffusion towards the anode [19] and a very effective ionization of other particles.

In order for the electrons to follow such azimuthal drift in the $\overrightarrow{E} \times \overrightarrow{B}$ direction, the Larmor frequency must be significantly greater than the collision frequency ($\Omega >> 1$), which is guaranteed by maintaining low densities in the vacuum chamber.

The initially neutral propellant, generally xenon, argon or krypton is introduced in the chamber via the feed and is efficiently ionized as a result of collisions with magnetized

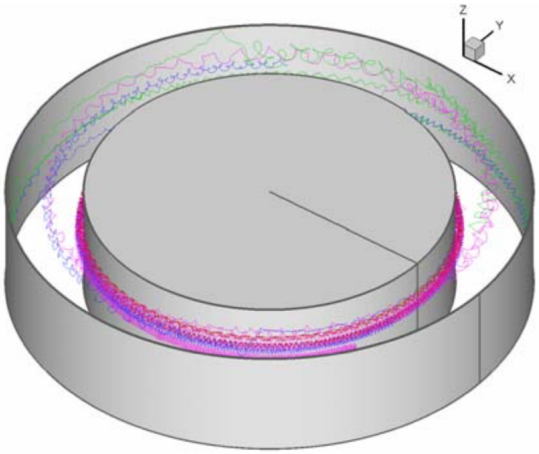

Figure 2.7: Monte Carlo simulation showing electron trajectory inside the chamber [20]

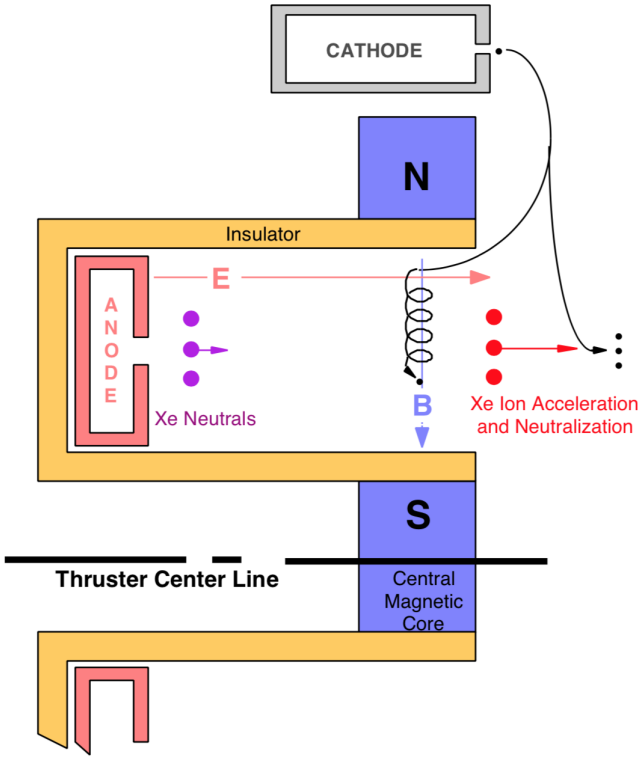

Figure 2.8: Cross section schematic showing fields and particle paths [19]

electrons. The produced ions accelerate in the axial electric field generated by the anode, creating an ion beam (j_x). Upon exiting the thruster, this beam is neutralized by the majority of the electrons emitted by the hollow cathode.

By having an electron current as well as an ionic one, Hall thrusters overcome the limitations of spatial distribution of charge given by Child's law, typical in gridded ion thrusters. This allows for a greater thrust to area ratio, thus making it considerably more compact than the Ion thruster for comparable power and thrust levels.

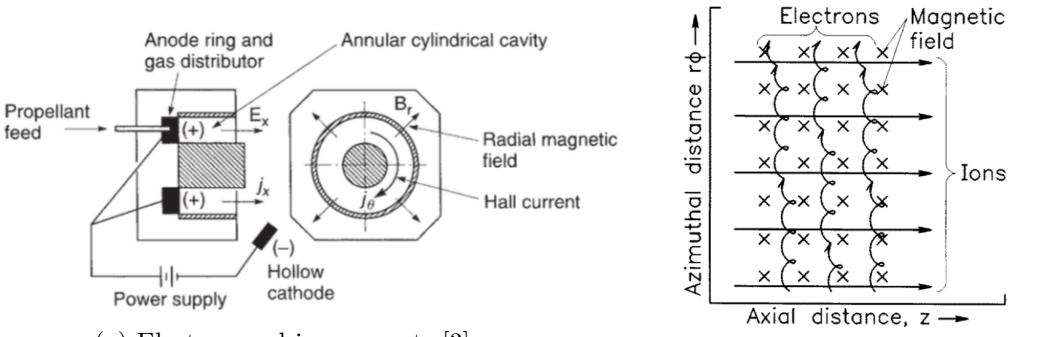

(a) Electron and ion currents [3]

(b) Charged particle motion [21]

Figure 2.9: Particles in Hall thruster annular chamber

It is paramount to observe that the ions do not get trapped in the magnetic field. This occurs because they have a much greater mass than electrons thus, as by Equation 2.15, their Larmor radius will be bigger. In order for the engine to work and eject ions, their Larmor radius must be greater than the characteristic channel diameter, so that these are accelerated by sole electrostatic forces without being affected by the magnetic field. Whereas the electrons, in order to be magnetized, must have a Larmor radius smaller than the characteristic diameter of the thruster, this is guaranteed by their much smaller mass.

Two diverse architectures have stemmed for the concept of Hall effect propulsion, the root of which is the material used in the channel walls. The *Stationary Plasma Thruster* (SPT), which has been the primary focus for this research, presents longer channel walls made of insulator material, typically boron nitride. On the other hand, the *Thruster with Anode Layer* (TAL) has shorter walls as a result of the conducting metals used, such as stainless steel.

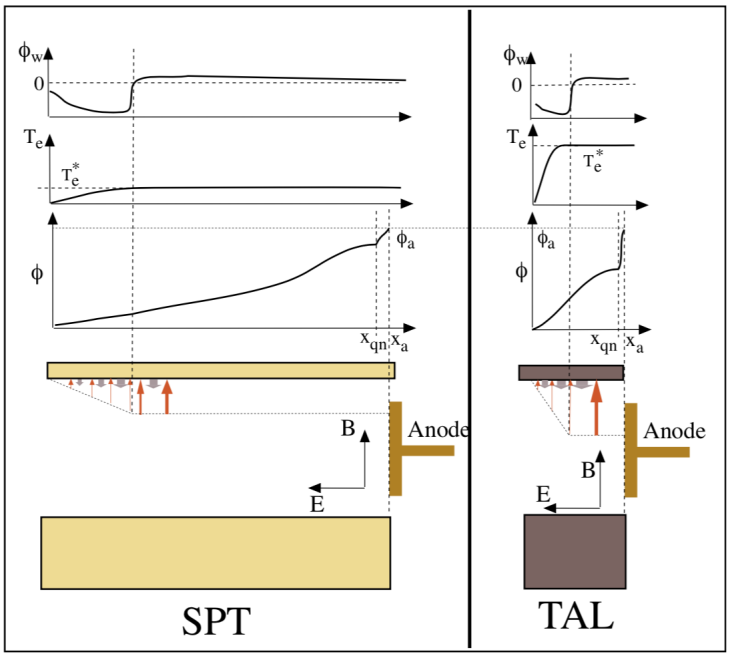

Figure 2.10: Difference between SPT and TAL architecture [23]

The reason for the difference in length of the walls can be visualized in Figure 2.10. Due to the small spatial extent of the acceleration region of the TAL, in the order of an electron cyclotron radius, resulting from the emission of *secondary* electrons from the metallic walls thus rapid increase in electron temperature and a sharp potential drop. Consequently, the discharge does not need to be contained in a long channel and the walls result shorter [23].

2.2.2 Field profiles and currents in Hall thrusters

The radial magnetic field is maximum in proximity to the exit plane, providing a higher localized electron temperature and thus ionization rate, it is therefore possible to identify an *ionization region* located upstream of the maximum magnetic field. Correspondingly, the axial electric field, generated between the anode at the base of the annular channel and the external hollow cathode plasma, will also be maximum in said region, determining the *acceleration region* [19], as clearly shown in Figure 2.11.

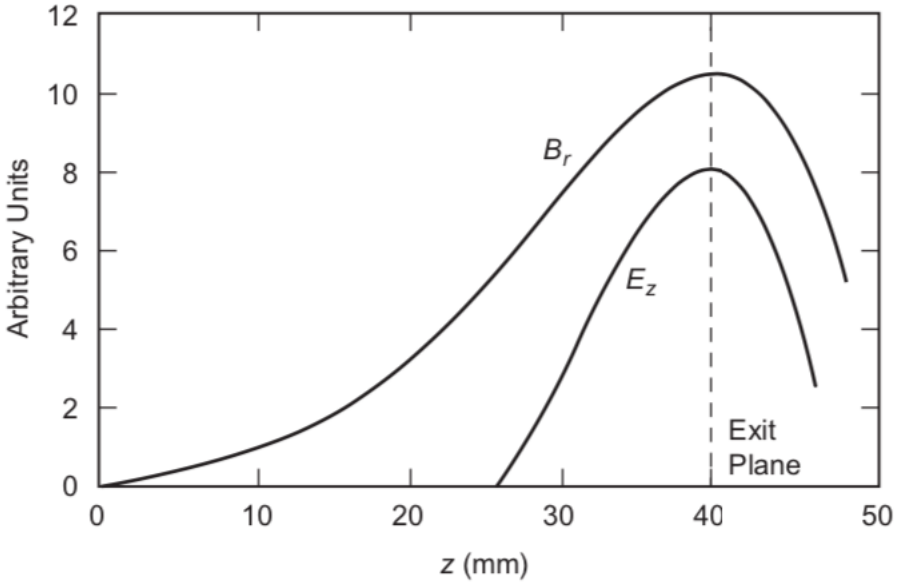

Figure 2.11: Typical magnetic and electric field intensities [19]

The magnetic field is designed to be maximum at the exit, falling to zero at the anode. Other than allowing for the azimuthal drift of electrons, this gradient permits an *ion lens* effect as ions are deflected away from the walls, avoiding erosion and wall losses, and are focused into the beam [19]. An example of the typical shape of magnetic field lines can be found in Figure 2.12, these in fact are not perfectly radial, but are shaped to allow for the afore mentioned deflection.

The ionization region does not coincide with the anode potential, ions are generally produced throughout the channel at varying potentials, resulting in a disparity in ion velocities and a divergence of the beam [19]. A typical potential drop is evident in Figure 2.13.

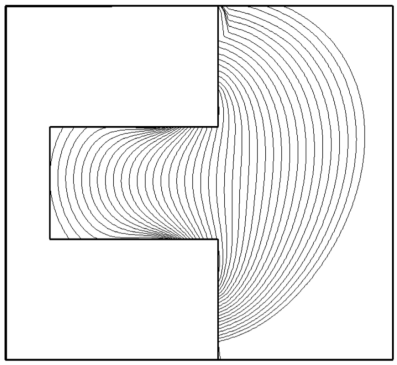

(a) Magnetic field lines [24]

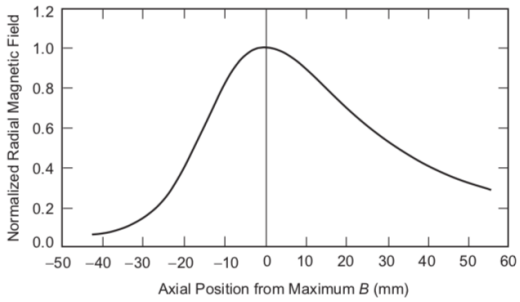

(b) Magnetic field intensity [25]

Figure 2.12: Magnetic field in NASA-173Mv Hall thruster

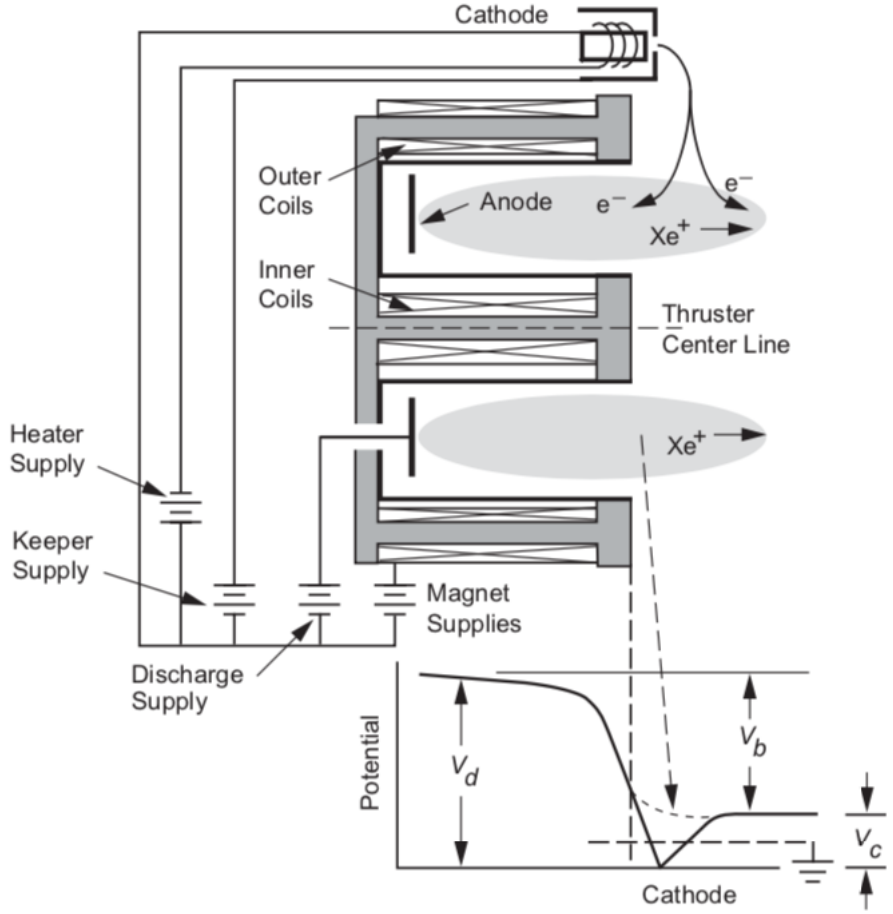

Figure 2.13: Electrical schematic and potential distribution [19]

The cathode is placed at a lower potential with the keeper biased positive to ease the extraction of electrons, the beam voltage can be expressed as the difference between the discharge potential and the cathode potential:

$$V_b = V_d - V_c \tag{2.27}$$

As mentioned earlier, ions are created throughout the chamber at varying potentials, their

velocities therefore, vary strongly. An average velocity can be calculated, considering the average potential over which ions are accelerated ($\overline{V}_b$):

$$\overline{v}_i = \sqrt{2\frac{q}{m_i}\overline{V}_b} \tag{2.28}$$

The current measured between the anode, discharge supply and cathode is due to the electron and ion flow within the circuit. To better define the curent it is possible to express the *current density* as:

$$j = nqv \tag{2.29}$$

In which n is the particle density, q is the charge and v is the speed of the particles. The current at the anode is determined by the electrons emitted at the cathode and entering the thruster (I_{ec}) moving slowly towards the anode by cross-field diffusion resulting from collisions, plus the electrons created as a result of ionization (I_{ei}). It is easy to see how the latter are equal in number to the ions created ($I_{ei} = I_{ib}$) therefore the anode electron current can be expressed as:

$$I_{ea} \approx I_{ec} + I_{ib} \tag{2.30}$$

The velocity of ions at the anode and cathode is much smaller than that of electrons and having hypothesized a quasi neutral plasma $n_e \approx n_i$, it is possible to neglect the ion current contribution [19]. The discharge current therefore can be expressed as the sole electron current collected at the anode or emitted by the cathode:

$$I_d \approx I_e \approx I_{ea} \approx I_{ec} + I_{ib} \tag{2.31}$$

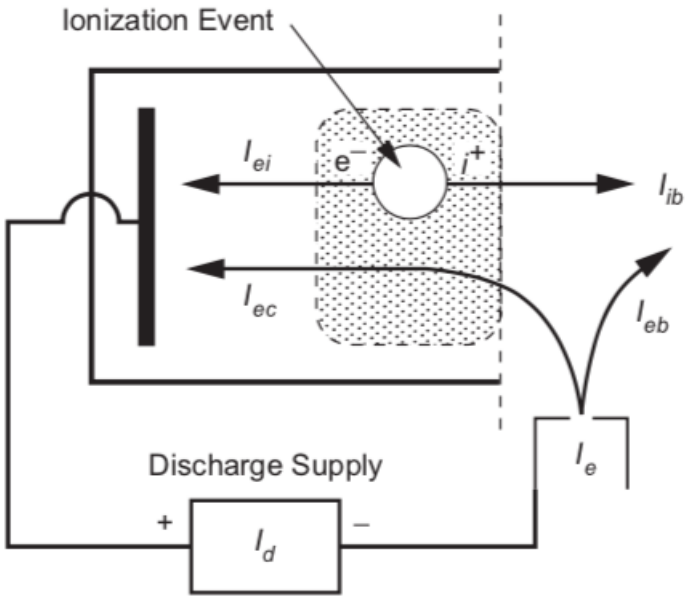

Figure 2.14: Schematic of currents in Hall thruster [19]

Similarly, having neglected the ion current at the cathode, the discharge current can be

considered the electron current emitted by the cathode, given by the electrons entering the thruster plus the ones that neutralize the ion beam:

$$I_d \approx I_e \approx I_{ec} + I_{eb} \tag{2.32}$$

It is clear that in order to neutralize the beam, the electron current must be equal to the ejected ion current $I_{eb} = I_{ib}$.

2.2.3 Hollow cathodes

The ionization of propellant by *electron bombardment* inside a Hall thruster and subsequent neutralization of the ion beam relies on the emission of electrons by a cathode. Differently from a basic cathode in which electron emission is carried out exploiting the thermionic effect, a hollow cathode generates a plasma in which an electron current is dominant over the ionic one. A schematic of such technology is visible in Figure 2.15.

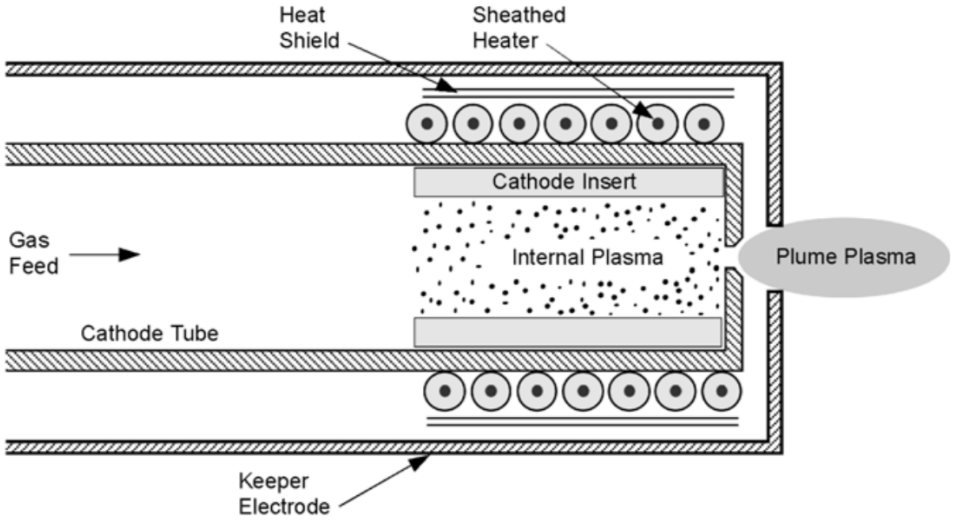

Figure 2.15: Schematic of hollow cathode [19]

A hollow cathode consists of a heater, an insert and a keeper. The insert, placed inside the cathode tube, is made of a material with a low work function as to facilitate the emission of electrons. The heater consists of a coil of wire, passing an electron current in these raises the temperature of the insert to emit electrons via the thermionic effect. These electrons ionize the propellant injected in the cathode tube through the gas feed, generating a cold and high-density internal plasma [19].

The keeper is electrically isolated from the cathode tube, a potential (around 30V) is applied between the two, with the keeper biased positive, to allow for the prevalent emission of electrons and reduce ion bombardment. In order to effectively neutralize the ion beam, the potential must be lower than the beam itself. The ion current from the hollow cathode is negligible as the heavy ions gain less velocity in such low potential.

Three plasmonic regions can be identified from Figure 2.16: a dense plasma in the insert region, a high current density plasma in the orifice, and a diffuse plume plasma outside of the cathode. The plasma ions generated throughout the device neutralize the electron space charge; as a result, hollow cathodes produce high currents at low voltages as compared with vacuum cathode devices [19].

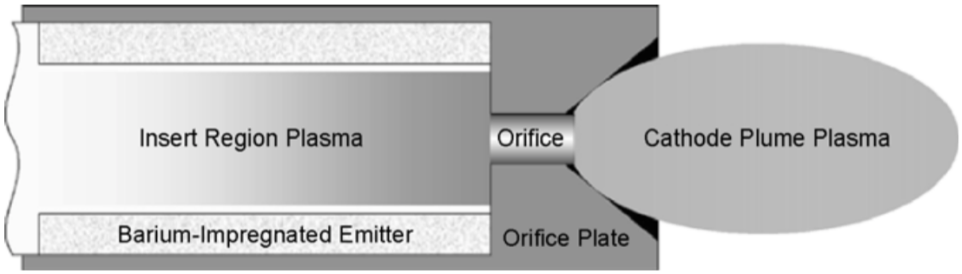

Figure 2.16: Plasma regions in a hollow cathode [19]

A hallow cathode is said to work in a *self heating* mode, in which the discharge is maintained even after the heater is switched off, as long as the ionization has begun. The emission of electrons from the insert is sustained by plasma bombardment.

2.3 Performance modelling

2.3.1 Thrust equations

In a Hall thruster the transfer of momentum from the plasma to the engine to generate thrust is obtained as a result of the magnetized electrons that are constrained not to move axially by the transverse magnetic field. The Hall force per unit area on the electrons is balanced by the magnetic force and exerted on the magnets by the electrons to generate thrust [19]:

$$\overrightarrow{T} = n_e \cdot q_e \overrightarrow{v}_\theta \times \overrightarrow{B} \tag{2.33}$$

In which v_θ is the drift velocity of the electrons and by introducing the current density it is possible to obtain:

$$\overrightarrow{T} = \overrightarrow{j}_\theta \times \overrightarrow{B} \tag{2.34}$$

It is intriguing to consider how thrust is obtained as a result of electromagnetic forces, whereas the propellant is ejected by electrostatic forces. For this, Hall thrusters are often refered to as hybrids between electrostatic and electromagnetic thrusters.

Similarly, as by Equation (1.3), thrust is defined as the mass flow rate of propellant ejected, so the mass flow rate of ions, times the speed at which these ions are ejected:

$$T = \dot{m}_i v_i = \dot{m}_p c \tag{2.35}$$

In which the mass flow rate to the cathode has been neglected ($\dot{m}_p \approx \dot{m}_a$). The mass flow rate of ions created can be linked to the total mass flow rate of propellant to the anode through the *mass utilization efficiency* ($\dot{m}_i = \eta_u \dot{m}_p$) which shall be better explained in the following section. The kinetic power of thrust can be expressed recalling Equation (1.9):

$$P_T = \frac{Tc}{2} = \frac{\dot{m}_p c^2}{2} \tag{2.36}$$

Therefore substituting the above definition of thrust and introducing the mass utilization efficiency, the kinetic power of thrust can be further defined as:

$$P_T = \frac{\eta_u^2 \dot{m}_i^2 v_i^2}{2\eta_u v_i} = \eta_u \frac{T}{2m_i} \tag{2.37}$$

The mass flow rate of ions can be expressed in relation to the ionic current density:

$$I_b = j_b A = n_i q v_i A = q\frac{\dot{m}_i}{m_i} \tag{2.38}$$

Where m_i is the ion mass. Recalling Equation (2.28), in which the average velocity is expressed as a function of the accelerating potential, it is possible to observe the proportionality of thrust to the beam current (I_b) and the effective acceleration voltage ($\overline{V}_b$) [19]:

$$T = \sqrt{\frac{2m_i}{q}} I_b \sqrt{\overline{V}_b} \tag{2.39}$$

In order to obtain Equation (2.39) hypotheses such as a unidirectional and singly ionized beam have been made. However, the beam in a Hall thruster is not unidirectional and diverges to develop a plume as a result of ion repulsion. The geometries of these plumes are very complicated and heavily depend on the species present in the beam, examples are illustrated in Figure 2.17.

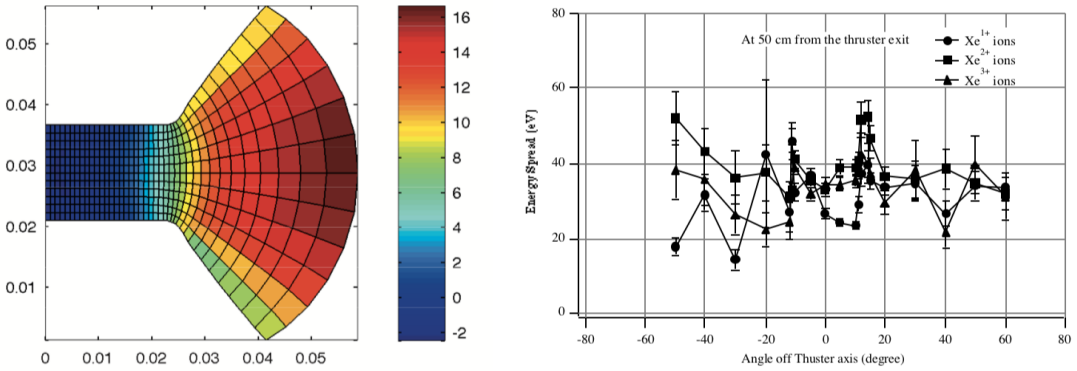

(a) Axial ion velocity (km/s) from centerline [26] (b) Ion energies at 50cm from thruster exit [27]

Figure 2.17: Examples of plume divergence characterization from literature

The divergence of such a beam results in a reduction of thrust, as the current is no longer entirely aligned in the axial direction, parallel to the thrust. These effects are modelled

by the introduction of a correction factor [19]:

$$F_t = \frac{\int_0^r 2\pi r j(r) \cos\theta(r) dr}{I_b} \tag{2.40}$$

In which $j(r)$ represents the current density as a function of the radius and is usually determined by direct measurement with instruments such as Wein Filters and θ is the half-angle divergence of the beam.

Moreover, corrections for multiple charge ions must be made, this phenomena is typical in Hall thrusters as a result of their very efficient ionization. In the presence of multiple species, the beam current is given by:

$$I_b = I^+ + I^{++} \tag{2.41}$$

The thrust for multiple species is given by the sum of the thrust for each species [19]:

$$T_m = I^+ \sqrt{\frac{2mV_b}{q}} + I^{++} \sqrt{\frac{mV_b}{q}} = I^+ \sqrt{\frac{2mV_b}{q}} \left(1 + \frac{1}{\sqrt{2}} \frac{I^{++}}{I^+}\right) \tag{2.42}$$

A correction factor (α) can be defined as:

$$\alpha = \frac{I^+ + \frac{1}{\sqrt{2}} I^{++}}{I^+ + I^{++}} = \frac{1 + 0.707 \frac{I^{++}}{I^+}}{1 + \frac{I^{++}}{I^+}} \tag{2.43}$$

Phenomena such as beam divergence and multiple charge ions result in a reduction of thrust, the global effect can be considered by the introduction of the parameter γ:

$$\gamma = \alpha F_t \tag{2.44}$$

The total thrust can therefore be calculated as:

$$T = \gamma I_b \sqrt{\frac{2m}{q} \overline{V}_b} \tag{2.45}$$

2.3.2 Corrections for atmospheric flight

Equation 2.45 has been used to determine the thrust produced by an electrostatic thruster operating in space. However, corrections must be introduced as a result of the residual atmosphere at VLEO altitudes. In fact, operating in an air-breathing mode, Equation 2.45 should be modified to account for the momentum of the air flow on the inlet [1]:

$$T = \gamma I_b \cdot \sqrt{\frac{2m}{q} \overline{V}_b} - \eta_c \dot{m} u_\infty \tag{2.46}$$

As previously mentioned, m represents the weight of propellant, in this case ions of the various species constituting air. The particles' rate of change of momentum ($\dot{m}u_\infty$) is

multiplied by η_c defined as the *intake efficiency*:

$$\eta_c = \frac{\dot{m}_{actual}}{\dot{m}_{ideal}} \tag{2.47}$$

In which the ideal mass flow rate is given by:

$$\dot{m}_{ideal} = m \cdot n_\infty u_\infty A_i \tag{2.48}$$

The far field flow characteristics are described by n_∞ and u_∞, in which the density can be obtained as a result of atmospheric models whereas the air speed relative to the intake depends on orbit altitude. Finally A_i represents the total intake area.

The dynamics of the intake are a crucial aspect in air-breathing electric propulsion. The intake must both collect and compress air in order for the thruster to work efficiently, yet minimizing the drag produced as a result. These concepts, as well as the efforts in reproducing the atmospheric condition at VLEO altitudes, are vastly explored by Andreussi et al [1] and Walsh et al[29], the present work however, shall concentrate on the design and performance evaluation of a thruster optimized for working iwith molecular propellants, temporarily setting aside the effects of the intake.

2.3.3 Efficiencies definition

The ions accelerating and exiting the thruster provide the desired thrust, in fact, it is fundamental to distinguish between the mass flow rate of neutral propellant injected in the thruster and these ions that effectively accelerate and exit, for this reason the *mass utilization efficiency* is introduced.

In typical xenon-operating Hall thrusters, almost all the propellant injected in the anode is ionized, however, in air-breathing Hall thrusters, this is not yet the case, as shall be extensively investigated throughout this research. Moreover, not all the propellant ($\dot{m}_p$) is fed directly to the anode, some is directed to the hollow cathode ($\dot{m}_c$) to sustain electron emission. It is therefore possible to define the *mass utilization efficiency* of the thruster as:

$$\eta_u = \frac{\dot{m}_i}{\dot{m}_p} = \frac{\dot{m}_i}{\dot{m}_a + \dot{m}_c} \tag{2.49}$$

Recalling Equation 2.35, it is possible to define the effective exhaust velocity as:

$$c = \frac{T}{\dot{m}_p} = \frac{\dot{m}_i vi}{\dot{m}_p} = \eta_u v_i \tag{2.50}$$

The above relation compares the effective exhaust velocity to the effective speed of the accelerating ions. In fact, these two parameters are not the same as not all neutral are ionized, therefore not all the propellant mass flow rate injected in the thruster exits at speeds v_i. The effective exhaust velocity in fact considers that only a part of the total mass flow rate injected in the anode will exit the thruster at speed v_i.

The total efficiency is defined as the kinetic power of the accelerated ions, or *jet power* divided by the total power:

$$\eta_T = \frac{P_T}{P_{tot}} \tag{2.51}$$

The total power is the sum of the power supplies feeding the anode, cathode heater, keeper and magnetic circuit:

$$P_{tot} = P_a + P_h + P_k + P_m \tag{2.52}$$

Space qualified cathodes are capable of working in *self heating* mode, that is to say that once the cathode has been heated up sufficiently, the heater can be switched off and the plasma discharge will be maintained as a result of the sole heating given by electron collisions with the insert. The heater power (P_h) term can therefore be neglected when computing efficiencies, however, for the sake of clarity, such term has been considered in this study. Substituting the kinetic power from Equation (1.9):

$$\eta_T = \frac{\frac{1}{2}\dot{m}_p c^2}{P_{tot}} \tag{2.53}$$

From which:

$$\eta_T = \frac{T^2}{2\dot{m}_p P_{tot}} \tag{2.54}$$

The anode efficiency can be defined as the discharge power divided by the total power input:

$$\eta_a = \frac{P_d}{P_{tot}} \tag{2.55}$$

In which the discharge power is given by the current (I_d) times the discharge voltage (V_d) provided by the power supply:

$$\eta_a = \frac{I_d V_d}{P_{tot}} \tag{2.56}$$

The energy lost in the ionization of propellant, earlier defined as the ion production cost (ε_b) is defined as the discharge power divided by the ion current produced:

$$\varepsilon_b = \frac{P_d}{I_b} \tag{2.57}$$

The resulting parameter has units eV/ion and represents the energy expenditure to ionize a single atom. Similarly the fraction of discharge current that produce the beam can be defined as:

$$\eta_b = \frac{I_b}{I_d} \tag{2.58}$$

It follows that the fraction of discharge voltage that produces the beam:

$$\eta_v = \frac{V_b}{V_d} \tag{2.59}$$

The above parameter relates the accelerating voltage (V_b), responsible for the acceleration of ions therefore for the generation of thrust, to the discharge voltage (V_d) applied by the power supply. As mentioned earlier these two differ as a result of ionization events not

happening at the anode, where the potential is exactly V_d, but further along the chamber at lower potentials. Moreover, the ions do not accelerate to zero (or ground) potential, as illustrated in Figure 2.13, but two a slightly higher value as a result of the cathode keeper being biased positive to extract the electrons.

Substituting (2.59), (2.58), (2.56) and (2.49) through (2.45) and in (2.54), the global efficiency can be defined as:

$$\eta_G = \gamma^2 \eta_b \eta_v \eta_u \eta_a \tag{2.60}$$

The above relation illustrates that maximizing beam current production and beam energy and minimizing propellant flow at the cathode derives in maximum efficiency. It also considers beam divergence and multiple charged ions in the γ term and is essential in illustrating how conversion of power supply inputs into the beam current and beam voltage influence the efficiency thus effectively optimizing the Hall thruster performance [19].

Figure 2.18 demonstrates the principal characteristics of a Hall thruster. It is immediate to observe how there is a threshold voltage, under which there is no ionization, therefore no current. Moreover it is clear that the electric and utilization efficiency (respectively proportional to I_i/I_d and I_i/I_m in 2.18a) increase with the discharge voltage.

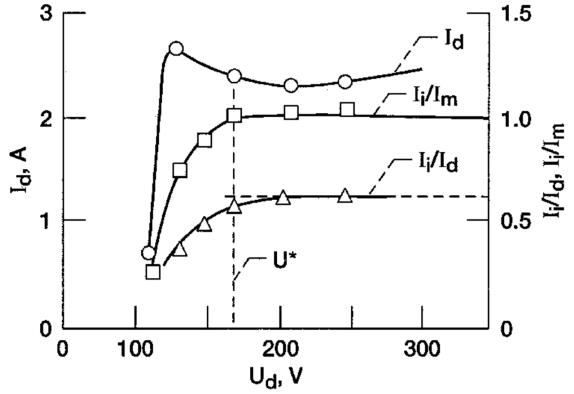

(a) Voltage curent characteristic and efficiencies of SPT Hall thruster

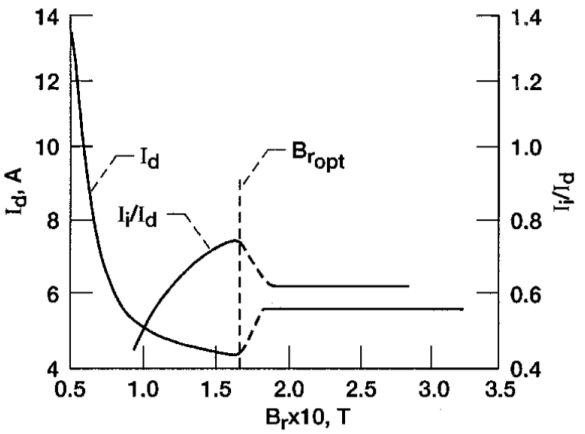

(b) Magnetic field influence

Figure 2.18: SPT operation with discharge voltage and magnetic field influence on SPT operation [28]

The magnetic field has a fundamental task in the efficient operation of a Hall thrust. If the field intensity is too low, the electrons will not be confined in a Hall current and will follow the electric field to the anode. Increasing the intensity results in reduced electron mobility towards the anode, therefore lower currents and more ionization of propellant, therefore more efficient operations. If however, the magnetic field results too strong, the electrons will not be capable of entering the channel and the efficiency will drop.

Similarly, as illustrated in Figure 2.19, the total efficiency increases as a function of the discharge voltage. At a fixed voltage, efficiency improved with higher flow rate because the

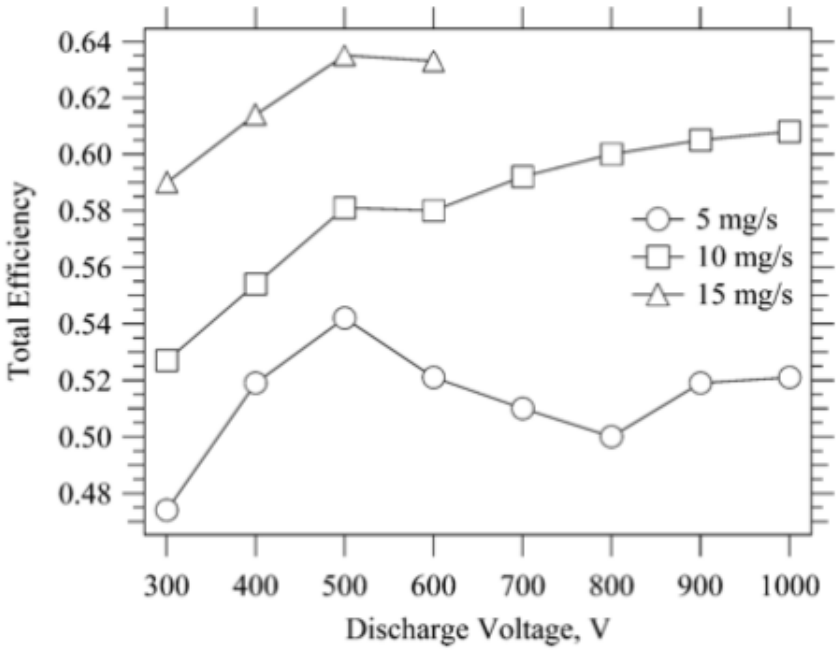

Figure 2.19: Total efficiency as a function of discharge voltage [24]

ionization rate is known to be proportional to the neutral density, these trends emphasize the importance of current density in achieving optimal performance [24].

Molecular Propellants for Electric Propulsion

3.1 Ionization of molecular propellants

3.1.1 Properties of conventional propellants

For its numerous advantageous properties, xenon (Xe) has represented the ideal candidate for typical electrostatic thrusters. As briefly explained in previous chapters, the principal characteristics of this propellant is its high atomic mass and low first ionization energy which lead to lower ionization costs and higher thrust. Storability represents another factor in which xenon is preferred for its high densities at cryogenic temperatures and low tank mass to propellant mass ratio for supercritical storage [30].

Element	First ionization energy (eV)	Atomic mass (amu)	Abundance in air
Xe	12.13	131.29	0.087ppm
Kr	13.99	83.80	1ppm
Ar	15.76	39.95	9340ppm
Ne	21.56	20.18	18ppm
N_2	15.58	28.01	78%

Table 3.1: Properties of typical propellants

Xenon, like other noble gasses, is extracted from the atmosphere, in which it is present at a concentration of 0.087 ppm (parts per million) in volumetric composition. Such rarity leads to a total global xenon production of only 10 ton per year [31]. This scarcity results in the inevitable consequence of high xenon prices, especially when compared to the less efficient, yet cheaper, noble gas alternatives like krypton, argon or neon.

Uncertainty in xenon usage over the past years has led to price unpredictability, as the balance between supply and demand, essential to maintain constant prices in the market has not yet been reached [32]. For this reason, the price of xenon fluctuates over years, as the scarse stocks struggle to meet the unpredictable demands.

However, the advent and rapid growth of the small satellite industry has led to a substantial increase in the number of missions thanks to more accessible costs. These small

satellites are growingly dependant on light and efficient propulsive system for which electric propulsion represents the ideal solution, as a results xenon demand is expected to rise abruptly [33].

Another crucial aspect that has made xenon the primary choice for electric thruster propellant is that it is both inert gas and non-toxic, meaning it does not chemically react with the spacecraft to form undesired coating to panels and equipment. This is a fundamental characteristic that allows to avoid spacecraft erosion or undesired interaction with the payload or equipment, whereas the non toxicity means it is safe to handle and use during ground testing.

In fact it is important to note that, even if a cheaper alternative propellant that matches or exceeds the performance of a xenon is discovered, this aspect of interaction with the spacecraft may prevent the propellant from becoming a viable option. Some examples are Mercury (Hg), which was used as a working gas in first Hall Thruster experiments, or Iodine (I), which is stored in solid phase but its vapours in the plume are toxic and react with organic compounds [34].

3.1.2 Challenges in ionizing molecular propellants

Molecular propellants represent a promising alternative to xenon, the abundance of such propellant in the atmosphere is evident as is the positive impact in cost reduction. The exploitation of such *in situ* propellant would also allow for continuous drag compensation at VLEO altitudes with innovative air breathing thruster designs. However, as shall be extensively explained in this chapter, the different properties of molecular propellants result in a degradation of performance when compared to xenon benchmarks, and shall require an optimization of the design of typical SPT-type Hall thrusters.

The principal differences between nitrogen, or air, and xenon as propellants for electrostatic thrusters reside in the lighter weight and higher first ionization energy of the former. As reported in Table 3.1, N_2 weighs about a quarter of the atomic weight of xenon. A first consequence of such lighter mass is a lower impulse of the impacting particle on the channel wall, this reduces the erosion, potentially extending the operational lifetime of the thruster.

The second consequence is that lower masses result in higher speeds achieved by the species, thus lower transient time of the particles in the thruster's chamber. This reduced residence time, coupled with the higher first ionization energy, makes the ionization of nitrogen much more difficult than xenon [35]. Further energy losses can be associated to the molecular structure of nitrogen that inevitably leads to vibrational and rotational excitation [36].

The lower rates and higher costs of ionization lead to much lower efficiencies and thrust levels, and an increase difficulty in sustaining a plasma discharge, which must be countered by higher mass flow rates, ultimately resulting in lower specific impulses.

The presence of oxygen causes undesired oxidation reactions within the BaO impregnated tungsten in cathodes, rapidly degrading their performance. For such reason, in order to implement these new technologies it is fundamental to utilize non reactive materials in cathodes such as Lanthanum Hexaboride (LaB6) cathodes.

Thanks to the extensive works of Cha [35] and Hwang et al [37], the ionization rate for nitrogen can be modelled and compared to that of xenon, as a function of electron temperature. It is immediate to observe from Figure 3.1 the much lower ionization rate of nitrogen, occurring as a result of the aforementioned problems of higher first ionization energy and reduced transient times.

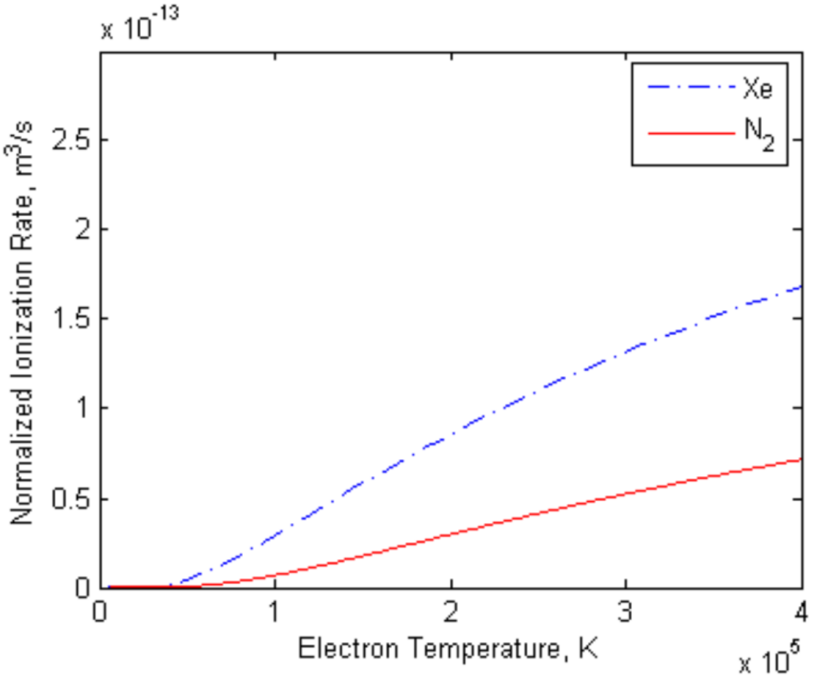

Figure 3.1: Ionization rate of N_2 compared to Xe [35]

The principal source of ions when using nitrogen as propellants derives from:

$$N_2 + e^- \rightarrow N_2^+ + 2e^- \tag{3.1}$$

As reported in the works of Saporoschenko [38] and Gurciullo et al [36], it is plausible to assume that N_2^+ is the dominant ion species in air breathing Hall thrusters. This is due to the fact that the dissociation of the molecule followed by ionization of the new atomic species is not only more energetically expensive, as illustrated in Table 3.2, but also less probable than the direct molecular ionization. The lack in probability results as a fact that the lighter and faster nitrogen atoms have a short transit time in the Hall thruster chamber [35], thus the time would not be sufficient for the two reactions to occur.

Description	Threshold Energy (eV)	Reaction
Excitation	6.17	$N_2 + e^- \rightarrow N_2^* + e^-$
Dissociation	9.80	$N_2 + e^- \rightarrow N + N + e^-$
Atomic ionization	14.55	$N + e^- \rightarrow N^+ + 2e^-$
Molecular ionization	15.58	$N_2 + e^- \rightarrow N_2^+ + 2e^-$
Dissociative ionization	24.32	$N_2 + e^- \rightarrow N^+ + N + 2e^-$

Table 3.2: Reactions in N_2 low temperature plasma [35]

Therefore, in order to efficiently utilize molecular propellants such as nitrogen for electric propulsion, it is fundamental to enhance the ionization within the thruster. In the following chapters, changes in design of the thruster and operational conditions shall be explored to guarantee an efficient nitrogen plasma discharge.

3.1.3 Atmosphere composition and orbit analysis

When studying the feasibility of air-breathing propulsion, a model of the density and composition of the atmosphere at various altitudes must be studied in order to estimate crucial parameters like available mass flow rate and drag.

Atmospheric conditions such as total or partial densities and temperatures change significantly with altitude, as a result, the composition is not constantly defined but characterized by varying ratios of the constituting species. Modern models, attempt to predict these ratios as a function of altitude, considering other aspects such as seasons and solar activity. These standards are summarized in ECSS-E-ST-10-04C [39] issued in 2008.

Modern modelling techniques simulate the atmosphere principally using two different baselines, which generate two fundamentally different models. The NRLMSISE-00 (Naval Research Laboratory Mass Spectrometer and Incoherent Scatter Radar) model [40] is the most advanced estimation for atmospheric conditions, with regards to composition and partial densities [41].

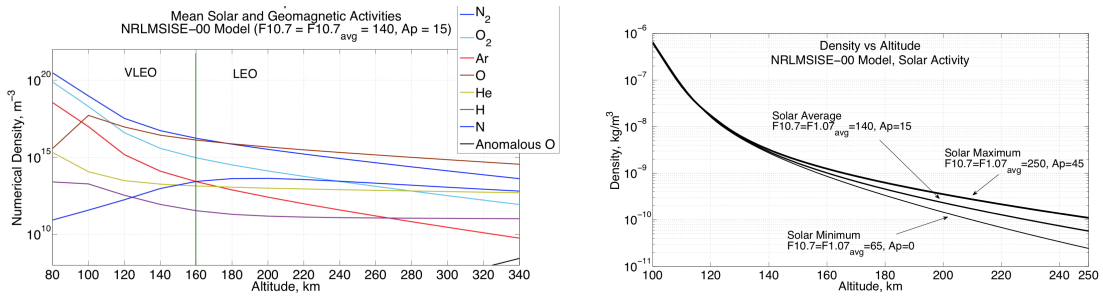

(a) Atmospheric composition

(b) Atmospheric density

Figure 3.2: Atmospheric properties at varying altitudes and solar and geomagnetic activity [42]

This model therefore correctly identifies the various species present in the atmosphere at various altitudes ($N_2, N, O_2, O, He, Ar, H$) as a function of solar and geomagnetic activity. The variations of these species are reported in Figure 3.2.

The model suggests that at lower altitudes, up to 200km, N_2 and O_2 will be the dominant species captured by the inlet and used by the thruster, as well as the main contributors to drag. At increasing altitudes atomic oxygen becomes the dominant particle in the atmosphere together with molecular nitrogen, while the density of all other species is too small to make a significant contribution to a VLEO-operating system.

The second model, JB2006, better models the mean density of the atmosphere [41]. Such parameter is fundamental when estimating the total drag exerted on the spacecraft and thus the total thrust that must be produced by the propulsive system, at various altitudes. The choice of operational altitude is a trade-off between having a high mass flow rate for optimal thruster operation and having low drag values to assure minimum thrust requirements.

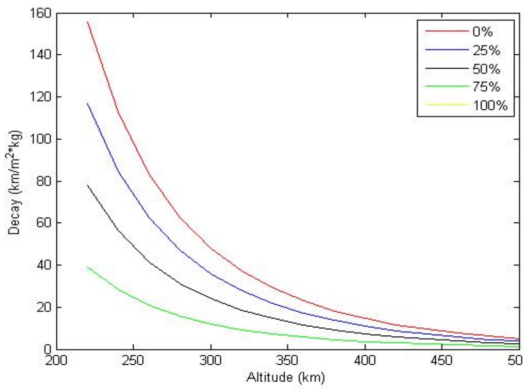

(a) Decay as funtion of percentage of the orbit where drag is compensated by equal thrust

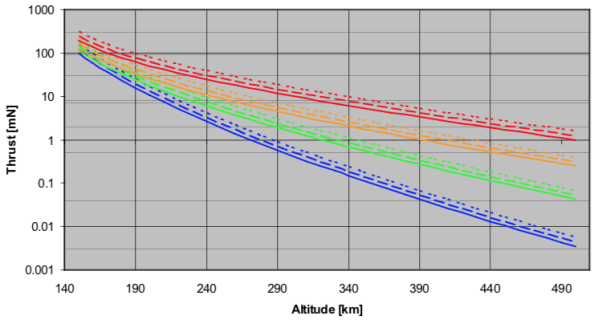

(b) Thrust strategies and solar activity influence

Figure 3.3: Thrust strategies as a function of altitude [2]

As illustrated in Figure 3.3, various thrust strategies have been devised. A continuous line represents a thrust strategy in which the thruster is continuously operating, the dotted line represents a case in which the thruster operates for 2/3 of the orbit, whereas the dashed line signifies a case in which the thruster operates for 5/6 of the orbit. The different colours represent solar activity, from blue, low solar activity, to red, highest solar activity.

Non-continuous thrust strategies require higher thrust levels, thus a continuous thrusting strategy would be preferable. This however, requires the spacecraft to thrust during eclipses, putting a large strain on the power subsystem, leading to large size batteries, thus inevitably increasing costs and weight of the spacecraft [2].

Orbit geometry also influences the power available to, and required by, the system. As mentioned, decreasing the altitude increases drag and thus thrust requirements, leading

to increase in power demands. It is therefore paramount to optimize the orbit shape and spacecraft configuration to maximize the available power. For this reason, 200-250km Sun-Synchronous Dawn-Dusk orbits represent the optimal configuration, minimizing eclipse times, during which the thruster is not operating [2].

Another crucial aspect to consider when analysing operational orbits is particle velocity. The faster the particle incoming in the inlet, the less residence time inside the chamber which results in lower ionization probability. Moreover, a higher exit velocity, therefore specific impulse, is required to produce the same amount of thrust when faster particle velocities are faced.

Particle velocity in the inlet can be estimated as the sum between the particle's *thermal velocity* and *free flow velocity*. The former can be derived as:

$$v_{th} = \sqrt{\frac{2k_B T}{m}} \tag{3.2}$$

In which k_B is the Boltzmann constant, T is the temperature and m is the particle mass. Whereas the latter can be derived by consideration on orbit geometry, hypothesizing a circular orbit, the free flow speed is given by:

$$v_{ff} = \sqrt{\frac{GM_E}{R_E + h}} \tag{3.3}$$

Where G and M_E are respectively Earth's gravitational constant and mass, R_E is the radius of the Earth (6371km on average) and h is the operational height of the orbit. Figure 3.4 depicts these speeds at varying altitudes.

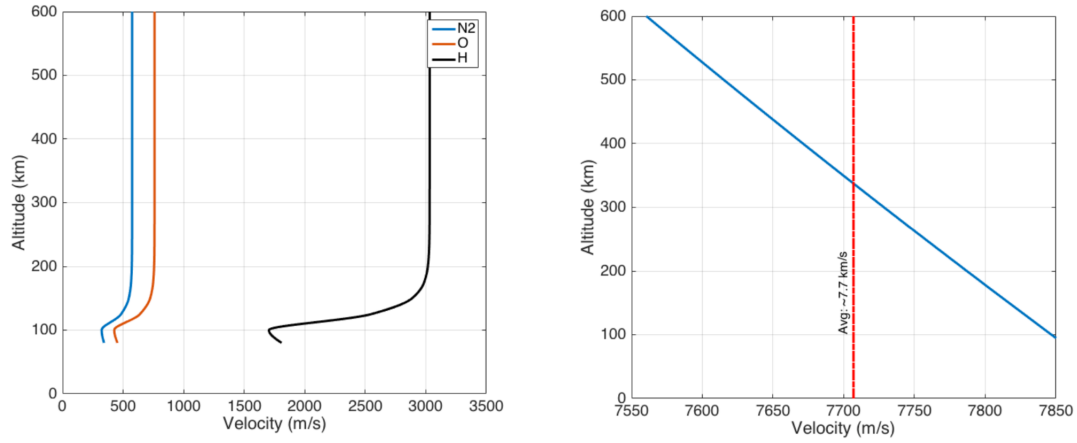

(a) Thermal velocity

(b) Orbital velocity

Figure 3.4: Particle velocities as a function of altitude [43]

Other than the difficulty in ionizing molecular propellants and sustaining an efficient plasma discharge, another major challenge that air-breathing electric propulsion faces is

the capability of effectively reproducing a representative environment for ground testing [1]. This implies the need to provide a very rarefied and hypersonic flow as to the thruster.

As previously illustrated by Figures 3.2 and 3.4 this entails densities of $10^9 - 10^{13}$ particles per cm^3 and velocities in the order of 8km/s between 100-200km of the incoming propellant flow. It is dutiful to highlight that these values are notably higher than those faced in this experiment, in which the propellant flows at most at sonic velocities (350m/s).

An interesting solution to this problem has been devised by SITAEL [1]. This entails the use of a second Hall thruster, defined as a *Particle Flow Generator* (PFG), running on a $1.27N_2 - O_2$ mixture to generate a plume whose characteristics, such as particle density and velocity, resemble the desired incoming flow to the primary Air-Breathing Hall thruster that is tested.

For such reason, a 1kW-class HT5k Hall thruster's plume has been analysed when running on Averaged Mass Flow Rates (AMFR) of 4.3 to 4.7mg/s of the above mixture and the following results obtained [1]:

- Particle density: $4.4 \times 10^{10} - 1.6 \times 10^{14} cm^{-3}$
- Particle velocity: 9-13.7km/s

These results seem to match the expected flow characteristics at the 100-00km operating altitude, however, SITAEL has underlined that this particle flow generating technique does inevitably present some major limitations:

1. These values indicate only the averaged properties of the plume which is actually composed of various species such as faster ions and slower neutrals.
2. HT5k operation on atmospheric propellant shows some instabilities in the operational ranges analysed
3. The HT5k cathode operates on xenon, therefore the background environment on the chamber will inevitably contain some xenon atoms which may influence results.
4. The PFG plume will exert a certain force on the Air-Breathing thruster that is placed directly behind it.

3.2 Results with molecular propellants

3.2.1 Performance Simulations for Typical Design

Numerical simulations developed at SPPL by Fernandez et al [44], Scharfe et al [45] and later adapted by Cha [35] to molecular propellants, allow to model plasma behaviour in Hall thruster, thus predicting results and allowing for more efficient design. In the following section, these simulations will be briefly explained and relevant results shall be presented.

The simulation has been tested on the Stanford Hall Thruster (SHT) geometry, this thruster presents a typical SPT-type configuration, optimized to operate on xenon. The model adopts a 2D hybrid particle-in-cell (PIC) technique to simulate the plasma in a plane spanning from the anode (initial condition of potential $\Phi = \Phi_a$) to the plume, setting the cathode potential ($\Phi = \Phi_c$) as the boundary condition [35], as illustrated in Figure 3.5.

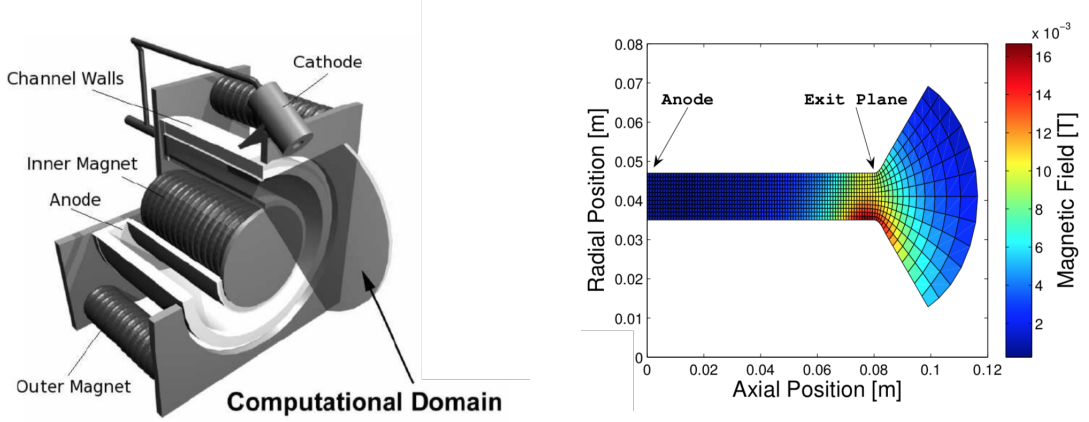

Figure 3.5: Simulation domain [35]

This technique is defined as a hybrid solver as it combines the PIC method for neutrals/ions with a fluid description of electrons to reduce computational costs of a full PIC simulation. The PIC method employs Monte-Carlo simulations to track the motions of a discrete number of collisional particles in the computational domain.

Simulations performed by Cha [35] and illustrated in Figure 3.6, highlight the aforementioned difficulty in ionizing nitrogen as opposed to xenon. Observing the figure on the left, in proximity to the anode (position = 0m), the density of neutrals depends on the mass flow rate as well as particle mass. Intuitively, moving towards the cathode (position = 0.12 m) results in a reduction in density of neutrals as a consequence of ionization. However, as the xenon neutrals are approximately zero at the exit plane (position = 0.08m), a considerable amount of nitrogen atoms exit without being ionized and is unaffected by the mass flow rate.

This result is mirrored when looking at plasma densities and the effects of an increase in mass flow rate. As the neutral density decreases along the channel, the plasma density must obviously increase, with the peak located in the ionization region, where the magnetic field is maximum, in proximity to the exit plane for this thruster configuration. When operating with nitrogen the peak is visibly lower, although it increases with mass flow rate, the peak is almost three times lower than xenon at lower mass flow rates. Such reduction in plasma density is inevitably reflected in a degradation of performance, such as lower efficiencies and thrust levels.

The effects of the lighter N_2 particles are demonstrated in Figure 3.7, as axial ion and neutral velocities are simulated. As previously considered, the smaller mass results in

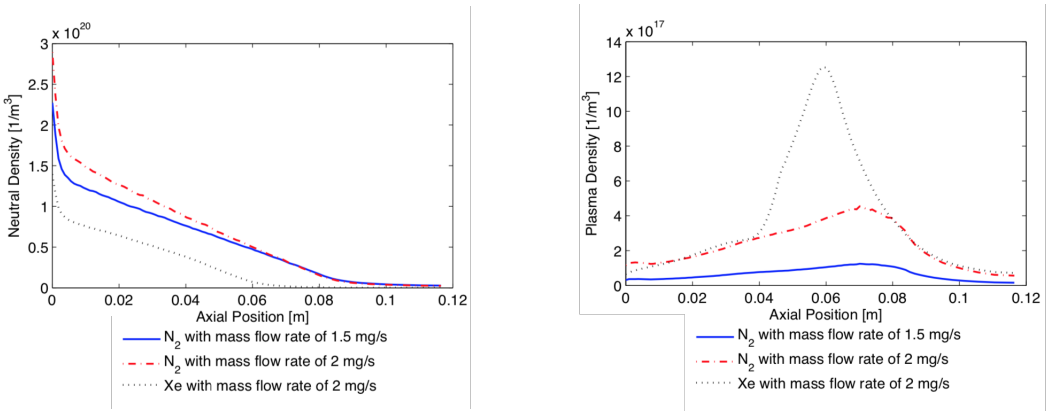

(a) Neutral density (b) Plasma density

Figure 3.6: Simulation for N_2 ionization along thruster chamber [35]

faster particles moving through the channel and negatively affecting the ionization rate. It is evident that the mass flow rate does not affect ion velocity, as these accelerate as a result of an applied potential. The mass flow rate however, does affect the neutral velocity as it results in an increase of pressure upstream leading to higher velocities.

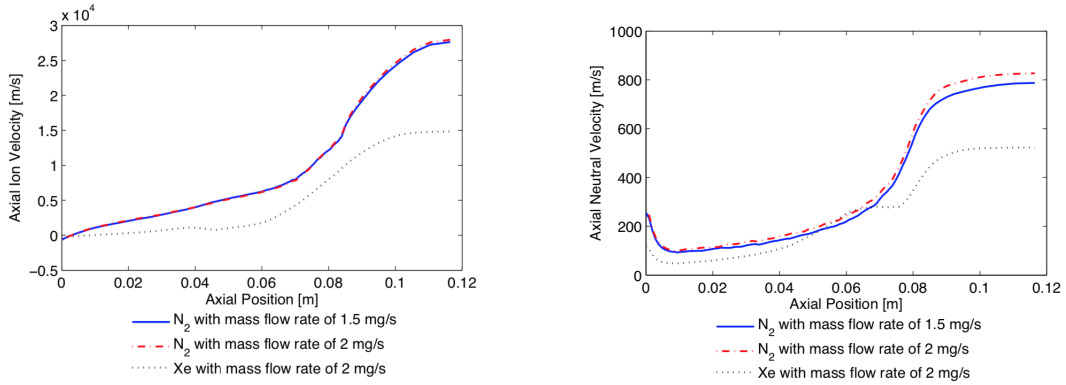

(a) Axial ion velocity (b) Axial neutral velocity

Figure 3.7: Simulation for N_2 velocity along thruster chamber [35]

Cha's simulation culminated in the estimate of performance parameters for the SHT thruster analysed. The results reflect a degradation in performance as a result of the lower ionization rates of N_2.

Propellant	Mass Flow Rate (mg/s)	Thrust (mN)	Global efficiency	Specific impulse (s)
Xe	2	28	23%	1446
N_2	1.5	7	5%	450
N_2	2	21	11%	1054

Table 3.3: Simulated performances for N_2 fuelled Hall thruster [35]

The results of the simulations indicate that a thruster designed for working with xenon behaves poorly in the presence of nitrogen. Increasing the mass flow rate increases ionization as previously explained, thus better performance is obtained. However, in order to make this technology competent a new design must be studied, optimized for the faster and harder to ionize nitrogen particles.

3.2.2 Plume analysis

Ion plume investigation using a Wien filter on Stanford's Z-70 SPT-type thruster has been conducted by Gurciullo et al [36]. A Wien filter, or E × B probe, is a pass-band velocity filter that detects charged particles and allows the estimation of the velocity of such ion species. Moreover, if the ion acceleration voltage is similar between the species such probe allows the recognition of the ion species according to their mass to charge ratio. The relevant results shall be briefly illustrated and commented to understand the plume composition of an air-breathing Hall thruster and the influence of the various ion species on overall performance.

The thruster initially ran on a mixture of Xe and N_2, the xenon present allowed to sustain the discharge as the SPT-type thruster was unstable if no xenon was present at such low potentials. The results indicate the presence of five main ion species ($Xe^+, Xe^{2+}, Xe^{3+}, N_2^+, N^+$), moreover as previously predicted, N_2^+ is the dominant species in nitrogen.

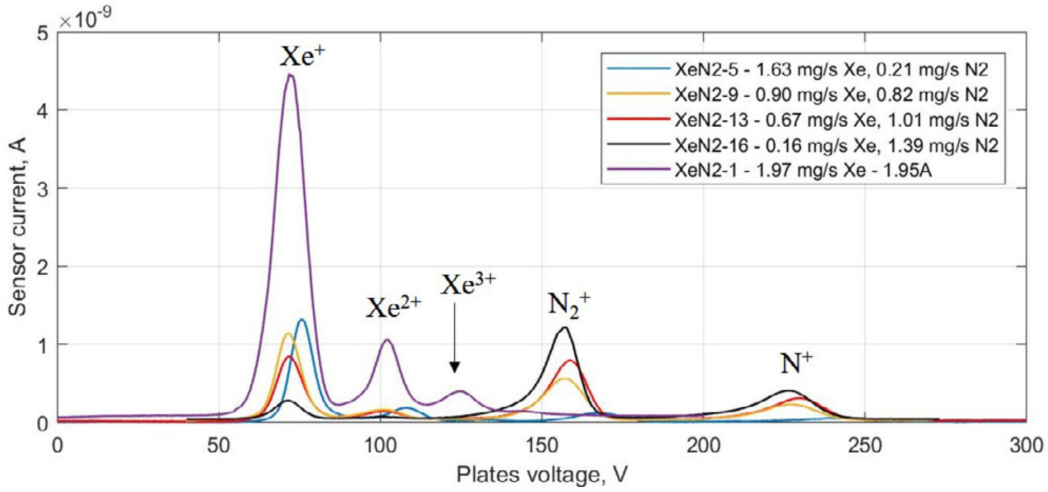

Figure 3.8: Wien filter spectra at varied mixtures flow rates compared to Xe only case (magenta line) [36]

The effects of mass flow rate can be directly observed, as ionization increases and as a result higher currents are achieved. The magenta line shows the benchmark performance with xenon only at similar operational conditions, not only is it possible to observe the evident degradation resulting from a reduction in current, the presence of nitrogen also perturbs and modifies the distribution of the xenon peaks.

Figure 3.9 illustrates the ion density fraction of the cases examined in Figure 3.8. As previously highlighted, a decrease in the xenon mass flow rate to nitrogen mass flow rate

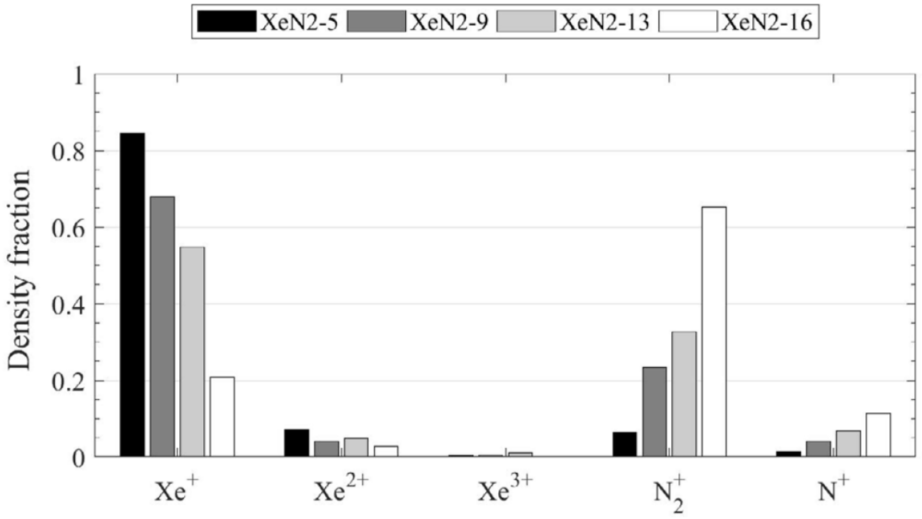

Figure 3.9: Ion density fraction at various Xe to N_2 mass flow rate ratio [36]

ratio generates a decrease in xenon ion species and increase in nitrogen ions. The density fraction is fundamental when calculating the contribution of each species to performance parameters.

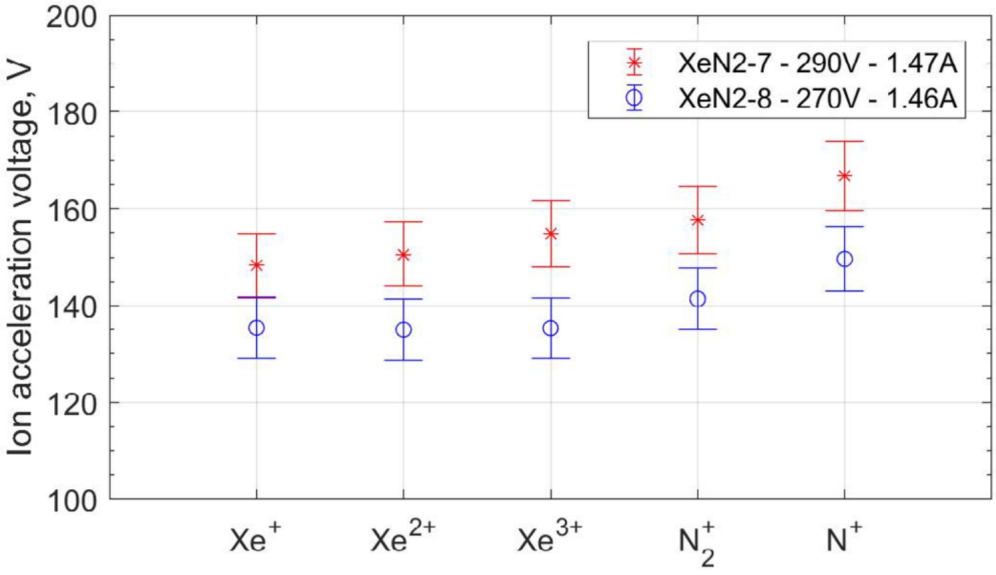

Figure 3.10: Ion acceleration voltage [36]

A very interesting dynamic in the ionization of nitrogen has been observed when studying the accelerating potential of the ion species. Figure 3.10 suggests that N_2^+ and N^+ ions are accelerated to higher energies than those of the family of the heavier xenon ions. This results from the fact that nitrogen ions would be created further upstream, so at higher potentials, than xenon ions.

This finding would be in contrast to what was previously explained, that the lighter nitrogen atoms are more difficult to ionize as a result of their smaller impact cross sections

and residence times, therefore one would expect lower potentials than xenon. This result has yet to be explained and further investigation is required as to identify the causes of such finding, physical or instrumental errors.

Similar experiments have been conducted with xenon-air mixture as propellant, the main species present are $Xe^+, Xe^{2+}, Xe^{3+}, O_2^+, O^+, N_2^+, N^+$. Accounting for only 21% of the air mixture and weighing roughly the same to nitrogen, the presence of oxygen is not expected to disrupt the trend analysed so far. Being slightly heavier than nitrogen, oxygen peaks are expected to be found at lower velocities in the analysed spectrum.

Figure 3.11 shows the resulting spectrum obtained when running on an a mixture of air and xenon. As was the case with nitrogen/xenon mixtures, as a result of the introduction of air, xenon peaks drastically reduce as N_2^+ and O_2^+ peaks start emerging.

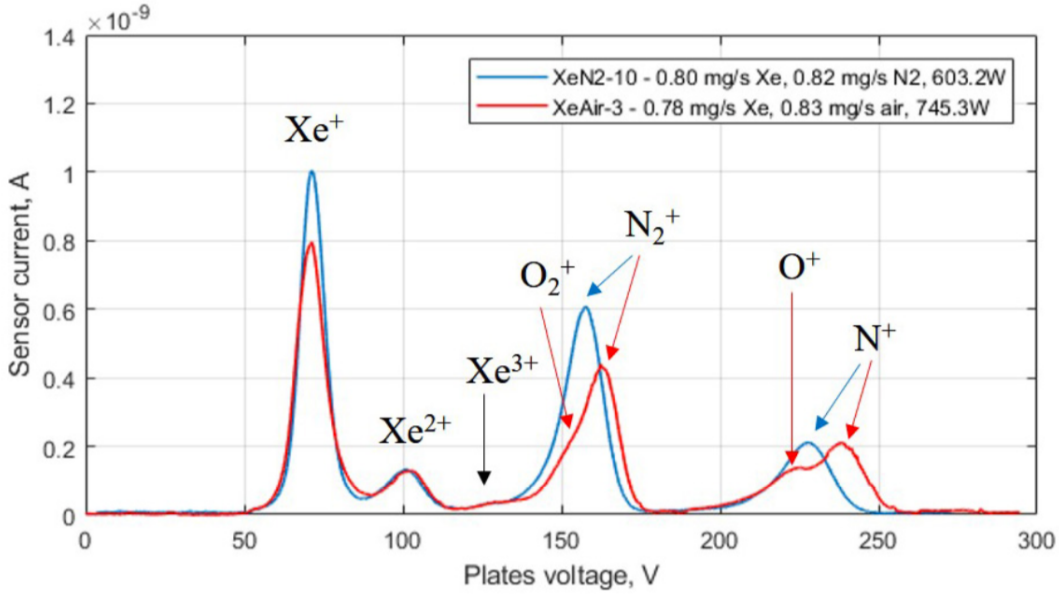

Figure 3.11: Wien filter spectra for air/xenon mixture compared to nitrogen/xenon [36]

As expected, the peaks of the heavier oxygen atoms are located at lower plate voltages as the ions accelerate to lower velocities than nitrogen atoms. Consistently to what was unexpectedly observed in previous runs with xenon/nitrogen mixtures, the lighter N^+ and O^+ ions seem to experience higher accelerating potentials than Xe^+.

Another insightful result illustrated in Figure3.12, comes from the estimation of the ion velocities as a result of the accelerating potential experienced, as the lighter atomic ions are accelerated to higher velocities than the heavier xenon atoms.

The density fraction of each species present in the plume was calculated and the results are reported in Figure 3.13. Such contribution is fundamental when estimating the thrust of molecular mixtures, as is the case with air, moreover, the effects of the presence of oxygen can be visualized, as nitrogen peaks decrease drastically when passing to xenon/air mixtures.

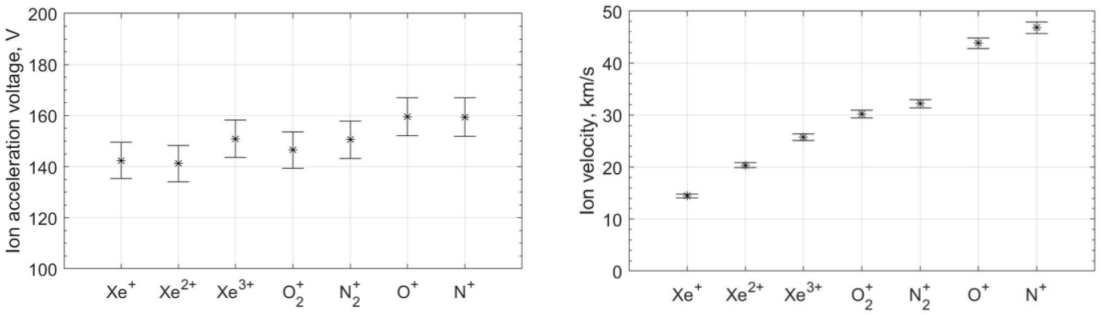

(a) Ion accelerating voltages (b) Ion velocities

Figure 3.12: Ion velocities and potentials derived from xenon/air run [36]

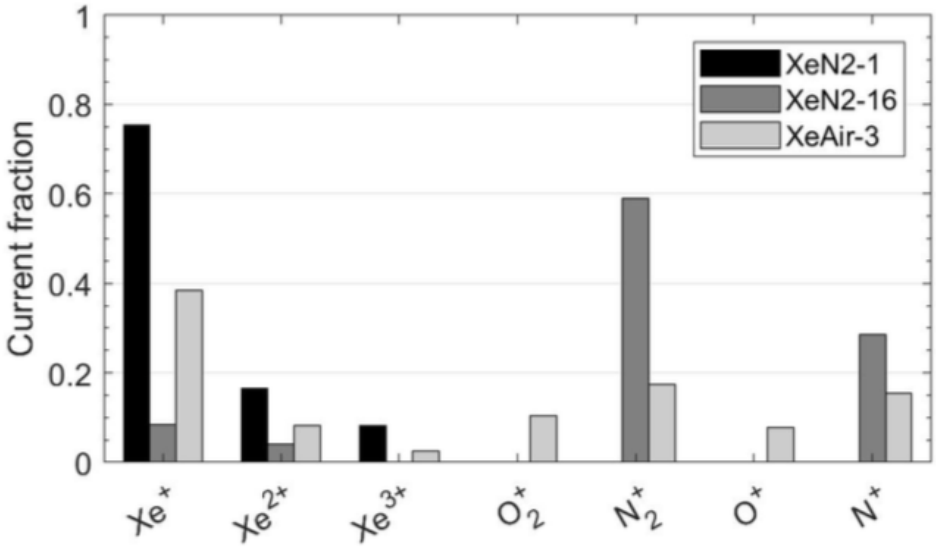

Figure 3.13: Current fraction in xenon/air and xenon/nitrogen mixtures [36]

Figure 3.14 compares two Wien filter spectra, in which all operating conditions between the two runs have been kept identical, expect for the magnetic field intensity.

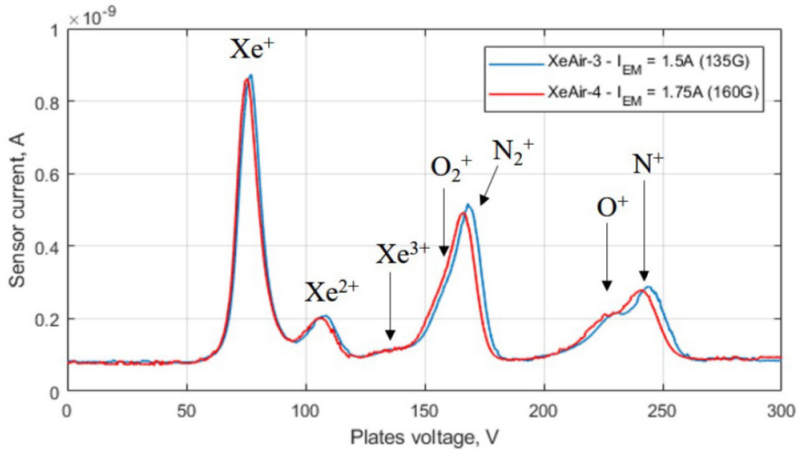

Figure 3.14: Effects of variations in magnetic field density [36]

As evident, an increase in magnetic field (red line) reduces electron mobility, causing a decrease in anode current as well as a deceleration in ion velocity, likely due to a shifting of the accelerating region within the thruster channel [36].

3.2.3 Measured performance with Z-70 thruster

The effects of molecular propellant on electric propulsion has been investigated by students at the Stanford Plasma Physics Lab. These experiments consisted in running the Z-70 Hall thruster with various mixtures of air, nitrogen and xenon. The data from these runs has been analysed via the previously introduced code to calculate the thrust generated and the overall performance of the thruster operating on molecular propellants.

The Z-70 thruster is a xenon-optimised SPT-type thruster, presenting an annular chamber measuring 72mm in outer diamter and 19mm in length, with a magnetic field peaking towards the exit plane. A more accurate design can be visualized in Figure 4.1.

Experiments have been conducted with a mixture of air and xenon, observing the performance at varying compositions of the constituent species. The relevant results are presented in Table 3.4 and the trends shall be analysed in this chapter.

Discharge Potential (V)	Discharge Current (A)	Xenon Mass Flow Rate (mg/s)	Air Mass Flow Rate (mg/s)	Thrust (mN)	Global efficiency	Specific impulse (s)
290	1.8	1.97	0	34.92	0.42	1805
290	1.11	1.97	0.087	30.42	0.23	1504
290	1.8	0.8	0.8	12.66	0.06	792

Table 3.4: Measured performance for Z-70 Hall thruster on Xe-Air mixture

Considering the initial case of the thruster operating on 100% xenon, the results highlight that even a minimum addition of air to the inflow of the thruster greatly influences the performance. The drop in current evident in the second line indicates that, even keeping the mass flow rate of xenon constant and adding a minimum amount of air, therefore increasing the overall mass flow rate, greatly reduces efficiency and performance.

It is plausible to hypothesize that the drastic reduction in performance as a result of the introduction of air may occur as part of the collisions that were essential to ionize the neutrals, now result in a dissociation of the new molecular species present in the mixture, such as O_2 and N_2. This results in a reduction of ions created, which reflects in a decrease in current paired with a much more drastic reduction in efficiency and thrust, even at low amounts of air in the mixture.

As the mass flow rate of air in the mixture is increased, efficiencies and thrust continue their sharp decrease and reach extremely low values of 6% efficiency and 12mN of thrust with a 50%-50% mixture of xenon and air. This is evident in Figure 3.15 in which the two Xe-air mixtures are compared to the reference 100% xenon case.

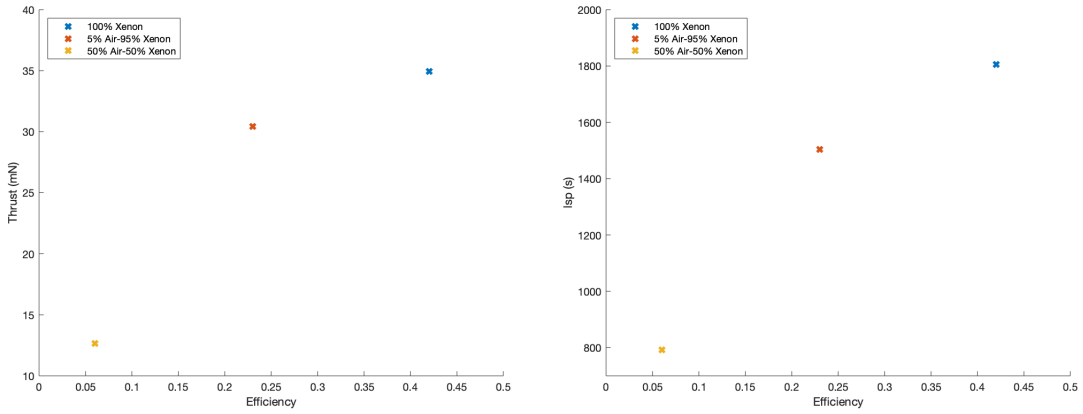

(a) (b)

Figure 3.15: Propulsive performance of Z-70 Hall thruster with varying Xe-air mixture composition

As previously mentioned, increasing the mass flow of air results in an evident decrease in efficiency, better highlighted in Figure 3.16. This is due mainly to the drastic reduction in ionization, as both the O_2 and N_2 molecules present higher first ionization energies than xenon and lighter masses, therefore shorter residence time in the chamber. This reduction in probability of ionization results in a much greater difficulty in sustaining a plasma discharge as air flow is increased. It is evident that the presence of xenon was necessary to avoid thruster discharge quenching.

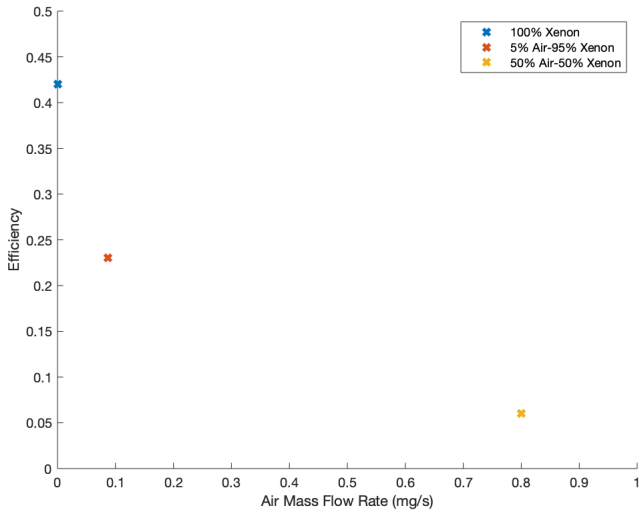

Figure 3.16: Efficiency of Z-70 Hall thruster with varying air mass flow rate

Moreover, the presence of molecular propellants introduces further energy losses that contribute to the reduction in efficiency. Differently from atomic propellants like xenon, molecules present other modes capable of absorbing energy, as a result, a collision between

a molecule and an electron not always creates an ion, but can lead to the dissociation of the molecule thus an energy loss.

With a decrease in the number of ions created and an increase in air flow rate, the reduction in thrust as by equation 2.45 is evident. Specific impulse drops at an even faster rate, as paired to the decrease in thrust is the increase in propellant mass flow rate necessary to sustain a plasma discharge. Such trend is evident in Figure 3.17.

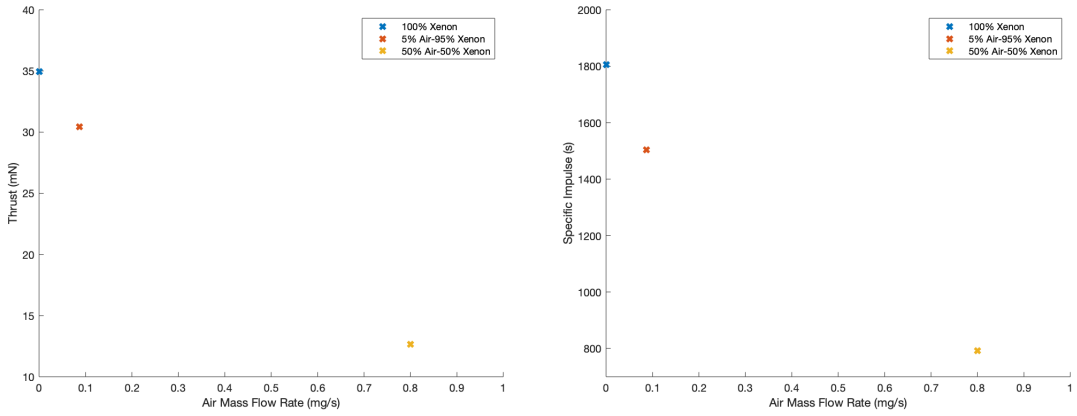

(a) (b)

Figure 3.17: Propulsive performance of Z-70 Hall thruster with varying air mass flow rate

In conclusion, the presence of molecular propellant causes the efficiency to drop from more than 40% to 6% as specific impulse values follow the same trend together with thrust. Moreover, it is fundamental to highlight that the SPT-type geometry of the Z-70 Hall thruster could not maintain a plasma discharge without a minimum presence of xenon. Such behaviour was also observed in similar experiments conducetd by Gurciullo et al [34, 36], in which plasma discharge quenched when xenon flow rate was reduced under 0.16mg/s running on a Xe/air or Xe/nitrogen mixture.

These findings highlight the inadequacy of this technology in exploiting molecular propellants and seem to suggest that the negative trend continues as air flow is further increased, making this type of technology seemingly uninteresting. For such reason, a drastic change in design was necessary to guarantee a plasma discharge and better performance when running on pure nitrogen.

Air-Breathing Hall Thruster

4.1 Optimized thruster design

4.1.1 Long channel concept

The simulated and experimental results presented in previous chapters emphasize the low performances of typical SPT short channel thrusters when operating on nitrogen, resulting from a reduction in ionization rate. It is evident that, in order to make this technology appealing, thruster design optimization tailored to nitrogen's properties is required. The introduction of a long-channel Hall thruster design has been proposed and developed by Seth Winger and other Stanford students working at the Plasma Physics Lab and further optimized and tested by the author.

Hall thruster technology has been chosen principally for its gridless configuration, which allows to ionize and accelerate the much faster neutrals over an extended length. Moreover the greater thrust densities of Hall thrusters, as a result of Child-Langmuir space charge law limitations on Ion Thruster, signify smaller thruster, essential in reducing drag forces when orbiting in the atmosphere.

As previously stated, the main reason for such low performance is the difficulty in the ionization of the lighter N_2 molecules as a result of their higher speeds, thus smaller transient times, and higher first ionization energy. It is therefore evident that in order to enhance the performances when running on nitrogen, the probability of ionization of the molecules must be increased.

This is partially achieved by a variation of the thruster's geometry, as the ionization region should be extended and the channel made longer to increase transient time and ionization [35]. Moreover, as previously noted, increasing the propellant injection rate results in more ionization thus better performances. This increase in mass flow rate is essential to maintain a pure nitrogen plasma discharge.

The key to increase ionization therefore is to widen the ionization, or Hall, region. In classic SPT-type thrusters, like Stanford's Z-70 Hall thruster, the magnetic field density presents a sharp peak in proximity to the exit plane. FEMM (Finite Element Model Magnetics) simulations illustrated in Figure 4.1 highlight the topology of the magnetic field with this

type of design. This magnetic field shape is achieve by placing a 3mm ferromagnetic front plate perpendicular to such region, the dense magnetic field lines assure electron confinement in such thin area.

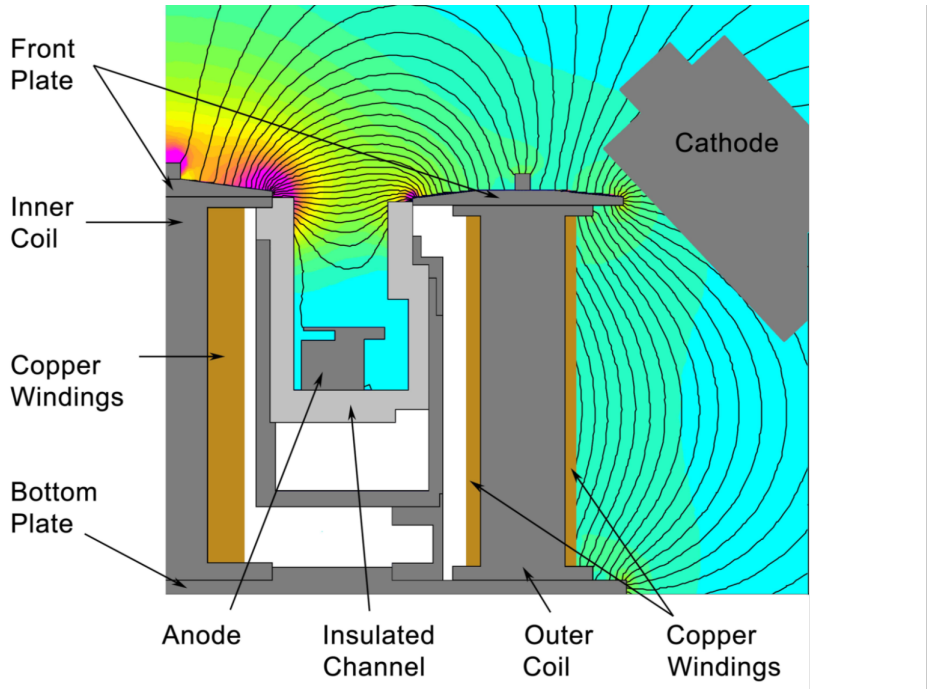

Figure 4.1: Magnetic field topology simulation for Z-70 thruster [52]

To enhance ionization of nitrogen neutrals, the design of typical Hall thrusters has been drastically modified to encompass a wider ionization region. The proposed design is illustrated in Figure 4.2 and shall be analysed in detail in this chapter.

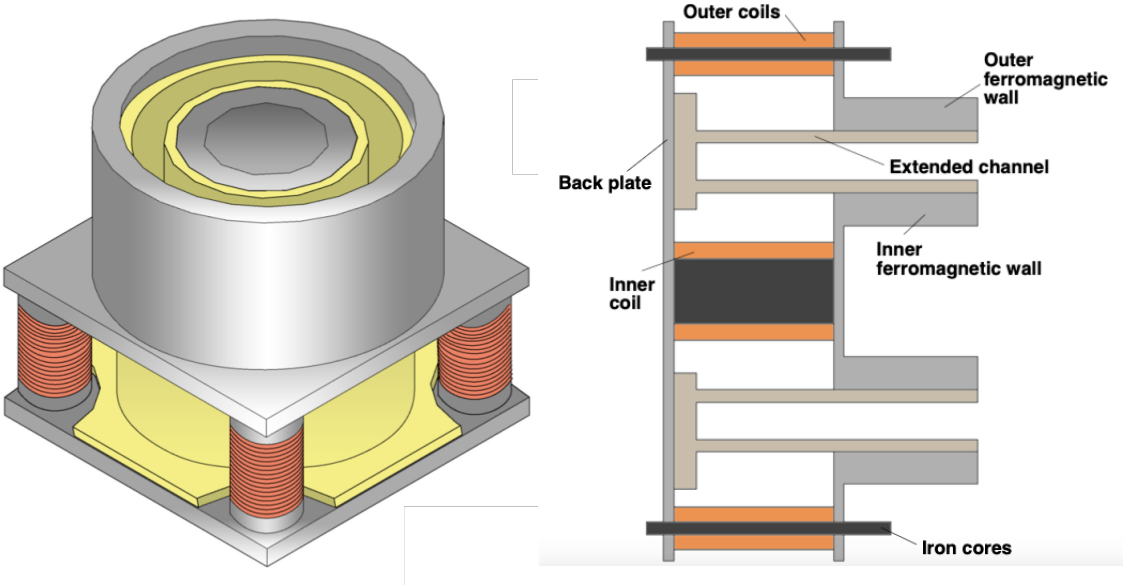

Figure 4.2: N_2 optimized thruster CAD design

In order to achieve generate a wider electron confinement region and prolonged neutral transient times, a longer boron nitride insulating chamber was developed. The new chamber measures 86mm in length and 100mm in outer diameter, with 10mm channel height. These dimensions are significantly larger when compared to the 19mm in length and 72mm diameter of the previous Z-70 Hall thruster.

Coupled with the longer ionization chamber, the thin exit plane was replaced by a ferromagnetic wall extending 46mm around the longer boron nitride chamber, these new elements are visible in Figure 4.3.

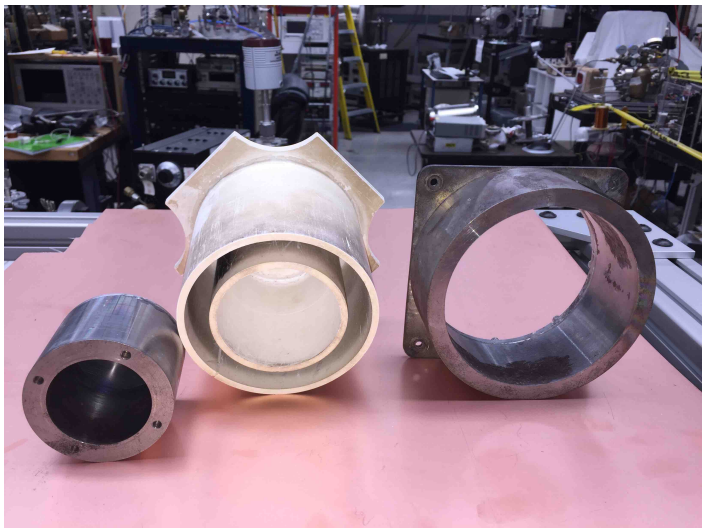

Figure 4.3: Boron nitride extended chamber with outer and inner ferromagnetic walls

An inner ferromagnetic wall was produced from pure iron, identical to the outer wall. The combination of these two conductive layers around the chamber ensures that the magnetic field remains radial and uniform for the whole extent of these 46mm long walls.

To fit the pure iron conductive ring, the electromagnet coils were redesigned and shortened, differently from previous designs, these coils do not cover the full extent of the chamber. The four external coils measure 50mm in length and 17mm in diameter. Similarly the inner coil was shortened to 45mm length and 32mm diameter.

AWG 20 kapton isolated magnetic copper wire was used to produce a total of 240 coils (40 coils in 6 layers) present in each of the five electromagnets. A pure iron core was adopted to enhance the magnetic field generated.

To close the magnetic circuit, a conductive back plate also made from pure iron was introduced. In order to guarantee electrical isolation of the conductive elements introduced from the anode and the plasma, the back plate and the front of the ferromagnetic walls were coated with boron nitride, hence their white colour in Figure 4.4a.

Moreover, in order to improve thruster stability and avoid shorting of the anode to the metal plate, which occurred frequently, the electrical wirings on the back of the thruster

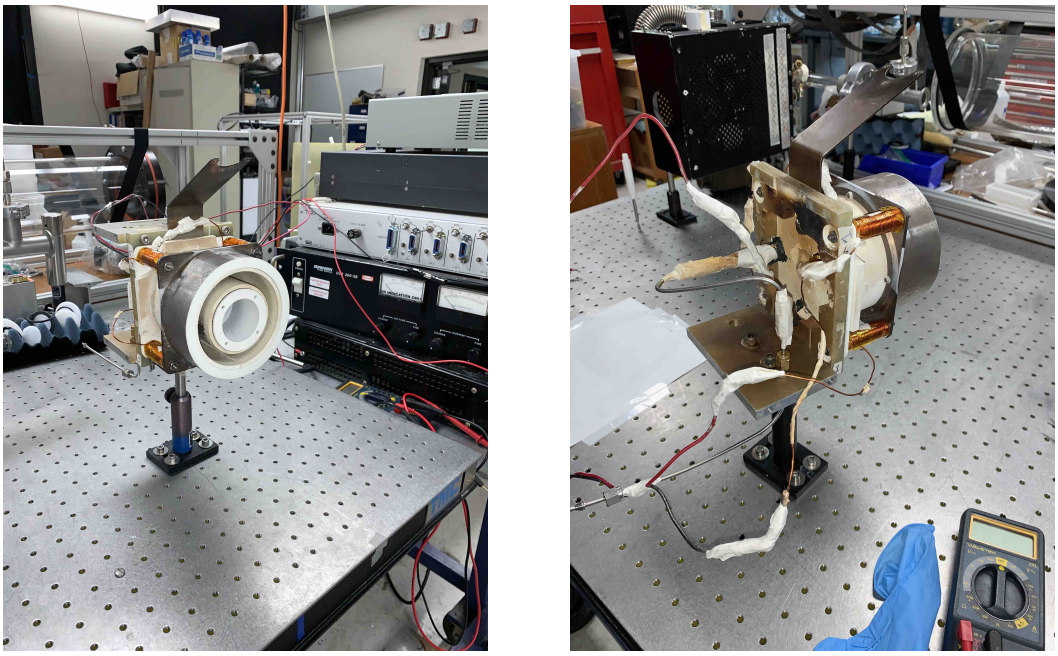

(a) Front end (b) Back end

Figure 4.4: N_2 thruster pictures

were redesigned to allow further space between each wire. Ceramic paste was used to isolate the wires and seal the gas distributor, thus avoiding backflow which led to undesired secondary discharges, these modifications are evident from Figure 4.4b

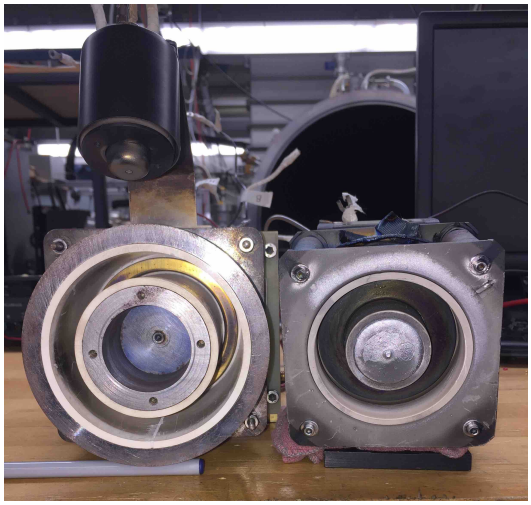

Figure 4.5: Comparison between N_2 thruster (left) and Z-70 thruster (right)

While modifying the ionization chamber, it is crucial to maintain the chamber radius larger than the electron larmor radius and smaller than the ion larmor radius, in order to assure electron confinement and non magnetization of accelerating ions.

This new design was simulated using FEMM and results are shown in Figure 4.6. As desired, the longer insulated chamber coupled to the conductive wall surrounding it generates an extended radial magnetic field region. As the channel and magnetic field are extended,

nitrogen residence time increases and electron confinement is enhanced throughout the channel ultimately increasing the probability of ionization of nitrogen neutrals.

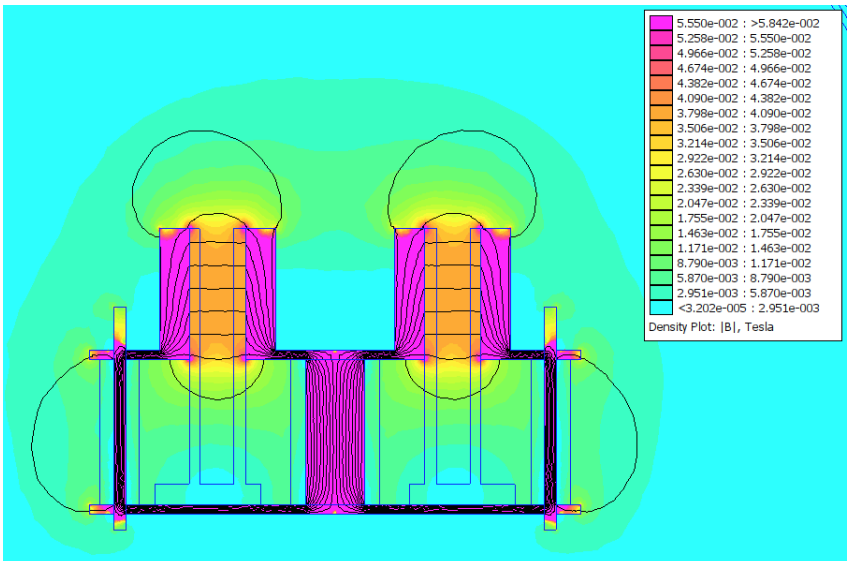

Figure 4.6: Long channel thruster magnetic field topology

The modified magnetic field for the N_2 thruster presents a more gradual and wider magnetic field peak, as opposed to the sharp variations present in the Z-70 configuration, illustrated in Figure 4.1. It is important that the magnetic field drops to zero in proximity to the anode as to not starve it from electrons, this condition would cause instabilities to thruster operation.

A magnetic field density plot in the centerline of the chamber was simulated for a magnet current of 2A and the results are compared to experimental values measured with a Gauss probe. Figure 4.7 illustrates the simulated and measured topology of the magnetic field generated in this new design.

The FEMM simulations seem to match the measured values to a great extent. The wider peak shape was evident during the magnetic field characterization, whereas the measured peak values seem to be slightly lower than the simulated ones.

4.1.2 Operating procedures

The high mass flow rates and powers required have made the operation of the N_2 optimized thruster an arduous task. As previously explained, the thruster has been mounted inside Stanford's Large Vacuum Chamber on a thrust stand. Upon pumping procedures and cathode conditioning, the following steps have been devised to switch on the thruster:

1. After conditioning, cathode heater should be already set to 8A with an approximate voltage of 8.5-9V.

2. Limit cathode keeper to 0.3A and set an initial overvoltage of 500V.

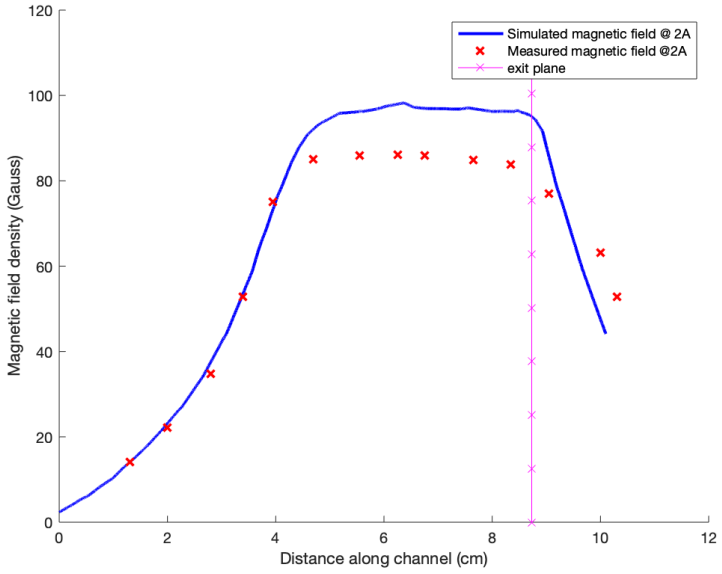

Figure 4.7: N_2 thruster magnetic field density along chamber

3. Set anode potential between 160-300V and limit the current on the power supply to 4A.

4. Start with a low magnet current, typically 0.5A, this can be increased to 3A once the thruster is working steadily.

5. Set an anode mass flow rate (high values are preferred, typically 90-100sccm) and cathode mass flow rate (depends on anode potential, 6.5A is recommended for 200V, this value can increase at higher voltages).

6. Puff the argon flow rate to the cathode. This should ignite the cathode and begin a discharge on the anode. Cathode ignition is evident as keeper voltage drops from 500V to 15-20V as it becomes current limited.

7. Once the anode discharge is stable slowly begin ramping up the magnet current (to a maximum of 3A). As the magnetic field is increased, the anode potential begins rising until it reaches the value set initially. As this happens, the power supply switches to a voltage limited mode and the currents will begin decreasing rapidly, indicating that the thruster is now working in nominal mode.

8. During these operations, the keeper voltage could increase as the densities in the cathode begin decreasing. In order to counter this behaviour, raise cathode mass flow rate until the voltage becomes stable.

9. Once the thruster is operating steady in voltage limited mode and the keeper voltages are stable, the operator can commence to acquire data.

It is fundamental to highlight that the cathode mass flow rates are indicative for a cathode running on argon. If xenon is used values may be lower as the heavier xenon atoms would guarantee a greater plasma density in the cathode.

As reported on the procedures, one of the main problems faced during operation was the switching off of the cathode as a result of its inefficiency in maintaining a plasma discharge. This is likely due to the initial use of argon. In fact, this lighter particle struggles to maintain sufficient densities in the chamber, therefore the only way to counter this phenomenon was to increase the cathode mass flow rate.

The pumping system struggled to face such high mass flow rates, in fact, during thruster operation, base pressures were as high as 1×10^{-4} Torr as cryopanel temperatures rose to 30K. For this reason, it is fundamental that after every run the anode mass flow be diminished to allow for the de-saturation of the panels.

The magnetic field density can be controlled via the magnet's current, the latter can be increased to a maximum current of 3A. Driving higher currents results in overheating of the electromagnets, thus degradation of the kapton insulating wire and eventual shorting of the magnetic circuit. The simulated effects of variation of magnet current on the magnetic field density are illustrated in Figure 4.8. The consequences of this increase in magnetic field intensity on thruster operation shall be highlighted in the following chapters.

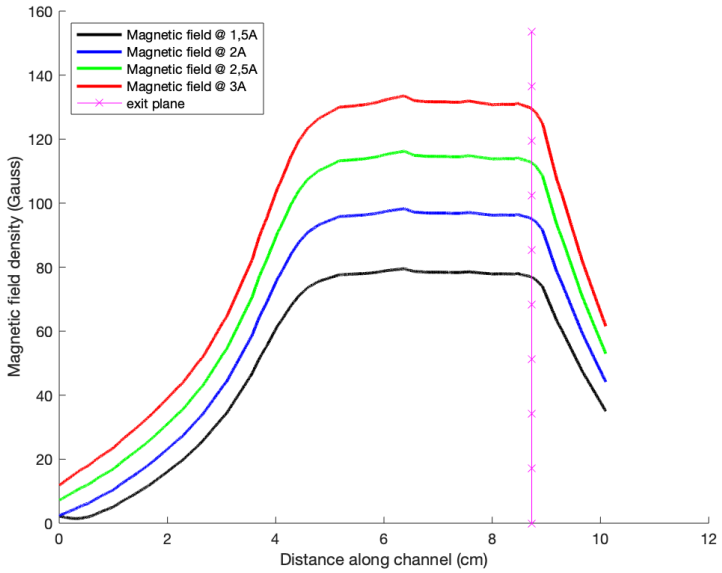

Figure 4.8: Magnetic field intensity at various driving currents

An increase in radial magnetic flux density is also crucial in maintaing low anode currents as to not damage the cathode. This occurs as a result of the reduction in electron mobility towards the anode, higher magnetic field densities encourage more azimuthal drift as well as an increase in ionization probability.

Proper behaviour of the magnetic circuit can be controlled via the circuit characterization in Figure 4.9. Shorting of the circuit as a consequence of overheating results in a decrease in resistance thus lower voltage drops throughout the circuit.

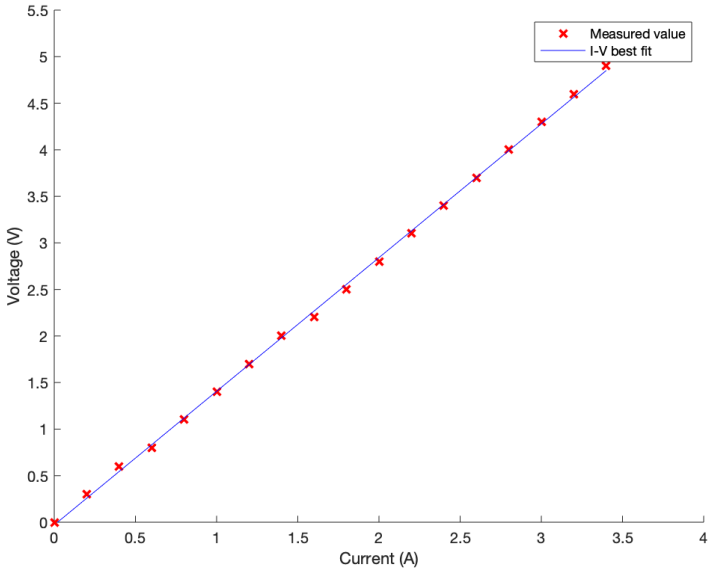

Figure 4.9: Magnetic circuit characterization

The best fit line indicates a circuit resistance of $R \approx 1.44\Omega$. During thruster operation, heating of the magnetic circuit leads to an increase in resistance therefore a drift in voltage drop.

4.2 Simulations for long channel design

4.2.1 Long channel thruster model

In previous sections, equations for thrust have been derived from considerations on ions accelerating in electric fields. Equation (2.46) defines thrust corrected for an air-breathing Hall thruster concept, accounting for the momentum of the inlet flow. In this simplified model however, no inlet has been use ad the gas will be fed directly to the thruster. Therefore neglecting the negative contribution of the second term, the following equation is obtained:

$$T = \gamma I_b \cdot \sqrt{\frac{2m_i}{q}\overline{V}_b} \tag{4.1}$$

In which γ accounts for losses to diverging plume and multiple ionizations, I_b represents the ion beam current, m_i and q are ion mass and charge and $\overline{V}_b$ is the effective accelerating potential. The ion beam current can be rewritten to account for the ion mass flow rate $\dot{m}_i$, which in turn can be tied to the anode mass flow rate by introducing the utilization efficiency:

$$T = \gamma I \left(q\frac{\eta_u \dot{m}_a}{m_i}\right) \cdot \sqrt{2\frac{m_i}{q}\overline{V}_b} \tag{4.2}$$

The γ and $\overline{V}_b$ values can be estimated from typical HET ranges, whereas particle mass to charge ratio can be specialized for nitrogen and xenon. The beam voltage V_b is defined as the anode discharge voltage V_d minus the keeper voltage V_k. Finally, the anode mass flow

rate is taken to be 2mg/s in both cases.

Reference Values	Nitrogen	Xenon
γ	0.75	0.75
$\overline{V}_b$	$0.8V_b$	$0.8V_b$
m_i/q	$2.904 \times 10^{(-7)}$	$1.360 \times 10^{(-6)}$

Table 4.1: Reference values for thruster model

It is therefore paramount to define the mass utilization efficiency η_u. To do so, the mass continuity equation is introduced [48]. Such equation defines the variation of neutral density as a result of ionization along the chanel:

$$\frac{\partial}{\partial_t}(n_a) + \frac{\partial}{\partial_x}(\Gamma_a) = -n_e n_a k_i = -\Gamma_a n_e k_i / v_a \tag{4.3}$$

In which the atom flux $\Gamma_a = n_a v_a$ has been defined as the product between atom density n_a and atom mean velocity v_a. The electron density is ne whereas k_i is the ionization rate which is defined as the product between the ionization cross section of nitrogen Q^{ion} and the velocity of the electrons v_e.

It is plausible to hypothesise a steady state condition for atom density, this results in a first order differential equation for atomic flux Γ_a as a function of space, in which the solution is in exponential form given by:

$$\Gamma_a(x) = \Gamma_{a0} \cdot e^{-\frac{n_e k_i}{v_a} x} \tag{4.4}$$

In which Γ_{a0} is the atom density at $x = 0$ therefore at the anode, in other words it is the total input mass flow rate. The exponential term is defined as the *ionization mean free path*, or penetration distance and is defined as:

$$\lambda_i = \frac{v_a}{n_e k_i} \tag{4.5}$$

This term estimates the length that a neutral has to travel inside the ionization region before actually being ionized. The above equation helps to better understand the previously mentioned difficulties in ionizing the lighter, thus faster, nitrogen molecules, as these will travel a longer distance inside the ionization region before being ionized.

If the ionization region is not adequately long, these neutrals will exit the thruster without being ionized. For such reason, both thruster configurations have been modelled to operate on xenon and nitrogen to simulate the effects of the design modifications. Moreover, as a direct consequence of the higher first ionization energies, the ionization rate of nitrogen molecules will be much lower than that of xenon at a given temperature, as illustrated in Figure 3.1.

Equation (4.4) defines the atomic density as a function of space and can therefore be directly linked to the mass utilization efficiency. In fact, the latter is described as:

$$\eta_u = \frac{\dot{m}_i}{\dot{m}_a} = \frac{\Gamma_i}{\Gamma_{a0}} = \frac{\Gamma_{a0} - \Gamma_a}{\Gamma_{a0}} \tag{4.6}$$

Therefore the mass utilization efficiency can be expressed as:

$$\eta_u = 1 - e^{-\frac{L_i}{\lambda_i}} \tag{4.7}$$

In which L_i represents the aforementioned ionization length. This length is defined by the geometry of the magnetic field. Xenon optimized thrusters such as the Z-70 present a very sharp and narrow peak in magnetic field, around 3mm wide, this results in a short ionization length $L_i \approx 2$mm.

Following design modifications however, the optimized N_2 thruster presents a 46mm extended outer ferromagnetic wall and thus an enhanced magnetic field peak. Accounting for edge effects, the ionization length shall be in the order of $L_i \approx 30$mm evidently much wider than the previous design.

In order to estimate the ionization mean free path λ_i for both thruster configurations, as by Equation (4.5) it is fundamental to determine neutral velocity v_a, plasma density n_e and ionization rate k_i. The neutral velocity can be estimated to be comparable to the speed of sound:

$$v_a \approx \sqrt{1.4 \frac{R}{M} T} \tag{4.8}$$

The adiabatic constant for N_2 has been taken to be 1.4, R represents the gas constant $8.3145 \frac{\text{J}}{\text{mol K}}$, M is the molecular mass, 28×10^{-3}kg/mol for nitrogen molecules and 131.293×10^{-3}kg/mol for xenon molecules, and finally T is the temperature of the particles, assumed to be at room temperature, around 300K. This determines a neutral velocities of:

- $v_a \approx 350$m/s for nitrogen molecules
- $v_a \approx 160$m/s for xenon atoms

It is noteworthy to highlight how the nitrogen flow velocity in this experiment will be much slower than the actual values during in-orbit operation, estimated previously to be around 8km/s. Evidently further testing is required to measure propulsive performance with a hypersonic propellant flow.

The plasma density can be estimated to be in the ranges of 10^{-17} to 10^{-18} particles per m^3 [48], further simulations by Cha [35] explored in the following sections seem to predict similar values at 2mg/s flow rate for both thruster designs. As a consequence of the increased difficulty in ionizing molecular nitrogen, an estimated value of 6×10^{-17} particles per m^3 has been adopted in the long channel modification.

Finally the ionization rate can be estimated by considerations on electron temperatures inside the thruster. Typical electron temperature values in Hall thrusters range from 10eV to 30eV, considering the lower voltages applied and after considerations on Cha's simulations [35] an electron temperature of 15eV has been chosen for nitrogen, which is equivalent to a temperature of 1.85×10^5K. As a result of the reduced collisionality, this value is much lower than in typical SPT thrusters such as the Z-70 running on xenon, for which electron temperature of 25eV are obtained.

Figure 3.1 introduced earlier, simulates electron-impact ionization cross sections to estimate the ionization rate as a function of electron temperature. According to these simulations, the electron temperatures correspond to ionization rates of

- $k_i \approx 0.2 \times 10^{-13}\text{m}^3/\text{s}$ for nitrogen molecules
- $k_i \approx 1.5 \times 10^{-13}\text{m}^3/\text{s}$ for xenon atoms

The estimated values lead to ionization mean free paths of:

- $\lambda_i \approx 29.4$mm for nitrogen
- $\lambda_i \approx 0.7$mm for xenon

These results clearly demonstrate the greater difficulty in ionization of nitrogen, as the neutrals must travel a greater distance before being ionized with respect to xenon atoms. In fact, albeit the extension of the ionization chamber, the distance a nitrogen neutral has to travel in the ionization region before actually being ionized (λ_i) is 98% the total ionization length (L_i) in the long channel configurations. These results moreover, indicate the inadequacy of the Z-70 configuration for operation of nitrogen propellant, as the ionization mean free path is much longer than the available ionization length.

Reference values for xenon indicate ionization mean free paths that account for 35% of the total ionization length. This highlights that, even after design modifications, the extended magnetic field peak plateau that influences the ionization length, is still too small and inadequate to effectively ionize the nitrogen neutrals. Additional development to further extend the channel and magnetic field peak would result in enhancement of nitrogen ionization and an improved performance.

Finally, substituting in Equation 4.7, mass utilization efficiencies can be estimated for both thruster configurations:

- $\eta_u \approx 0.066$ for nitrogen molecules in Z-70
- $\eta_u \approx 0.64$ for nitrogen molecules in extended channel
- $\eta_u \approx 0.94$ for xenon atoms in Z-70

The results indicate a major improvement as a result of the channel and magnetic field extension, as nitrogen ionization is expected to improve from 6.6% to 64%. However, the

mass utilization efficiency of nitrogen molecules in the long channel thruster, is still lower than in typical xenon optimized thrusters as a result of the lower ionization rate of nitrogen and the inadequacy of the ionization region length when compared to the ionization mean free path.

It is now possible to estimate the ion beam current as:

$$I_b = q\frac{\eta_u \dot{m}_i}{m} \approx 4.4\text{A} \tag{4.9}$$

Substituting these values in Equation (4.2), the long channel thruster is expect to produce 29.7mN at a kW, this gives a specific impulse of 1453.9s. Hypothesizing typical cathode and electromagnet values:

- $\mathrm{V_k} = 25\text{V}$
- $\mathrm{I_k} = 0.3\text{A}$
- $\mathrm{V_h} = 9\text{V}$
- $\mathrm{I_h} = 8\text{A}$
- $\mathrm{V_m} = 3.2\text{V}$
- $\mathrm{I_m} = 2\text{A}$

Considering the electron current into the anode to be around 15% of the ion beam current [48] therefore 0.66A, for a total discharge current of 5.06A, the expected global efficiency can be computed from Equation (5.7) and a value of $\eta_\mathrm{G} \approx 0.17$ is obtained.

These results allow for better comprehension of the benefits of these modifications, as the expected thrust and specific impulse values obtained are competitive for electrostatic thrusters. The low efficiencies reflect the decrease in ionization rate.

The positive effects of further increases in ionization length on mass utilization efficiency can be appreciated in Figures 4.10 and 4.11. An increase in L_i enhances ionization, as a results efficiencies and thrust are expected to increase. This result validates the concept of long channel designs to optimize the performance of air breathing electric propulsion and encourages future development of even more extended chambers.

Computed thrust values are higher than what is expected, this is because the model does not take into consideration the effect of dissociative reactions and wall losses. In fact, if more complicated mechanisms such as losses due to collision with walls are taken into consideration, longer channels may lead to a reduction in efficiency and thruster erosion. Such aspect must be taken into consideration when extending thruster length to enhance nitrogen ionization and more elaborate models must be produced, in which the electron energy is correctly computed and the resulting reactions evaluated.

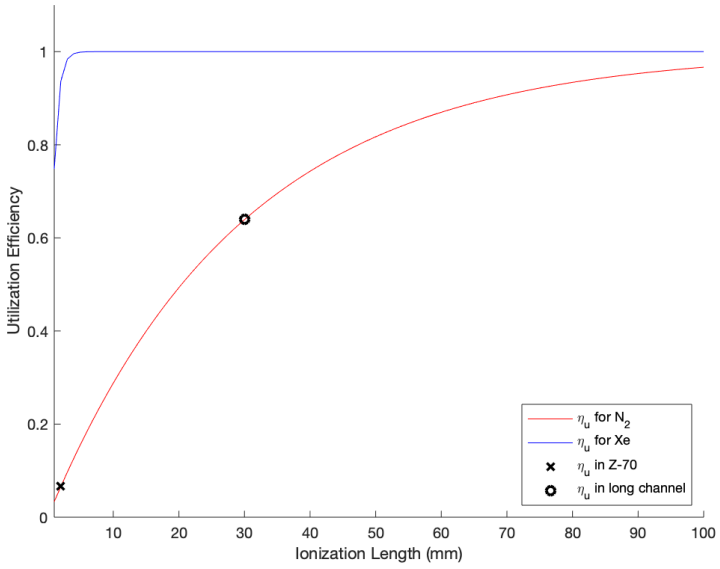

Figure 4.10: Effects of ionization length on mass utilization efficiency η_u

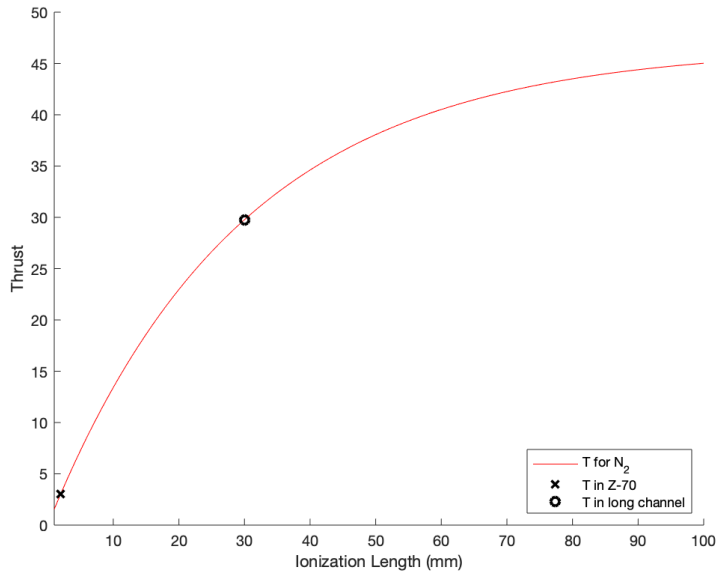

Figure 4.11: Effects of ionization length on thrust for N_2 molecules

Having obtained estimates for plasma properties, another useful insight to model plasma behaviour in the long channel Hall thruster is the Hall parameter. This is essential to understand the effectiveness of the modified magnetic field in confining electrons. The Hall parameter was previously define as:

$$\Omega = \frac{\omega_B}{\nu_c} = \frac{qB}{m_e n_n Q v_e} \tag{4.10}$$

Having previously estimated n_e and $k_i = Qv_e$, defining electron rest mass as $m_e = 9.109 \times 10^{-31}$ and having simulated and experimentally verified the radial magnetic field, the Hall

parameter along the thruster chamber can be immediately obtained. This is illustrated in Figure 4.12.

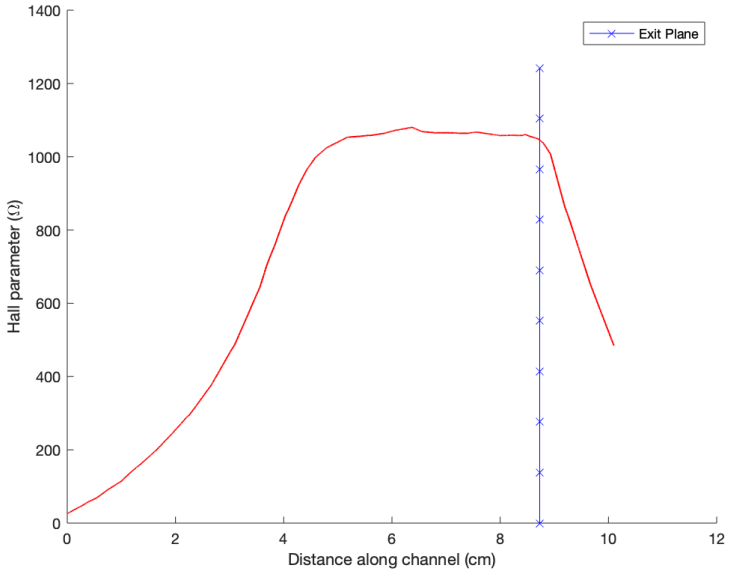

Figure 4.12: Hall parameter along thruster axis

Elaborating on electron confinement, in order to effectively ionize the propellant it is fundamental that the electron residence time in the ionization region (t_r) is comparable, if not greater than, the time between ionizing collisions (t_i) [47]. Hypothesizing that each collision leads to ionization of a neutral, which unfortunately is not precise in the case of molecular propellants, the latter is simply the inverse of the collision frequency:

$$t_i = \frac{1}{n_e k_i} \approx 83.3\mu\text{s} \tag{4.11}$$

The electron residence time on the other hand can be expressed as the ionization length divided by the axial electron drift:

$$t_r = \frac{L_i}{v_{e,\perp}} \tag{4.12}$$

The axial electron diffusion occurs as a result of collisions and is therefore determined by the Hall parameter:

$$v_{e,\perp} \approx \frac{1}{\Omega} v_\theta \tag{4.13}$$

In which v_θ is the azimuthal motion of the electrons as a result of the $\overrightarrow{E} \times \overrightarrow{B}$ field and is determined by:

$$v_\theta = \frac{E_z}{B_r} \tag{4.14}$$

In the ionization region, the axial electric field is determined by the potential drop as a result of the plasma sheath, which is aproximately equal to half the electron energy [47]:

$$q\Delta V \approx \frac{1}{2} k_B T_e \tag{4.15}$$

From which the axial electric filed in the ionization region can be determined:

$$E_z \approx k_B T_e q L_i \tag{4.16}$$

Therefore the electron residence time can be estimated as:

$$t_r \approx \frac{q L_i^2 \Omega B_r}{k_b T_e} \approx 637 \mu s \tag{4.17}$$

The ratio t_r/t_i is about 7.6, illustrating that the electrons reside in the ionization region sufficient time to ionize the neutrals. The simulated performance values for the long channel thruster running on nitrogen are higher than expected. The simplified model does not take into consideration the effects of dissociation or wall losses, in fact the model predicts that all collisions result in ionization, which is a correct estimate only for xenon atoms.

4.2.2 Performance simulations

The new optimized magnetic field profile was implemented in Cha's simulation [35] to investigate the effect such alteration. The propellant mass flow rate was varied from the nominal 1 to 3.5 mg/s to verify the effect of such variation on thruster performance.

The first crucial aspect to observe from Cha's simulations is the noticeable increase in simulated plasma density as a result of the wider ionization region. This evidently leads to a reduced number of neutrals crossing the exit plane, as visible in Figure 4.13.

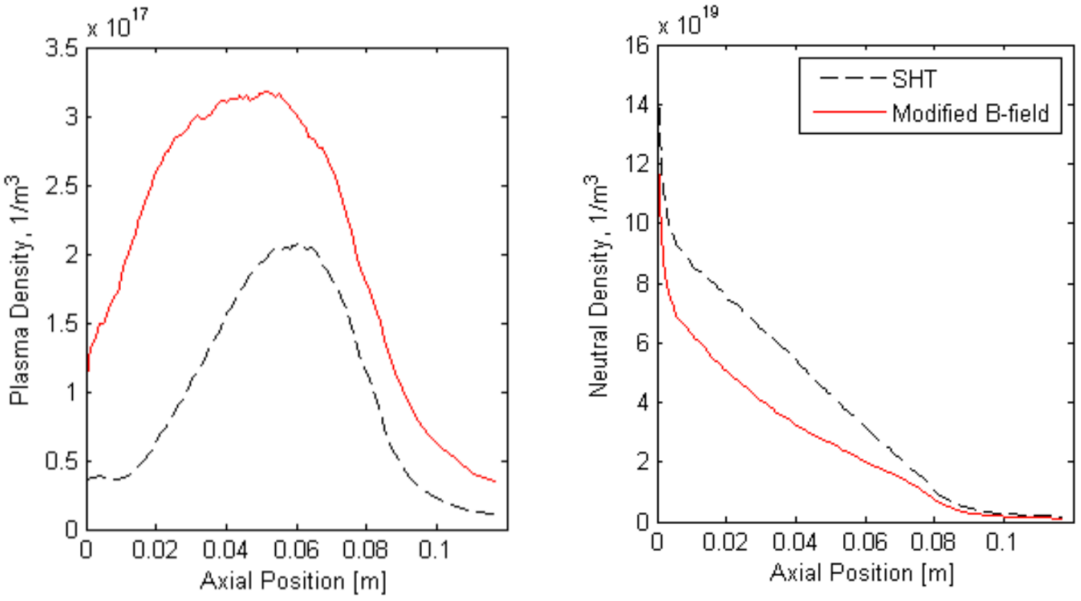

(a) Simulated plasma density

(b) Simulated neutral density

Figure 4.13: Plasma simulations for N_2 optimized thruster [35]

Moreover, the plasma potential decreases more gradually, as is expected as a result of the extended ionization zones, whereas in the SHT it drops sharply in proximity to the exit

plane as a result of the very concentrated zone in which ions are created. Having moved the ionization region upstream, the ions are expected to accelerate earlier, as is visible in Figure 4.14.

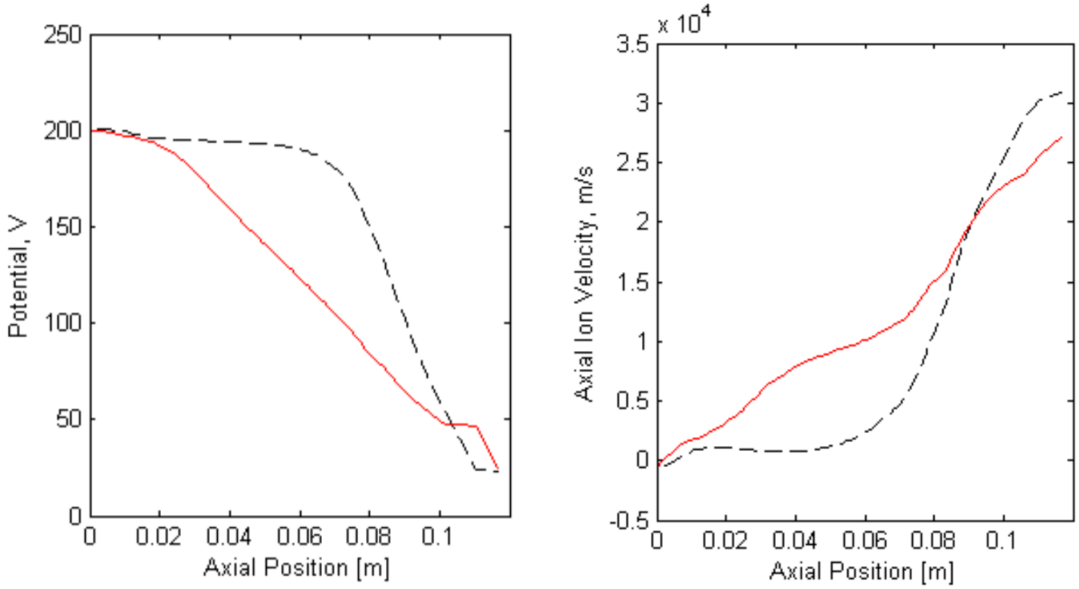

(a) Simulated plasma potential

(b) Simulated ion velocity

Figure 4.14: Simulated velocities in the N_2 optimized thruster [35]

As a result of the modifications, simulated performance was increased, thrust was raised from 6.8 to 12.3mN and efficiency from 3.7 to 7.3%. Moreover, the effects of an increase in mass flow rate were simulated and are illustrated in Figure 4.15.

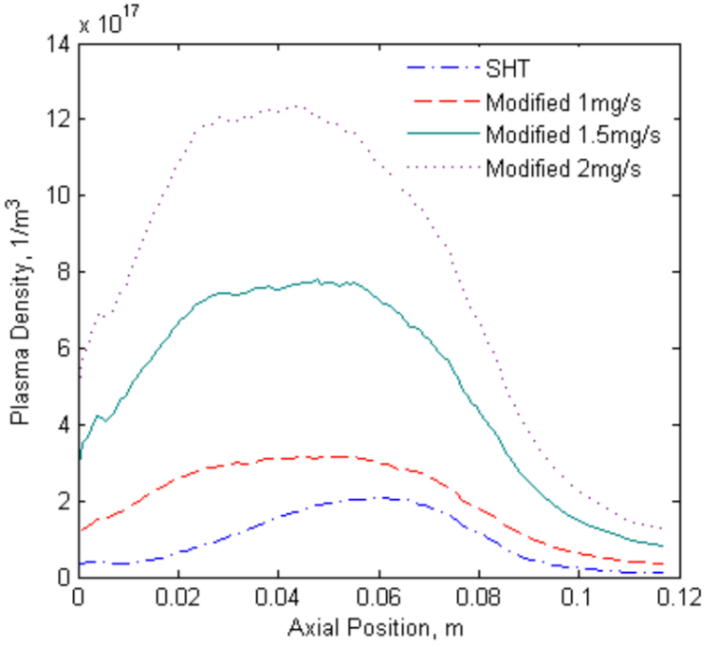

Figure 4.15: Simulated plasma density as a function of mass flow rate [35]

As previously simulated, the mass flow rate has a positive impact on ion production. It is therefore clear that, in order to overcome the lower ionization rate of these thrusters, higher mass flow rates must be adopted than in the case of xenon. It is also noteworthy to observe how the increase in peak plasma density is higher than linear with mass flow rates.

The simulated performances are computed and presented in Table 4.2 as a function of mass flow rate with a fixed anode potential of 200V. An increase in mass flow rate undoubtedly improves thruster performance, linked to the previously mentioned boost in ionization. As a result, currents are expected to rise, whereas specific impulse and total efficiency seem to reach a maximum value and do not improve with higher mass flow rates.

Thruster Geometry	Mass Flow Rate (mg/s)	Thrust (mN)	Global efficiency	Specific impulse (s)	Current (A)	T/P (mN/kW)
SHT	1	6.8	3.7%	692	3.1	9.19
N_2 thruster	1	12.3	7.3%	1324	5.2	8.42
	1.5	24.4	9.5%	1662	10.5	12.84
	2	38.6	11.3%	1971	16.5	11.68
	2.5	53.9	12.8%	2202	22.89	11.79
	3	68.4	13.6%	2328	28.75	11.90
	3.5	79.3	13.6%	2313	33.17	11.96

Table 4.2: Simulated performances for N_2 optimized thruster compared to previous SPT-type geometry[35], both running on nitrogen

These simulated results seem to suggest that the N_2 optimized thruster works best with high mass flow rates to sustain a plasma discharge. Decent efficiencies are achieved when operating at high powers, with over 10% reached at 2kW. As a result of the high mass flow rates, the thrust values result comparable to those achieved by typical xenon propelled thrusters operating at 1kW.

It is interesting to notice how the simulated thrust levels for the long channel thruster seem to be similar to the previously proposed model. In fact, at a 2mg/s nitrogen mass flow rate, 38.6mN of thrust are simulated and 30mN are predicted to the model. As promising as these results may seem, these values are much higher than expected as both these models do not consider numerous factors contributing to losses.

In fact, these shear transport simulations are based on semi-empirical models and are obtained through the fitting of various parameters. For this reason, having developed the simulation without prior operation of the nitrogen hall thruster, thus basing the values on xenon-operating Hall thruster knowledge, these simulations may present performances that do not match the measured values.

Experimental Setup

5.1 SPPL vacuum facility

The research was conducted in Stanford Plasma Physics Laboratory's (SPPL) Large Vacuum Facility at Stanford University. Hall thrusters are mounted inside a 1.5m diameter, 3.5m in length stainless steel vacuum chamber, shown in Figure 5.1. A pumping system guarantees extremely low pressures, in the range of 10^{-5} Torr, during thruster operations.

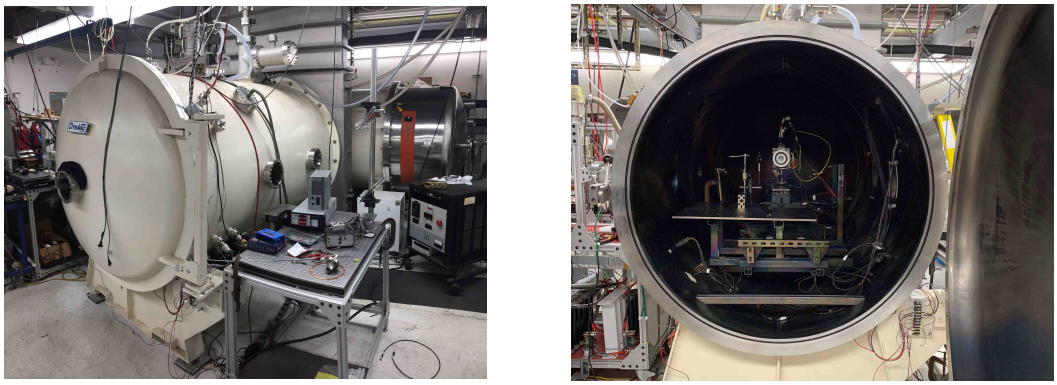

(a) Large vacuum chamber

(b) Open chamber with Hall thruster mounted

Figure 5.1: SPPL Large Vacuum Facility

The chamber employs a two-stage cryogenic cooling system allocated in the T section, capable of attaining temperatures as low as 20K during experiments. Both the cryogenic pumps and the turbomolecular pump are cooled by a filtered cold water closed loop system. A 1.5m gate valve separates the cryopanels from the thruster, allowing for rapid adjustments to the setup. It is fundamental that the vacuum chamber is non-magnetic, so as to not affect the trajectory of the charged particles and the fields inside the Hall thruster.

Maintaining low background pressures is essential for correct Hall thruster operation. Higher pressures enhance electron mobility towards the anode as a result of increased collisions with background neutrals [50]. Consequently, the ionization region will move upstream towards the anode and higher ion velocities inside the discharge channel will be

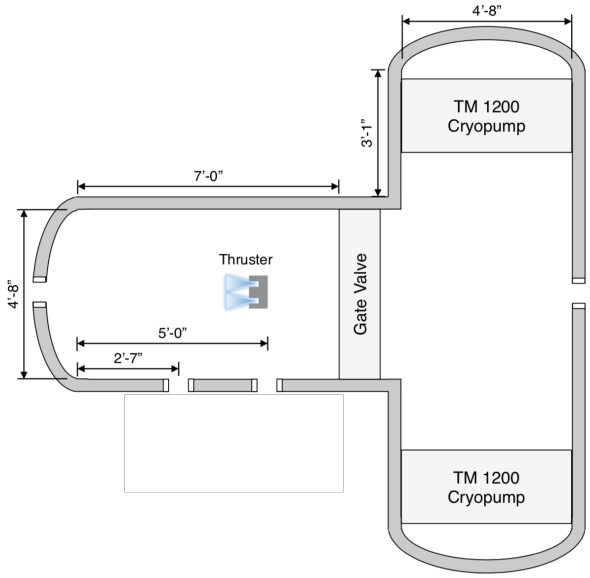

Figure 5.2: Top view schematic of SPPL's Large Vacuum chamber [55]

achieved, although these will eventually converge to the same value after the exit of the thruster as a result of the same total applied potential drop [36].

5.1.1 Pumping procedures

Two mechanical roughing pumps and a turbomolecular pump are used to lower the chamber pressure to the operating range of the cryogenic cooling system, the ensemble guarantees a base pressure of 10^{-6} Torr. During nominal thruster operation, thus with a constant input of mass in the chamber, the turbomolecular pump and the cryogenic panels allow for the background pressure to be maintained at 10^{-5} Torr. The pumping system is illustrated in Figure 5.3.

The first mechanical pump is turned on after closing the chamber and allows to lower the pressure from atmospheric values to less than 9 Torr. Below 9 Torr the second pump, in series with the first, is turned on, while the turbomolecular pump is initially switched off and isolated from the pumping line. The two mechanical pumps lower the pressure to 150 mTorr, after which the turbomolecular pump is introduced in the pumping process.

At such low densities, the mean free path of the molecules inside the chamber is comparable to the dimensions of the rapidly spinning blades of the turbopump, it therefore eases the pumping process by directly scooping the molecules and pushing them from the low pressures inside the chamber to higher pressures outside. While operating, the turbomolecular pump is backed by the two mechanical pumps, connected in series, to dispose of the molecules extracted from the chamber.

The pressure inside the chamber is recorded using a thermocouple gauge sensor and a hot-cathode ion gauge filament, both illustrated in Figure 5.4. The thermocouple gauge sensor can measure pressures as low as 3×10^{-2} Torr. Below this pressure, thus during typical

(a) Mechanical roughing pumps

(b) Turbomolecular pump

Figure 5.3: Pumping system

thruster operating conditions, the thermocouple is no longer precise and the hot-cathode gauge filament must be used.

(a) Thermocouple gauge sensor

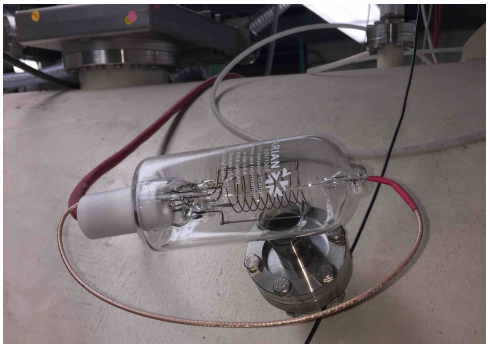

(b) Ion gauge filament

Figure 5.4: Pressure sensors

5.1.2 Cryogenic cooling

The two stage cryogenic cooling system is illustrated in Figure 5.5, it is locate in the T-section of the chamber. The system consists of a first stage shroud that is cooled using a Polycold PFC water vapour chiller and a second stage cryopanel cooled by a closed-loop helium cryopump.

The Polycold helps the cryopumps face the thermal load, lowering the temperature of the panels below the freezing point of water and reaching a temperature of -150^{o}C prior to cryopump operation. During the cooling of the cryopanels the temperature and pressure inside the Polycold chiller increase as the panels reach saturation from frozen molecules, this reduces the efficiency of the system. To mitigate this, the cooling on the panels is achieved through cycling of the chiller.

The cryopumps are fundamental to maintain low pressures inside the chamber. The panels inside the chamber are cooled to temperatures so low, around 20K, that molecules will

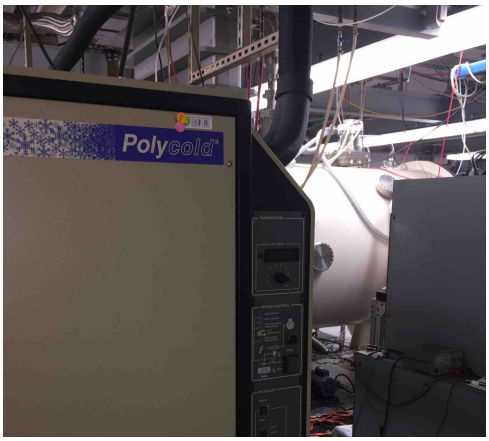

(a) Polycold

(b) Cryopanel

Figure 5.5: Cryogenic cooling system

freeze and adhere to them as soon as they make contact, drastically reducing the chamber pressure.

As temperatures inside the chambers start to rise at the end of each run, molecules that had adhered to the cryopanels' surface will become again free and pressures rise. A small percentage of these molecules however, will remain stuck to the panels and over time this will degrade the effectiveness of the panels to maintain low pressures. Once this efficiency is visible reduced, a set of heaters can be actuated to regenerate the panels, this is achieved by raising the temperatures thus forcing molecules to evaporate.

5.1.3 Power supplies and feed lines

The anode of the thruster is powered by a Power Ten Inc. P62B-3006.6 power supply, whereas for the cathode keeper a Sorensen DCS600-1.7E power supply was adopted. Two additional Sorensen DLM40-15 supplies power the cathode heater and the magnetic circuit.

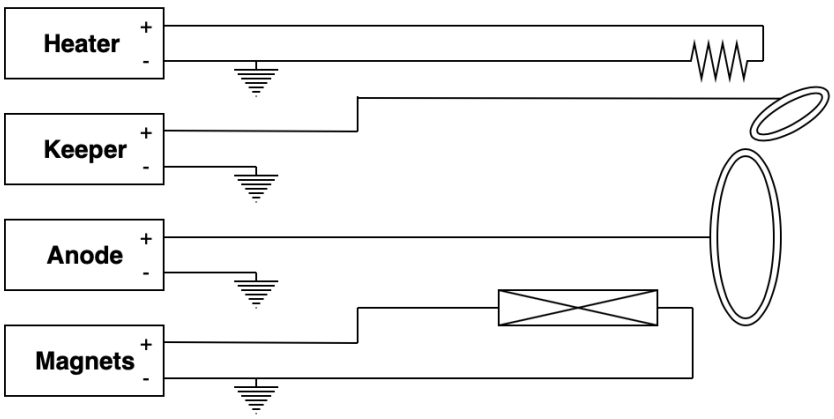

Figure 5.6: Scheme of electric connections

Electrical lines connect the power supplies racked in the work station, shown in Figure 5.7, to the thruster inside the sealed vacuum chamber, as simplified by the scheme in Figure 5.6. All potentials are relative to a common ground which is the body of the vacuum chamber. Finally, two multimeters were connected in series and parallel to the anode power supply to precisely measure respectively the current and voltage of the discharge.

(a) Power supplies racked in work station

(b) Voltmeter (top) and ammeter (bottom) to measure anode discharge

Figure 5.7: Power supplies to the thruster

A mass flow control system allows to manage the propellant type and flow to both the anode and cathode. Two mass flow controllers (Unit Instruments UFC-1200A) allow for argon delivery to the anode and the cathode, respectively with range 0-50sccm and 0-100sccm (Standard Cubed Centimeters per Minute). A third mass flow controller (Ultra-Flow UC2-21S02) is used to deliver air or nitrogen exclusively to the anode, with 0-100sccm range. The system is illustrated in Figure 5.8. The mass flow controller (Unit Instruments URS-100) allows to set and measure the flow on each of these three lines. A bypass line is used to rapidly increase the flow of propellant to the cathode, such procedure is known as a "puff" and eases cathode ignition.

5.2 Data acquisition

5.2.1 Cathode and thruster ignition

The ignition and operation of the thruster and the cathode, is an intricate task. The cathode used is an IonTech HCN-252 Barium Oxide (BaO) impregnated hollow cathode. Once mounted the thruster on the stand and created the vacuum, the first simple operation is to purge the gas lines of any impurity. This typically implies opening all the valves along the gas line, in sequence from the highest pressure to the lowest and expelling a flow of gas for several seconds.

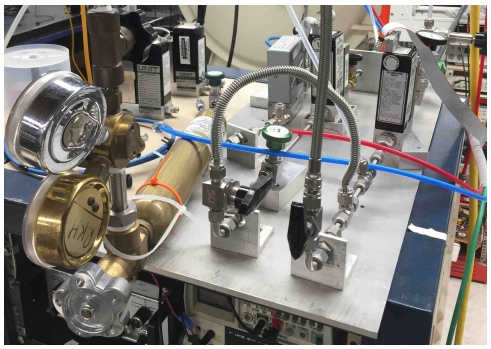

(a) Propellant feed control system with Xenon tank on the left

(b) Anode mass flow controller

Figure 5.8: Mass flow control system

This is followed by the more arduous task of conditioning the cathode heater. This involves ramping up the current to the desired operational value of 8A, thus allowing the heater to reach operating temperatures, for which electrons are emitted by the insert through the thermionic effect.

The procedure shown in Table 5.1 has been devised for cathode conditioning when running on xenon. An identical procedure has been followed when conditioning the cathode on argon, with the exception of the cathode mass flow rate that has been kept constant at 5 sccm throughout the whole operation.

Time (minutes)	Cathode mass flow rate (sccm)	Heater current (A)
5	5	0
10	3.5	2
10	3.5	4
10	3.5	6
10	3.5	7
10	5	8

Table 5.1: Heater conditioning procedure for xenon

Moreover the heater voltage at the beginning and end of each step is recorded to better understand the trends in behaviour of the cathode.

Following cathode conditioning, the thruster must be ignited, this has proven to be an arduous task for the N_2 optimized thruster used and the following procedure has been devised:

1. Heater conditioned, typically around 8A.
2. Set keeper overvoltage and limit the current.
3. Set anode voltage and limit current to cathode requirements.
4. Set initial magnetic field, low fields are suggested to ease ignition.

5. Set anode and cathode mass flow rates.

6. If cathode does not automatically start, puff the cathode flow to ease ignition. Cathode ignition is evident as voltage drops and cathode becomes current limited.

7. The anode should switch on and currents rise, it should be left stabilize for a few seconds.

8. Only when the anode has stabilized and the keeper voltage seems constant should the magnetic field be applied.

Once the thruster is ignited and a steady working mode is found the calibration be executed and thrust computed. Working with such high mass flow rates of nitrogen in order to enhance ionization, it is recommended to shut off the anode gas feed after every run and let the base pressure of the chamber decrease and cryopumps desaturate for optimal performance.

It has been observed that lower anode potentials ease cathode ignition when running with argon. Moreover, it was not possible to raise anode voltage to more than 300V as this was the operational limit of the power supply used.

It is fundamental to highlight that the Large Vacuum Facility struggled to face the increase volume flow rates required by the N_2 thruster. During thruster operation, the chamber settled to base pressures much higher than those registered during xenon operating thrusters, at values in the range of 1×10^{-4} Torr. This evidently hinders optimal thruster operation, increasing collisionality within the chamber, thus reducing electron confinement and ionization.

5.2.2 Thrust stand

In order to evaluate the low levels of thrust generated, the thruster is mounted on a displacement-measuring mechanism called a *thrust stand*. This apparatus, designed by the US Air Force laboratories for Stanford University, uses an inverted pendulum to accurately measure the milli-Newtons of thrust produced by the thruster.

A schematic of such equipment is shown in Figure 5.9. The thruster is mounted on the top part of the stand which, thanks to several flexures, can move relative to the bottom part, the latter being fixed to the vacuum chamber. These flexures, together with a restoring spring and the feed lines connected to the thruster, behave like a spring, with a global elastic constant K, this parameter is fundamental to determine the thrust and is measured during calibration, this concept will be explored in further sections.

The insulator, consisting of a plastic mount, electrically separates the thruster at a floating potential, to the rest of the chamber placed at ground potential. A magnetic damper is introduced to reduce oscillations of the stand and allow the structure to converge to an equilibrium position, easing the direct measurement of displacement.

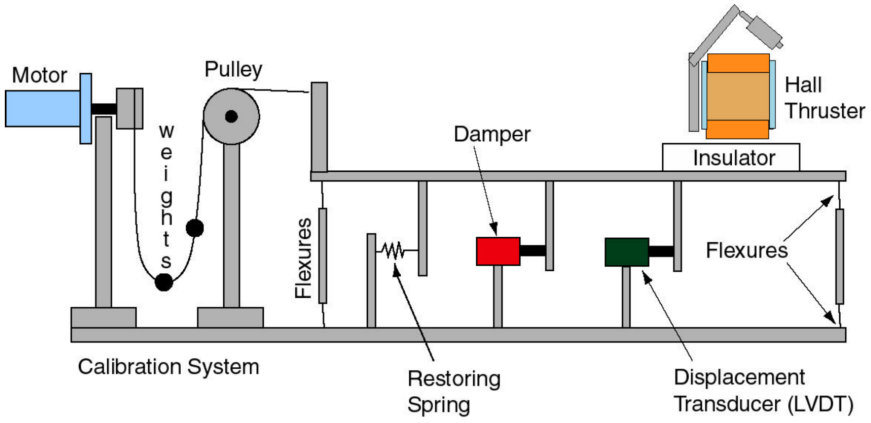

Figure 5.9: Schematic of a thrust stand [51]

A levelling screw, illustrated in Figure 5.10 allows for precise adjustment in the stand's inclination. Finally, a Linear Voltage Differential Transformer (LVDT), produced by Macro Sensors model PR 812, is used to measure the displacement, it measures the change of impedance as a result of the relative motion between a stationary coil and an ferromagnetic core.

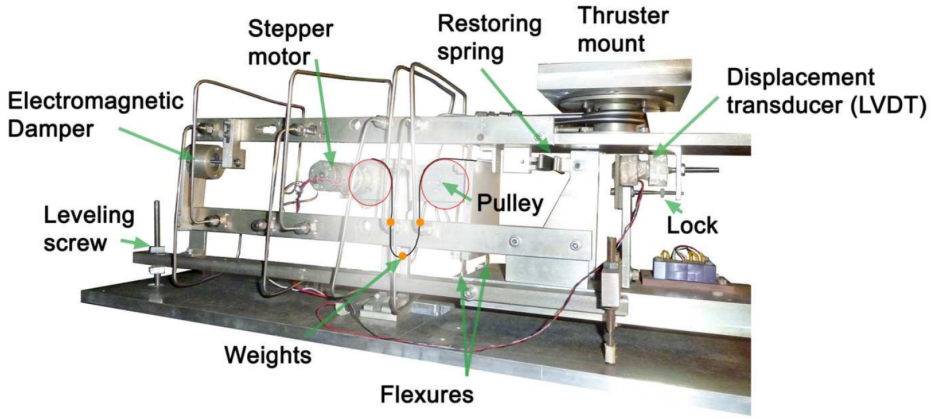

Figure 5.10: Picture of SPPL's thrust stand [52]

The thrust stand therefore functions like a mass-spring system, in which a force F generates a proportional displacement x, therefore at equilibrium the following equation holds:

$$F = K\Delta x \tag{5.1}$$

A direct measurement of the displacement at the equilibrium point produced as a result of the thruster being activated allows for the immediate computation of thrust. In order to do that however, the elastic constant of the whole apparatus must be determined, this is done through calibration and shall be explored in the following section.

Figure 5.11 depicts the thruster mounted on the thrust stand inside the chamber. The

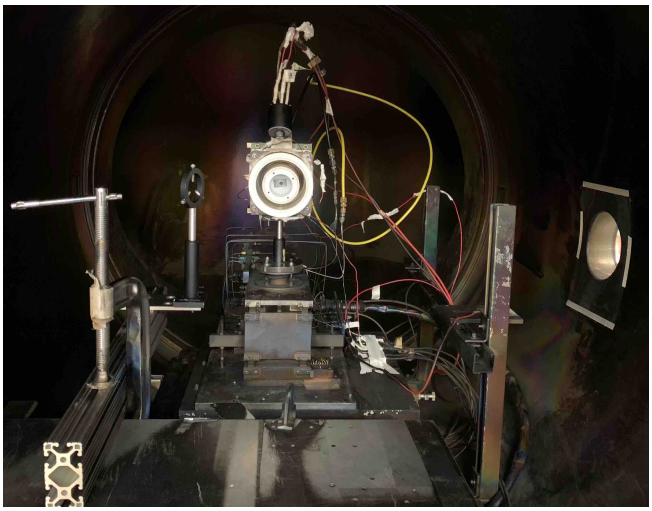

Figure 5.11: Hall thruster mounted on thrust stand

cathode and anode propellant feed lines are clearly visible as well as the electric lines connected to the thruster circuits.

5.2.3 Calibration

As the thruster operates, it exerts a force on the top half of the stand, which is therefore displaced relative to the bottom half. The LVDT measures such displacement returning an output voltage, proportional to the displacement. In order to have precise thrust measurements, it is paramount to determine the elastic constant, this is achieved through the initial calibration.

Calibration is extensively explained by Marcovati [53] and Young [54], this procedure is performed during thruster operation by applying three known forces to the thrust stand and measuring the resulting displacement, or voltage. To improve accuracy, it is fundamental that the three weights applied are of similar magnitude as the thrust produced by the thruster.

These three weights, attached to a chain, are gradually unloaded by a spool operated by an electric motor. Each weight produces a known vertical force (mg), then translated to a horizontal force by a pulley attached to the upper part of the stand. Having accurately measured the weights beforehand, this calibration procedure yields a displacement (or voltage) versus force curve which allows to translate LVDT measurements in thrust values.

During calibration, the operator applies the weights one at a time, keeping each for roughly five seconds to allow damping of the oscillations so that the thrust stand reaches an equilibrium position. Once the three weights have been applied the inverse procedure is followed, removing the three weights with five seconds intervals. This completes the calibration producing a pyramid shape, illustrated in Figure 5.12.

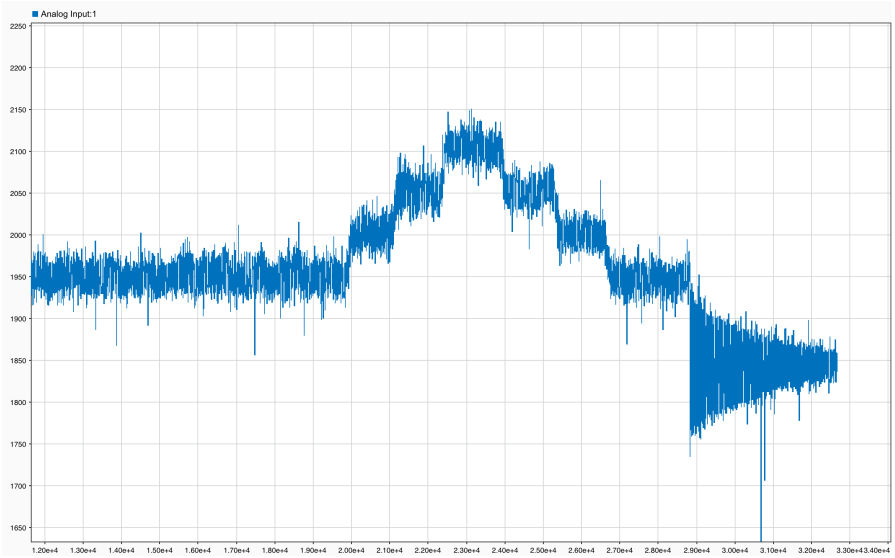

Figure 5.12: Example of calibration steps

The base plateau corresponds to an unloaded configuration, in which no weight is applied and only the thrust is exerted on the stand, whereas the top plateau represents the situation in which the three masses are unloaded and the stand is now subject to the three weights plus thrust. Once the masses are removed, the thruster is switched off so the resulting negative displacement is proportional to the thrust and can be computed.

The three masses produce a force of:

1. $F_1 = 13.35mN$
2. $F_2 = 26.77mN$
3. $F_3 = 40.19mN$

Errors in such calibration method can arise as a result of thermal drift and a lack of precision by the operator in setting the weights. Whereas the latter is self-explanatory, the former is due to the high temperatures reached during thruster operation, the metallic parts of the stand are subject to thermal expansion, resulting in incorrect measures of displacement by the LVDT.

Another minor error derives from the fact that, as the thruster anode is switched off to measure the thrust, the gas is still flowing, accounting for a minimal force, this is estimated to account for less than 3% of the thrust [54].

5.2.4 Arduino and simulink for data acquisition

The LVDT returns a voltage proportional to the displacement, in order to effectively acquire such output an analog to digital converter was used, more precisely an Arduino DUE board.

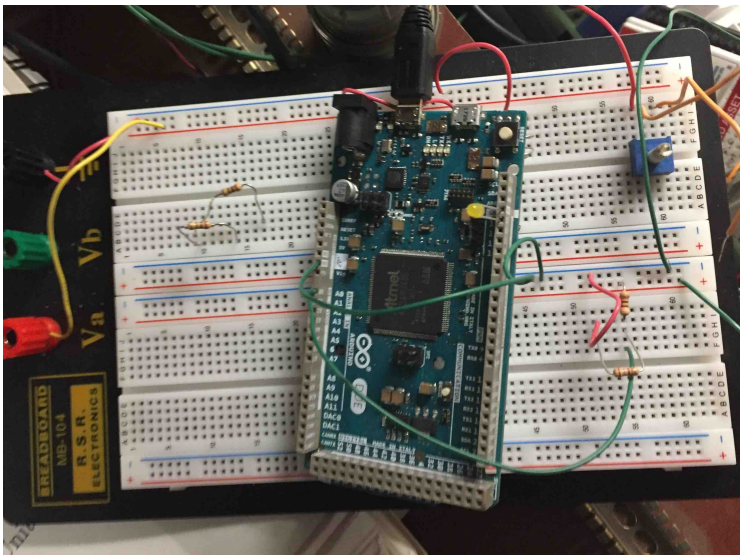

Figure 5.13: Arduino DUE board and voltage divider

A voltage divider was used in order to step down the voltage from the 0-5V scale of the LVDT to the 0-3.3V scale of the Arduino board. The digital signal in output of the Arduino is then acquired by Simulink, the results are saved in a timeseries format and then passed to MATLAB for data processing.

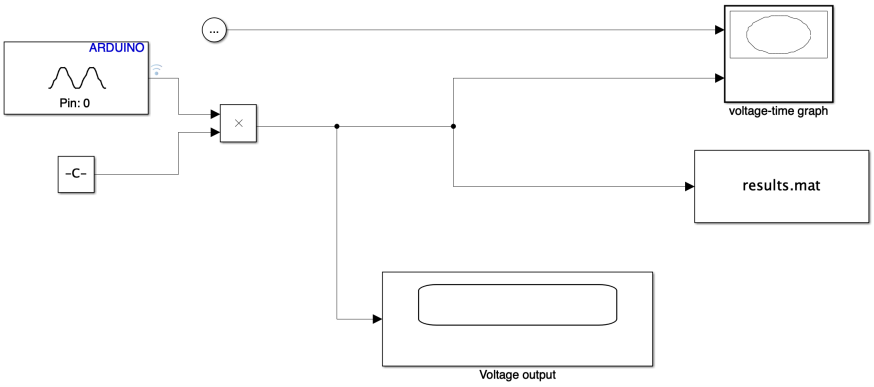

Figure 5.14: Schematic of Simulink acquisition program

5.3 Data processing

5.3.1 Raw data filtering

As evident from the raw data in Figure 5.12, the superimposition of thrust stand oscillation and line noises makes the detection of the plateaus for calibration and thrust computation an arduous task. The data must therefore be filtered before a force versus displacement curve can be computed, such is accomplished through a dedicated MATLAB algorithm.

The filtering process that allows to pass from noisy raw data to uniquely identified plateaus is divided into three stages. The implementation of a series of filtering steps, each tar-

geting different frequency bands allows for greater precision in oscillation reduction while maintaining the desired trend in data. In fact, the frequency of oscillations in the data depends on a vast amount of factors such as line noise, thruster weight, operator precision in applying weights and many others. Each of these factors influence the data at different frequencies and must therefore be filtered separately.

First filtering stage

In the first filtering step, a low pass filter (LPF) is employed to cut high frequency oscillations. A LPF allows only frequencies under a certain threshold, defined as the *cutoff frequency* (f_c) to pass, this factors out all the high frequency oscillations, typically resulting from line noise.

In order to generate such LPF, a second order Butterworth filter design is employed. These filters are defined as *maximally flat filters* as they present flattest possible frequency response possible without inducing peaking in the Bode plot [56].

These filters however, are characterised by a non-constant phase lag and is emphasized at lower frequencies. To account for such delay that varies with frequency, MATLAB's *filtfilt* filter was applied to guarantee a zero-phase digital filtering. This allows to reduce the startup delay as input data is processed in both the forward and reverse directions. That is to say that after filtering the data in the forward direction, this function repeats the same process in reverse, running it back through the filter .

In order to reduce all high frequency oscillations, a normalized cutoff frequency is chosen with a half-bandwidth equivalent to one standard deviation of the raw data. That is to say that the filter attenuates all data points laying more than one standard deviation from the mean of the raw data input.

The effects of such filter are demonstrated in Figure 5.15. As evident in the green line, high frequency fluctuations are strongly attenuated and the data does not present a starting lag. Trends in the data are still evident, with lower frequency fluctuations that have not been reduced by this first filter.

Second filter stage

The second filtering step must account for lower frequency oscillations in the data, these are evident when analysing the results of the first filtering step in Figure 5.15. Such lower frequency fluctuations in voltage output occur as a result of thruster oscillation as the thrust stand acts as a pendulum.

In order to target such lower frequency oscillations as the second stage filter consists in an average of a certain number of consecutive values. As stated, this helps to flatten the voltage output, as well as reducing the number of data points to handle. This last results is fundamental to reduce computational costs and to ease the third filtering step.

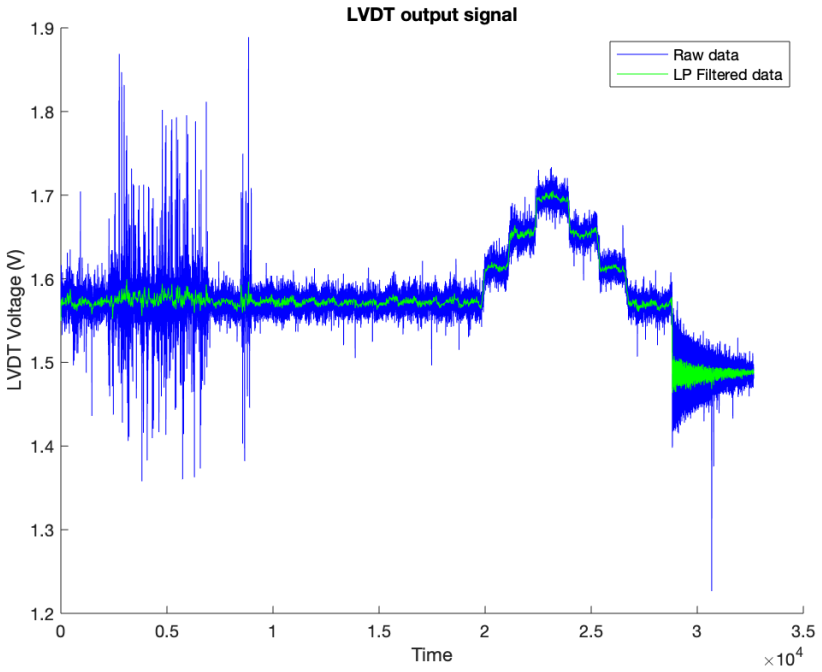

Figure 5.15: First filtering step using Low Pass filter

The algorithm therefore reads and averages a certain subset of the already filtered dataset. The dimension of this subset depends on the dimension of the whole dataset and has been chosen to be equal to half the square root of the total number of datapoints. The dimension of such subset, must be chosen correctly to be big enough to contain and average the fluctuations yet small enough to maintain the shape of the calibration curve.

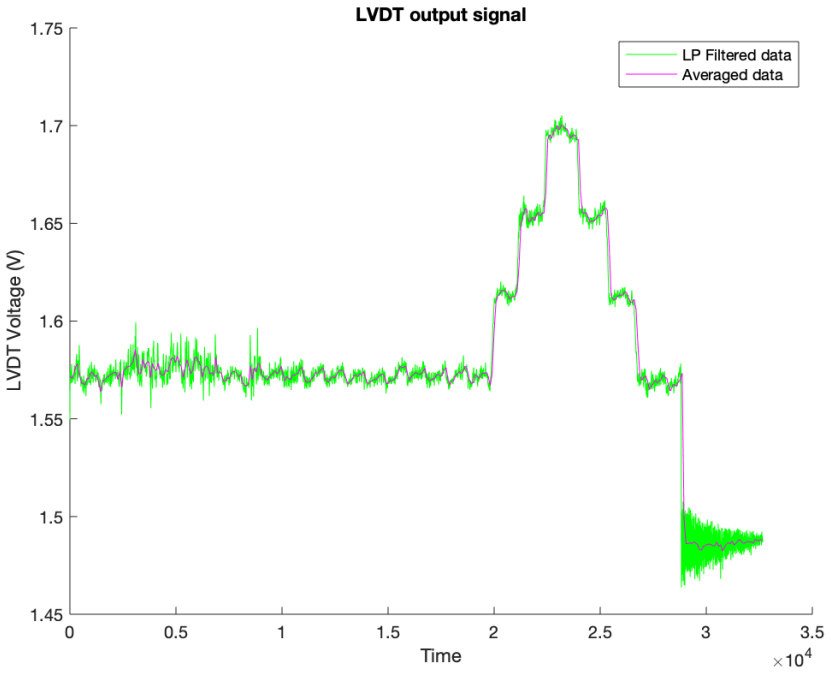

Figure 5.16: Second filtering step

Figure 5.16 demonstrated how this filtering step further reduces fluctuations and achieves a slightly flatter curve, represented by the magenta line. The importance of this step is to reduce the number of points, therefore the distance between each consecutive point, this makes the third step more effective as shall be demonstrated.

Third filter stage

The final filtering stage consists in obtaining constant voltage values for each load configuration, thus uniquely identifying the plateaus. The function created to do so evaluates the difference between two consecutive values, if such difference is lower than a threshold imposed by parameter C, the value is averaged with the previous ones. If however, the difference results greater, the value is saved.

For this reason, it was fundamental that the distance between each point was increased, as to emphasize the voltage difference and better distinguish the variations as a result of weights applied in calibration and those as a result of oscillations and line noise.

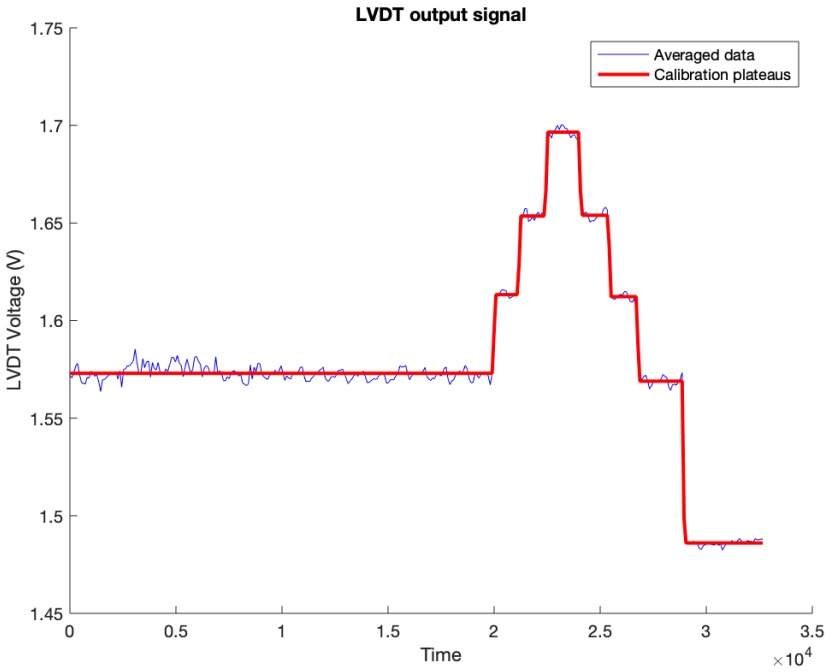

Figure 5.17: Third filtering step to identify the plateaus

This final filtering stage is regulated by the parameter C, this identifies a useful increase in values. That is to say that if the increase is smaller than C, it is considered a noise fluctuation, if it is greater, it is considered an increase as a result of an applied weight. Evidently, the threshold value must be set greater than the remaining fluctuations yet smaller than the variation in signal as a result of the applied loads.

The choice of parameter C greatly influences the identification and final values of the plateaus thus as a result affects the computed thrust. It is evident therefore that such

parameter must be carefully determined and optimized. Such task is achieved through an iteration of such parameter, the algorithm varies C from 10 times the standard deviation of the previous averaged data, to 0.1 times the standard deviation. The values of the resulting plateaus for each iteration are then compared to the value of the previously averaged data and the mean of the difference is recorded. If the shape obtained is not the pyramid expected, the iteration is discarded.

After having tried all the values of parameter C, only the one that yield the smallest difference is saved along with the corresponding calibration curve. This implies a minimum averaging error so that displacement values obtained during calibration are the most precise possible independently of the shape of the initial raw data.

The combined result is illustrated in Figure 5.18, in which the plateaus are now clearly visible. This filtering technique ignores the effects of thermal drift, such rising trend is visible in Figure 5.17 as the thruster is switched off, therefore computing more conservative values of thrust.

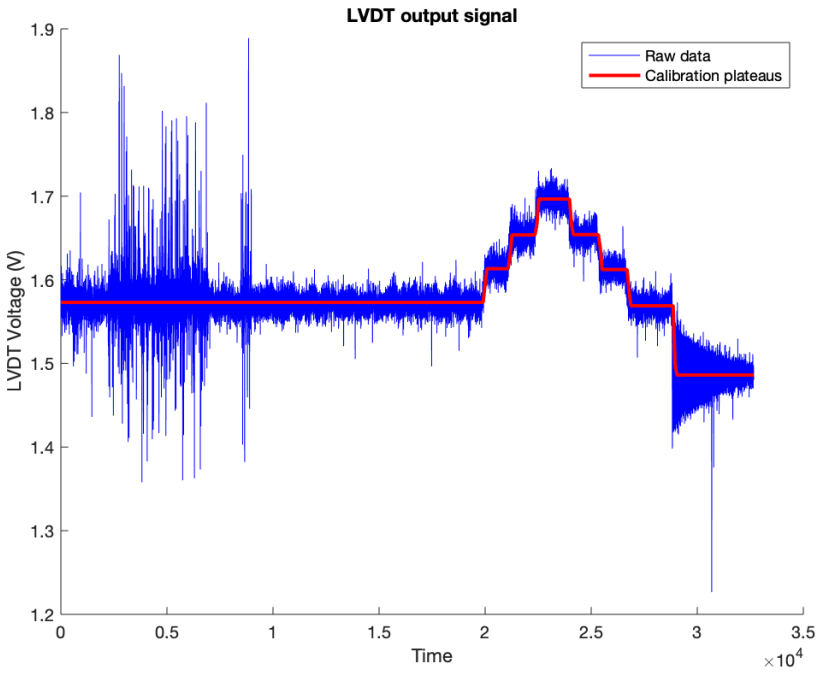

Figure 5.18: Complete filtering process

The filtering algorithm has been devised to work on all types of input data, with varying sample size, as long as the pyramid-like shape is maintained by the operator during calibration. Figure 5.19 illustrates the identical filtering procedure on another dataset, in which the acquired data presented a very different shape and size. The optimization algorithm guarantees that the parameters chosen minimize the averaging error.

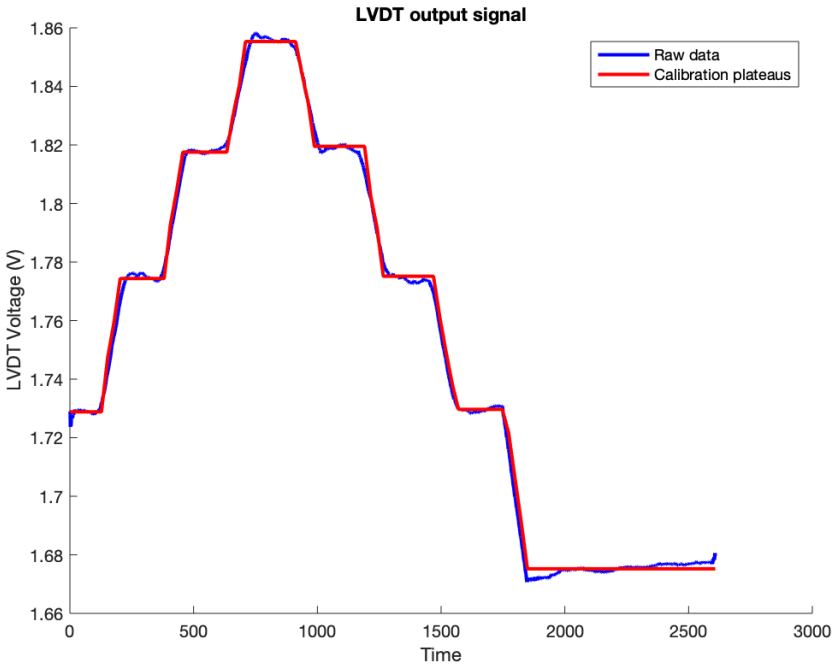

Figure 5.19: Filtering algorithm applied to different dataset

5.3.2 Thrust computation

Following the filtering steps, the algorithm recognizes the different calibration plateaus. This is achieved by determining the eight most occurring voltage values through a simple histogram count illustrated in Figure 5.20. However, as stated earlier, thermal drift influences the results. As evident from both the voltage output graphs and the histogram count, as a result of thermal drift two plateaus associated with the same weight applied, are characterized by slightly different voltage values.

To account for this difference, these two different values are averaged, in this way each load configuration is identified by a unique voltage. Having associated each load configuration to a unique displacement, a force versus displacement best fit curve can be plotted, as visible in Figure 5.21. As a result thrust can be extrapolated, extending the best fit line to the value identified by the lowest displacement plateau, associated to the switched off thruster.

By doing so, thrust results negative, this is because the actual force applied is the weight of the calibration masses plus the thrust, therefore the displacement of the base plateau, which is identified as the displacement resulting from no force applied, is actually characterized by the thrust. This assumption can be made as force and displacement are linear in a thrust stand.

Errors deriving from the generation of the best fit line can be estimated. The maximum error is computed considering the greatest distance between the calibration points and the best fit line.

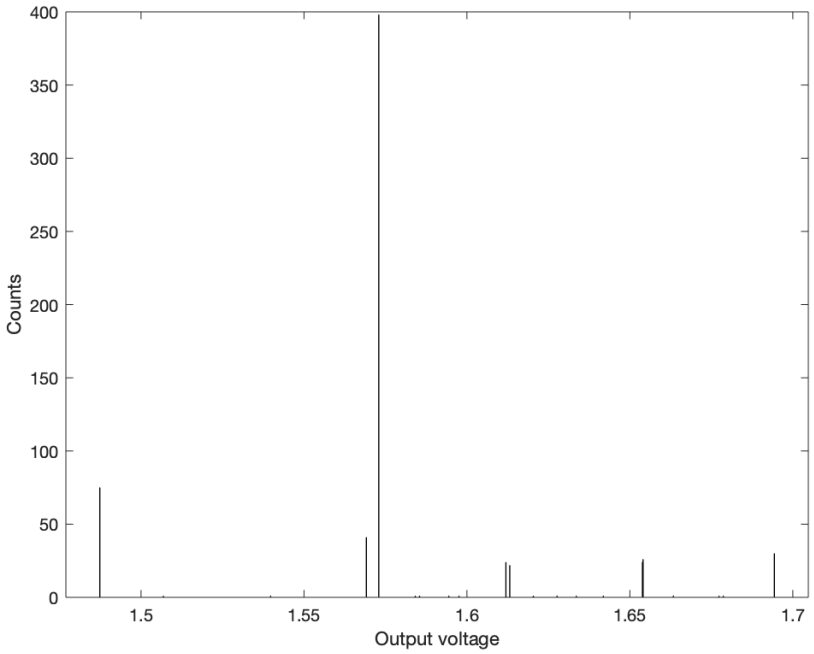

Figure 5.20: Histogram count to identify plateaus

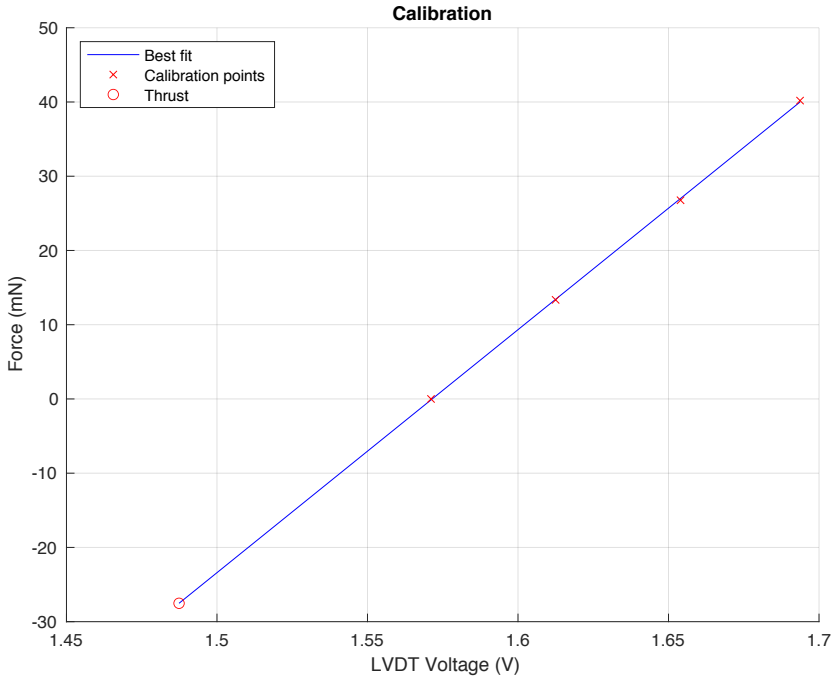

Figure 5.21: Force to displacement curve

5.3.3 Performance evaluation model

Once thrust is directly measured, numerous other parameters can be calculated to evaluate the performance of the thruster. Knowing the operating conditions it is immediate to determine the total power (P_{tot}) supplied to the thruster as a sum on the anode, keeper,

heater and magnets power supply.

$$P_{tot} = P_a + P_h + P_k + P_m = V_d I_d + V_h I_h + V_k I_k + V_m I_m \tag{5.2}$$

Space grade cathodes typically operate in self heating mode, in which the heater power can be excluded from the efficiency as the cathode can maintain the plasma discharge without the need of a dedicated power supply. This unfortunately was not the case for the cathode used in these experiments.

Having determined the total power, anode efficiency can be computed as:

$$\eta_a = \frac{P_A}{P_{tot}} \tag{5.3}$$

Moreover the effective exhaust velocity is obtained dividing the thrust by the anode mass flow rate (converted from sccm to kg/s):

$$c = \frac{T}{\dot{m}_a} \tag{5.4}$$

It is fundamental to highlight that such value is the average exhaust velocity as the plume, especially for molecular propellant, consists of ions with a wide range of velocities. The effective exhaust velocity is also directly related to the specific impulse:

$$I_{SP} = \frac{c}{g_0} \tag{5.5}$$

In which g_0 is the reference value of gravitational acceleration at sea level taken to be 9.807m/s^2. Finally the kinetic power can be computed:

$$P_T = \frac{1}{2} T c \tag{5.6}$$

From which the global efficiency of the thruster is derived:

$$\eta_G = \frac{P_T}{P_{tot}} = \frac{T^2}{2\dot{m}_p P_{tot}} \tag{5.7}$$

Long Channel Thruster Results

6.1 Performance measurement

6.1.1 Thruster operation

Following the procedure listed in the previous chapter, the thruster was ignited and a stable plasma discharge was generated, pictures of which are shown in Figure 6.1. This achievement demonstrated the effectiveness of the design modifications, as a stable plasma discharge was maintained on 100% nitrogen with no xenon present to enhance ionization.

Figure 6.1: N_2 Hall thruster with 100% nitrogen plasma discharge

To conduct these first tests, pure nitrogen was chosen over a more complete air mixture mainly to avoid oxygen contamination, which would result in rapid deterioration of the barium oxide impregnated cathode available for testing. For future testing with a complete air mixtures, a different non-reactive cathode technology is suggested.

Running on pure nitrogen as opposed to an air mixture does not greatly affect the accuracy of the results. In fact, not only does nitrogen constitute more than 78% of the atmosphere, the ionization cross sections and first ionization energies of O_2 and N_2 are similar [49].

Initial testing was conducted at low anode potential with 99 sccm (2.06mg/s) pure nitrogen flow. Whereas the volume flow rate was much higher, the mass flow rate is substantially similar to xenon operation on the Z-70 illustrated in previous chapters to aid comparison between the two thrusters and propellants. The results are presented in Table 6.1.

Discharge Potential (V)	Discharge Current (A)	Magnet Current (A)	Anode MFR (mg/s)	Cathode MFR (mg/s)	Anode Efficiency	Chamber Base Pressures (Torr)
180	3.2	0.8	2.06	0.29	0.88	2.0×10^{-4}
180	2.6	1.6	2.06	0.29	0.85	2.2×10^{-4}
180	2.9	1.7	2.06	0.29	0.88	2.0×10^{-4}
180	3.2	1.7	2.06	0.29	0.88	2.1×10^{-4}
180	3.0	2.0	2.06	0.29	0.88	2.0×10^{-4}
180	1.5	2.5	2.06	0.74	0.74	8.1×10^{-5}
200	3.9	1.6	2.06	0.33	0.91	1.2×10^{-4}
200	3.5	1.6	2.06	0.33	0.90	1.1×10^{-4}
200	2.7	2.0	2.06	0.29	0.86	1.0×10^{-4}
200	3.3	2.3	2.06	0.15	0.88	1.0×10^{-4}
200	2.7	2.6	2.06	0.29	0.85	1.3×10^{-4}
200	2.1	3	2.06	0.65	0.81	8.5×10^{-5}
220	3.5	2.2	2.06	0.34	0.89	1.3×10^{-4}

Table 6.1: N_2 thruster operating conditions

Possibly due to cathode degradation, the thruster discharge was at times unstable and minimum parameter modifications could cause it to instantly quench or rapidly change mode. This phenomenon became particularly evident when increasing the electromagnet current or the applied discharge potential. In fact, as more efficient electron confinement or increased electron energies boosted ionization and the density of ions increased, it became evident that the degraded cathode emitter struggled to supply the required electron current. Keeper voltages were observed to rise abruptly to counter this effect, ultimately quenching the cathode discharge when voltages above 30-40V were reached. In order sustain the hesitant cathode discharge, cathode mass flow rate had to be increased to enhance plasma density within the cathode.

As evident from the results in Table 6.1, operating the long channel thruster design on nitrogen constitutes higher currents than those observed with typical xenon-operating shorter channel thrusters, even at lower anode potentials. These results suggest that air-breathing thrusters are expected to operate at high power levels, this aspect must be taken into account when choosing the cathode, as high currents can constitute an additional source of deterioration.

Higher currents occur mainly as a result of the higher volume flow rates during operation, essential to maintain a plasma discharge. The lower atomic mass of nitrogen compared to xenon implies that when running on similar mass flow rates to xenon thrusters (2mg/s), a significantly higher number of nitrogen molecules are present, therefore a greater number of electron and ion charges are produced at comparable ionization levels.

Another reason for the high currents faced during operation was the reduction in electron confinement as a result of higher chamber pressures faced and weaker peak magnetic field generated by the shorter coils, both these factors lead to an increase in electron mobility

towards the anode. These aspects therefore must be evaluated and corrected for future testing.

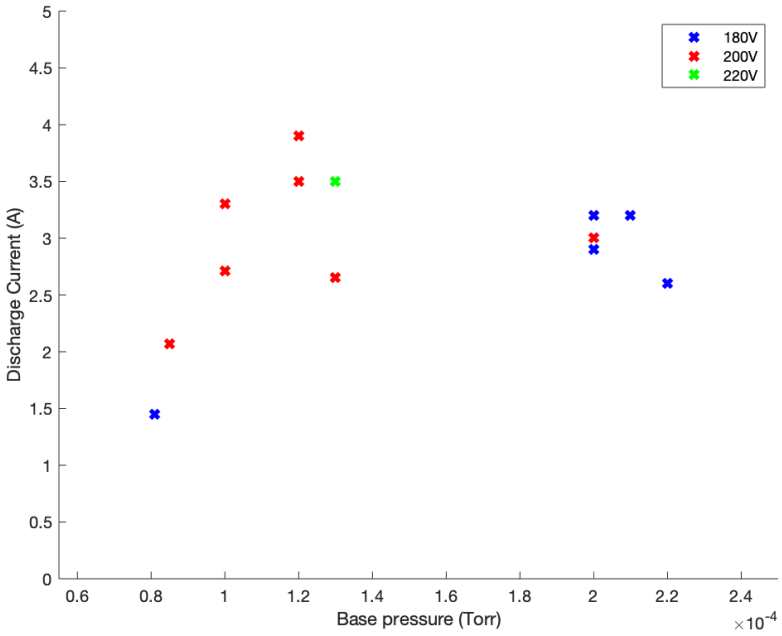

Figure 6.2: Effects of base pressure on discharge current

The effect of background pressure on discharge current is evident from Figure 6.2. The figure clearly illustrates the combined effect of base pressure and magnetic field on discharge current, as anode current drops to a value of 1.5A, almost half of all other values, at the lowest pressures and highest magnetic fields.

An increase in magnetic field density counters the aforementioned electron drift towards the anode, forcing electrons in an azimuthal motion around the chamber, thus limiting anode current. Such a result is evident in Table 6.1 and better illustrated in Figure 6.3.

The figure denotes the benefits of a increase in magnetic field density on anode currents. This decreasing trend is a consequence of more efficient electron confinement, especially significant when such high chamber pressures were registered.

Figure 6.3 also suggests higher anode currents for higher applied potentials. In fact, higher potentials cause the electrons to accelerate to greater velocities, thus energies. As previously described, at higher electron energies are associated greater probabilities of ionization, thus greater ionization rates, illustrated in Figure 3.1. This result is better appreciated in the discharge characterization curve illustrated in Figure 6.4.

As potential increases so does the electron energy, boosting ionization. As mentioned, testing at greater potentials was hindered as a result of cathode degradation. Typical characterization curves are expected to flatten out as potential increases, thus when all neutrals are ionized a current maximum is reached. It is interesting to notice how the

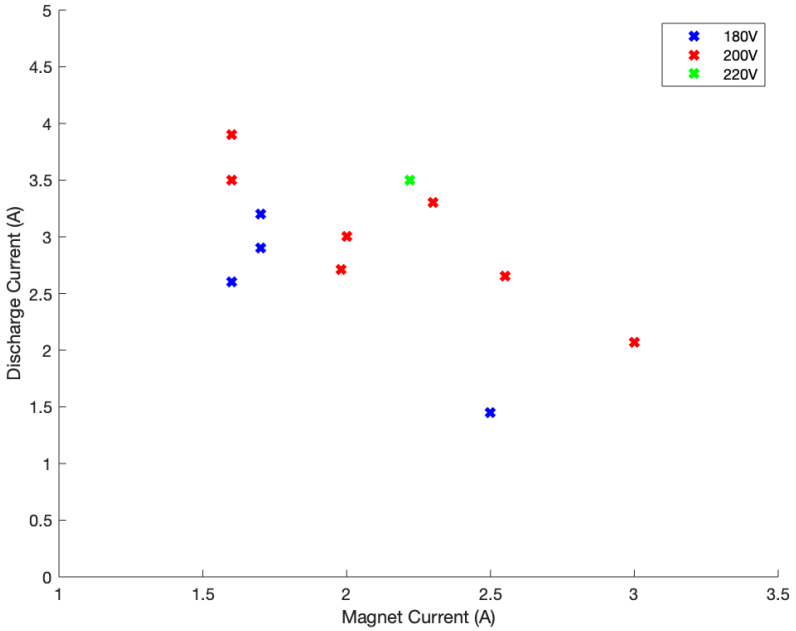

Figure 6.3: Discharge current as a function of magnetic field with varying anode potentials

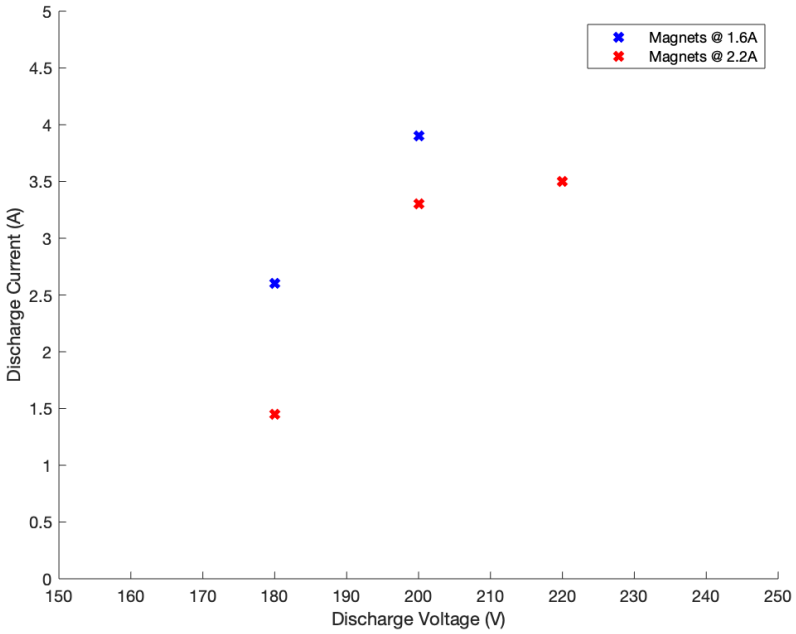

Figure 6.4: Discharge current as a function of discharge potential at constant magnet currents

curve seems to flatten at higher potentials than in typical xenon thrusters, this is believed to be a consequence of the higher first ionization energy of nitrogen neutrals.

Molecular propellants however, require more in depth studies of discharge currents at greater potentials. In fact, at growing potentials, dissociative ionization reactions of nitrogen neutrals are expected, which would cause a surge in current and less efficient operation.

As potential increases, the composition of the plume is expected to shift towards a greater presence of atomic nitrogen and its ions.

Further increasing of potential would lead to the complete dissociation and ionization of the nitrogen neutrals, effectively flattening out the characterization curve. Such extreme condition would be characterized by very high powers and high propulsive performance as the number of charges would effectively double, yet low efficiencies as a result of the surge in power.

6.1.2 Performance with varying parameters

To measure the propulsive performance of the long channel N_2 optimized thruster, this was placed on the thrust stand in the large vacuum chamber and operated with a pure nitrogen inflow to the anode and argon to the cathode. To better characterize the thruster, performance was measured varying parameters of the thruster.

Due to thruster instability during calibration, performance was not measured in all of the aforementioned operational points. Moreover, the thruster tended to rapidly change operating modes, reflected in an asymmetric calibration pyramids, for this reason thrust calculation was slightly modified from the initial procedure to account for the multiple modes observed. This aspect introduces some uncertainty in the thrust measured, as highlighted by the errors, and shall be better explained in the following section.

The results presented in Table 6.2 reflect the benefits of the chamber extension, a plasma discharge was initiated and maintained running on pure nitrogen and good levels of thrust obtained, even at such low anode potentials.

Run	Anode Voltage (V)	Anode Current (A)	Magnet Current (A)	Thrust (mN)	Isp (s)	Global Efficiency
Run 1*	180	3.2	1.7	22.62 ± 1.24	1107.31 ± 60.72	0.16
Run 2	180	3.0	2.0	22.76 ± 0.66	1114.16 ± 32.31	0.17
Run 3*	180	1.5	2.5	23.41 ± 0.63	1145.98 ± 30.84	0.28
Run 4	200	3.5	1.6	22.79 ± 1.19	1115.63 ± 58.25	0.14
Run 5	200	2.7	2.0	20.85 ± 1.20	1020.66 ± 58.74	0.15
Run 6	200	2.7	2.6	22.32 ± 0.02	1092.62 ± 0.98	0.17
Run 7*	220	3.5	2.2	20.62 ± 2.66	1009.41 ± 130.21	0.10

Table 6.2: N_2 thruster performance results, * indicates strong instability during calibration

The results indicate good performance of the thruster, with thrust levels in the 20-23mN range. The specific impulse and efficiencies however, indicate poor performance relative to reference xenon-operating electrostatic thrusters, ranging respectively around 1100s and 16%. This is a direct consequence of the high mass flow rates required and high currents obtained.

As observed by Table 6.2, increasing the magnetic field density generally results in better performance of the thruster. As previously discussed, increasing the magnetic field density results in a reduction of electron mobility which extends the effective ionization region thus increasing the probability of collisions with neutrals. As more ions are being created, the mass flow rate of propellant leaving the thruster ($\dot{m}_i$) increases, which leads to the observed increase in thrust, better appreciated in Figure 6.5.

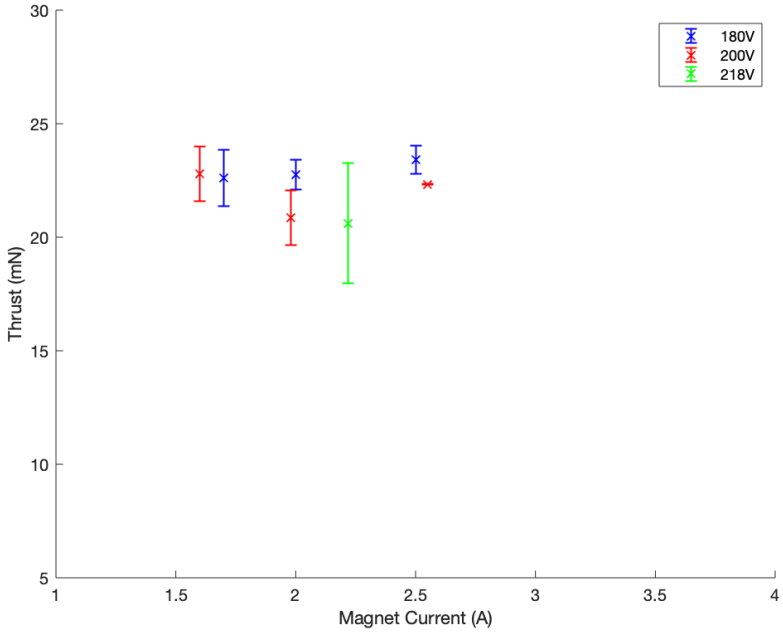

Figure 6.5: Thrust variations with magnetic field, at varying anode potentials

The obtained thrust values are lower than typical xenon operating Hall thrusters at similar discharge powers, as an inevitable consequence of the reduced ionization and losses for dissociation. However, a net improvement from the Z-70 runs operating on molecular propellants illustrated in previous chapters is evident, not only as the discharge is maintained singularly on nitrogen but also as the thrust levels and efficiencies double.

As a result of the high mass flow rates, specific impulse values are low for electric thrusters, ranging round 1100s. As expected however, a rising trend is observed with an increase in magnetic field, indicating a more efficient use of propellant, better appreciated in Figure 6.6

The reduction in electron mobility generates a visible drop in anode current as electrons are forced in an azimuthal drift and axial diffusion towards the anode is reduced. This decrease in discharge power and increase in thrust as magnetic current is increased is reflected in an increase in global efficiency of the thruster, as highlighted in Figures 6.7 and 6.8.

The low efficiencies faced reflect the poor ionization of nitrogen molecules and the inevitable losses for dissociation and greater wall collisions. However, the modifications to

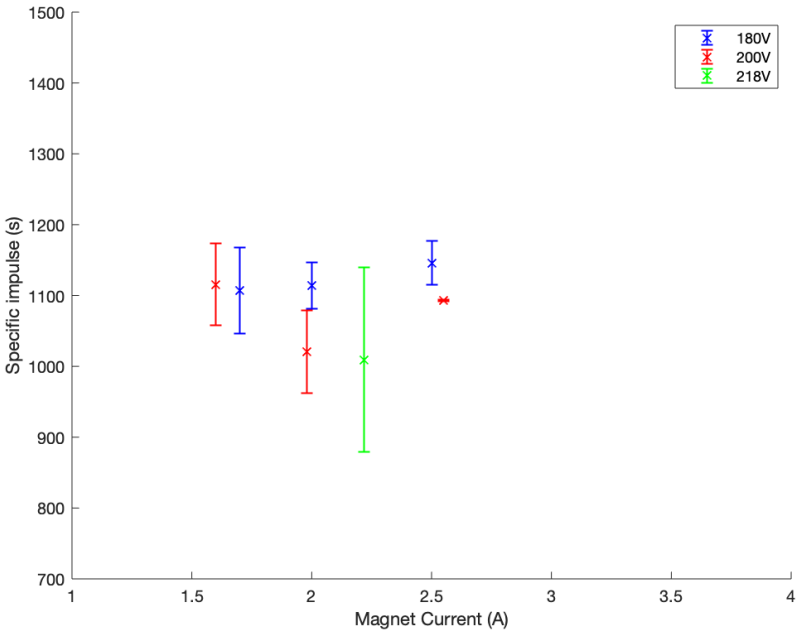

Figure 6.6: Specific impulse variations with magnetic field, at varying anode potentials

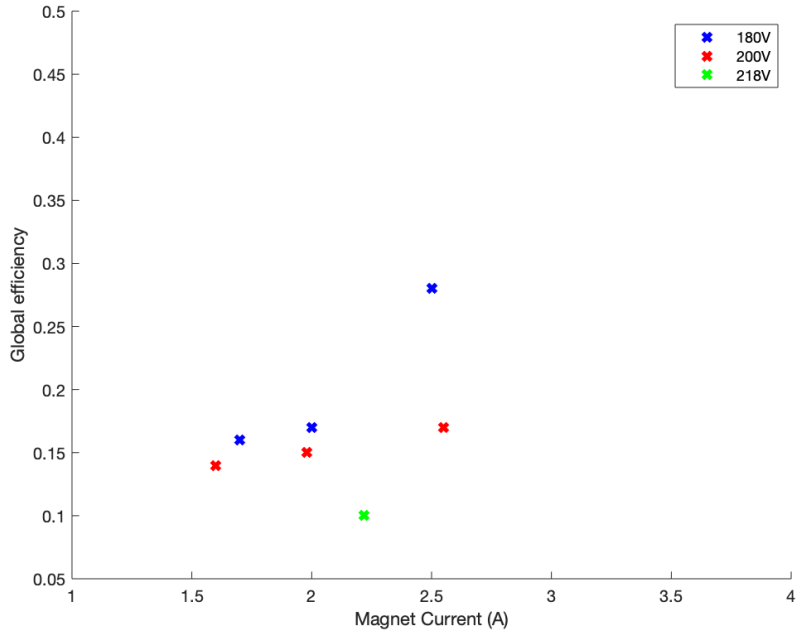

Figure 6.7: Global efficiency variations with magnetic field, at varying anode potentials

the ionization channel aimed at extending the ionization region and increasing neutral residence time visibly improved performance of the thruster, with efficiencies averaging around 15% up to a peak of 28%. This longer channel however, can result in an increase in wall losses, hindering a further increase in efficiency.

A particularly good point is observed in Run 3, with anode currents dropping to 1.5A and efficiency doubling to 28% as a result of an increase in magnetic field. This test was

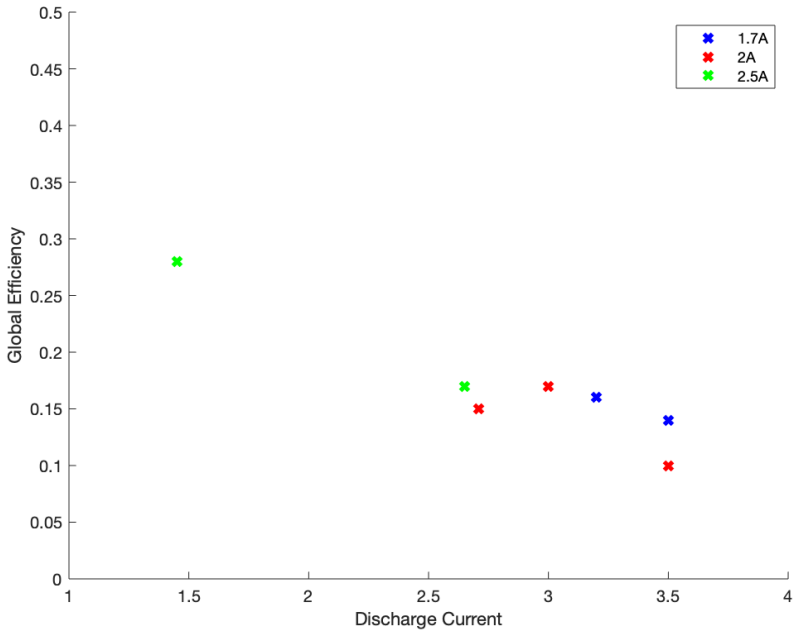

Figure 6.8: Global efficiency as function of anode currents, at varying magnet currents

also characterized by the lowest background pressure registered during all testing, thus electron confinement was particularly enhanced. However, the calibration was affected by very strong instabilities that could have affected the positive outcome of the experiment. Further testing is therefore required to verify the performance at such low power mode. The rising trend in performance with magnetic field coupled to the low anode current however, are encouraging symptoms of efficient thruster operation.

This encouraging trend noticed when increasing magnet currents indicates the importance of an extended ionization region and effective electron confinement to boost nitrogen ionization, especially important when high background pressures are experienced in the vacuum chamber as was the case during these experiments. This indicates that the 130G magnetic field that the electromagnets generate is still inadequate for efficient operation, therefore stronger magnetic fields are necessary for future developments, at least up to 200G, to observe if these encouraging trends continue.

An increase in mass flow rate is expected to results in more efficient operation of the thruster, with optimal values simulated around 2.5mg/s [35]. As aforementioned, this increase would lead to greater plasma densities and ion mass flow rates, which should reflect in greater thrust measurements. However, variation in mass flow rate was hindered by the difficulty in sustaining a stable discharge and limited range achievable by the N_2 mass flow controller available. With lower nitrogen mass flow rates, especially under 80sccm (1.6mg/s), the plasma discharge resulted unstable and easily quenched at increasing magnet current.

Higher mass flow rates were not achievable as the controller was limited to a maximum volume flow of 100 sccm (standard centimeters cubed per minute), which corrisponds to

2.06 mg/s of nitrogen used during testing. Moreover, further increases in mass flow rate were also avoided in order to prevent surges in anode current during ignition that would damage the cathode.

The results seem to indicate an unexpected decrease in performance associated with higher anode potentials. This trend could be linked to an increase in dissociative reactions, leading to less efficient thruster operation. In fact, as potential is increased, the electrons would acquire higher energies, which in turn could lead to more probably dissociative ionizing reactions, especially energies surpass the 25eV threshold. This observation seems to be contradictory to the positive trend observed from an increase in magnetic field, which is also expected to cause an increase in electron energy. Further testing is required to verify observed phenomena.

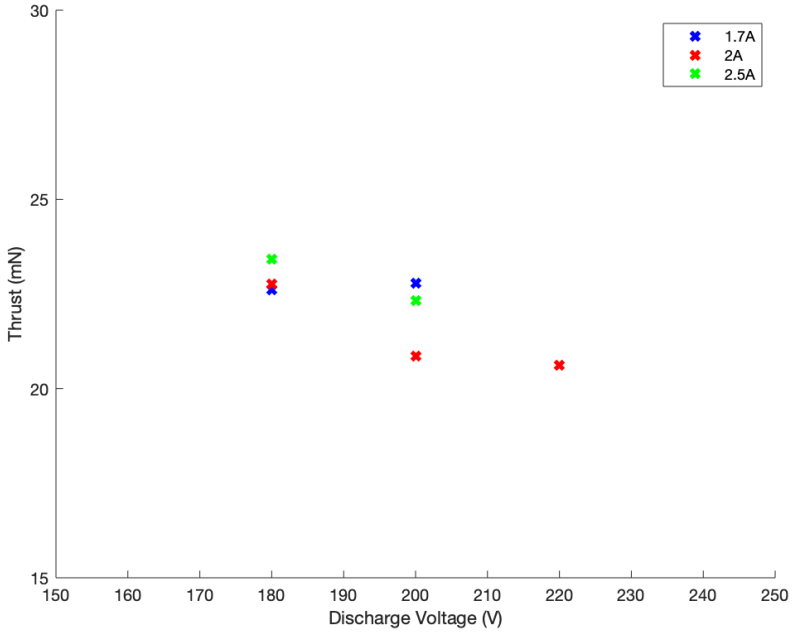

Figure 6.9: Thrust variations with applied potential

As in Figure 6.9, a decreasing trend is observed at increasing potentials, with exception of the case with lowest magnetic fields. In fact, higher magnetic fields and higher potentials can be associated with an increase in electron energy which may introduce dissociative reactions. This is further emphasized by noting how this decreasing trend is not evident with lower magnetic fields, which may be a result of lower electron energies.

Further testing and modelling is required to better comprehend the electron energy and the reasons for such trends at varying applied potential. It is fundamental to understand if the electron energy is too high, thus increasing the potential enhances dissociative ionization reactions, or if its too low, then increasing the magnetic field causes it to increase and thus enhance ionization and the effects observed at varying potential are due to other phenomena.

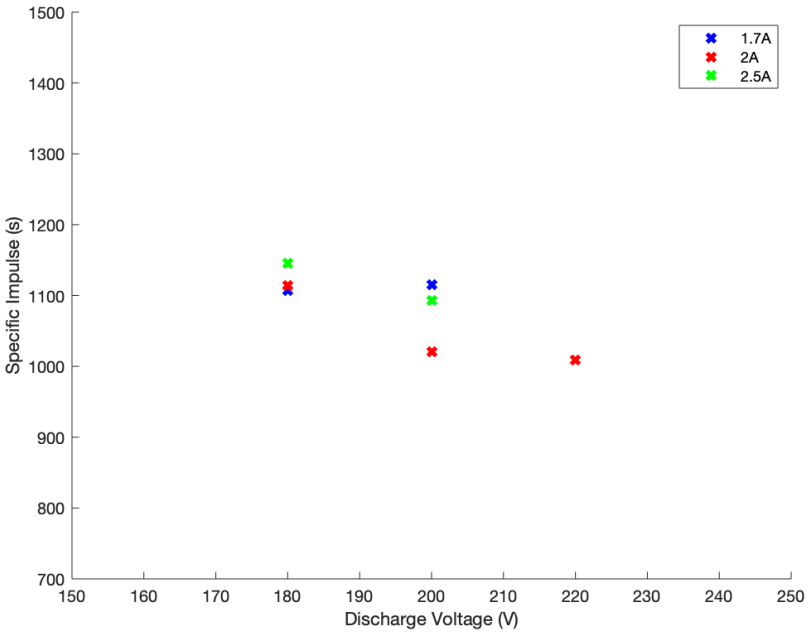

Figure 6.10: Thrust variations with applied potential

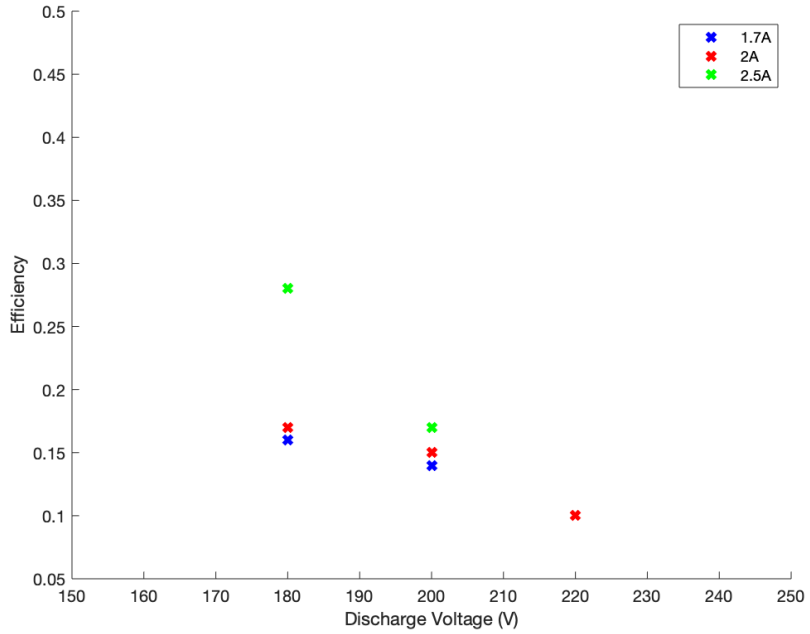

Figure 6.11: Thrust variations with applied potential

In fact, simulations conducted by Cha [35], model electron temperature to reach a maximum of 15eV in the ionization region, which is just enough to ionize nitrogen neutrals, but with low rates. The higher than expected background pressure and slightly weaker peak magnetic field may result in electron energies even lower than in simulation, although numerous other factors would influence the temperature distribution.

Spectrometrical analysis conducted on the thruster has given approximate electron tem-

peratures of 5-8eV at 1cm after the thruster exit plane, slightly lower than predicted by PIC simulations. Although highly approximate these results could suggest that indeed the energies are too low, therefore the benefits seen at increasing magnetic fields are a result of an increase in ionization rate. Unfortunately the complete results of these analyses are not yet available, yet further testing is needed to validate these results and provide more certain explanations, fundamental for future development of the thruster.

In any way, when operating on molecular propellants it is fundamental to control the electron energy in a desired range as to reduce the possibility of dissociative ionization reactions, occurring for nitrogen after a threshold energy of 25eV, yet to guarantee sufficient ionization, therefore energies above 15eV.

6.1.3 Instabilities and errors

Thruster instabilities during calibration was the main source of error and is reflected in a certain degree of uncertainty in the results obtained. It has been consistently noticed that during calibration the displacement value, reflected in LVDT voltage output, would vary even at fixed applied weights, this is a symptom of the thruster changing operation mode, thus varying the thrust exerted on the stand. As example of this is illustrated in Figure 6.12. This increase in displacement led to an asymmetric calibration pyramid, as displacement values on the left side identified by the code, where visibly different from those on the right.

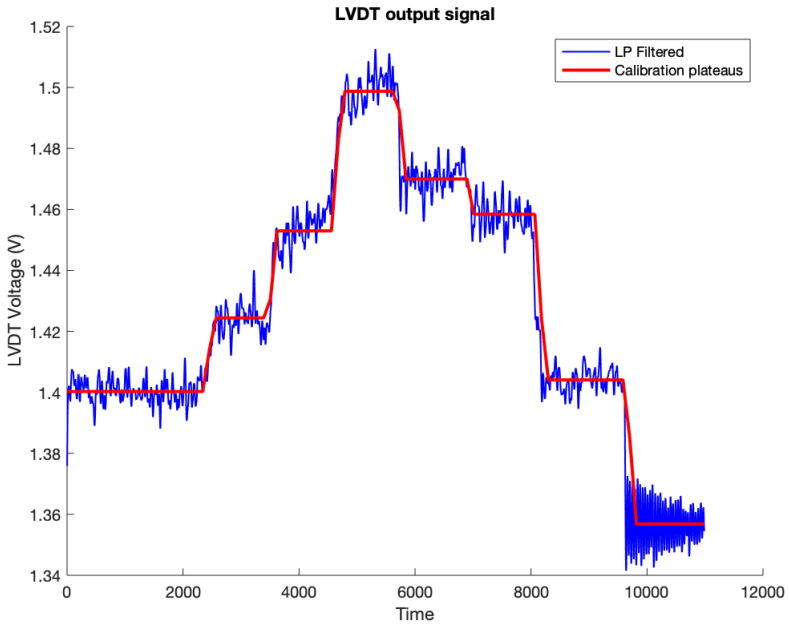

Figure 6.12: Thruster changing modes during thrust calibration

This anomaly has been consistently observed in most calibration shapes and is therefore believed to be triggered by the movement of the thrust stand as a result of the applied calibration weights. In fact, it may occur as a result of the oscillations of the cathode

relatively to the thruster, yet further investigation is required. A persistent error by the operator during calibration is unlikely, yet not excluded.

Further causes of the instability may be linked to cathode deterioration. As previously mentioned, it is believed that the emitter was degraded, thus plasma density in the cathode was low. The cathode would therefore struggled to give sufficient electron current, which would explain the observed fluctuations of the keeper voltages and sudden quenching if the cathode discharge during testing.

However, thruster instability is not the only explanation to these peculiar results. Such strong asymmetry between the two sides of the calibration curve may be linked to the heating of the thruster, which could affect both the LVDT and the global elastic constant of the thrust stand, making it change during calibration. This phenomenon has been previously observed in all thrust measurements with the Z-70, yet accounted for a minimum difference between the two sides. It is possible that this new thruster, albeit the lower powers involved, dissipates more power into heat, synonym of less efficient operation, achieving higher temperatures which affect the reading. Thermal models must be consulted in order to verify this hypothesis.

In order to account for such anomaly, the thrust calculation has been slightly modified. Instead of averaging the two plateaus relative to the same applied weight on both side of the calibration pyramid, the results presented in Table 6.2 have been obtained by considering only the displacement values on the left side of the pyramid, ignoring therefore the change in mode of the thruster that occurs later.

In order to verify the veracity of the presented results, the thrust calculations have been repeated, this time averging the two displacement plateaus for each applied weight, therefore obtaining averaged measurements between the two modes. These results are presented in Table 6.3 together with the previously commented ones for better comparison.

Run	Thrust (mN)	Isp (s)	Global Efficiency
	One side		
Run 2	22.76 ± 0.66	1114.16 ± 32.31	0.17
Run 4	22.79 ± 1.19	1115.63 ± 58.25	0.14
Run 5	20.85 ± 1.20	1020.66 ± 58.74	0.15
Run 6	22.32 ± 0.02	1092.62 ± 0.98	0.17
	Averaged		
Run 2	21.31 ± 2.88	1043.18 ± 140.98	0.15
Run 4	20.05 ± 2.68	981.50 ± 131.19	0.11
Run 5	17.29 ± 4.56	846.39 ± 223.22	0.10
Run 6	18.22 ± 3.82	891.91 ± 187.03	0.11

Table 6.3: Comparison of N_2 thruster performance results with different computation techniques

It is dutiful to highlight that this second technique hasn't been possible for all runs previously measured, as some where characterized by oscillations so big that it was impossible to identify a reasonable plateau. Moreover, as a result of the fluctuations, this second technique introduces greater error in thrust computation.

Albeit lower performance values the results show substantially similar trends, as illustrated in Figures 6.13, 6.14 and 6.15. This indicates the effectiveness of a strong magnetic field and low background pressure in order to guarantee optimal thruster performance.

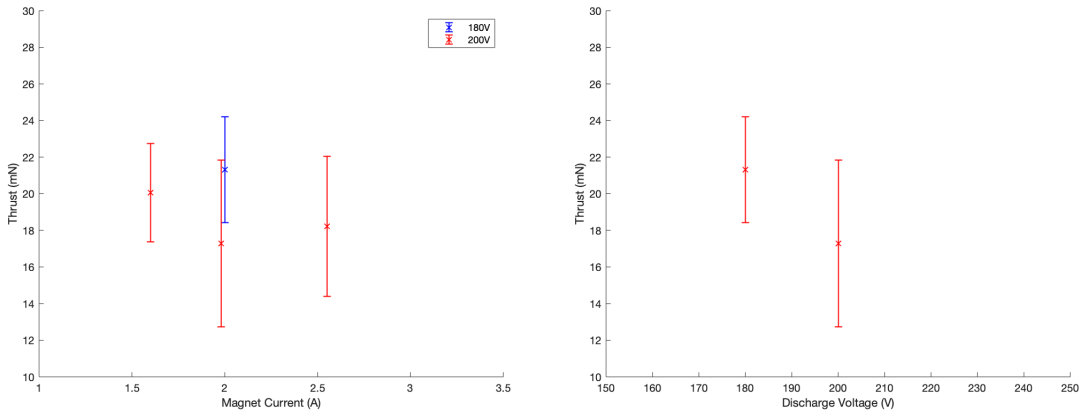

(a) Thrust as a function of magnet current (b) Thrust as a function of discharge potential

Figure 6.13: Thrust trends with averaged calibration curve

The decreasing trend with discharge potential is still visible, indicating the importance in modelling electron temperature and understanding the dynamics of the ionization and acceleration region as a function of potential.

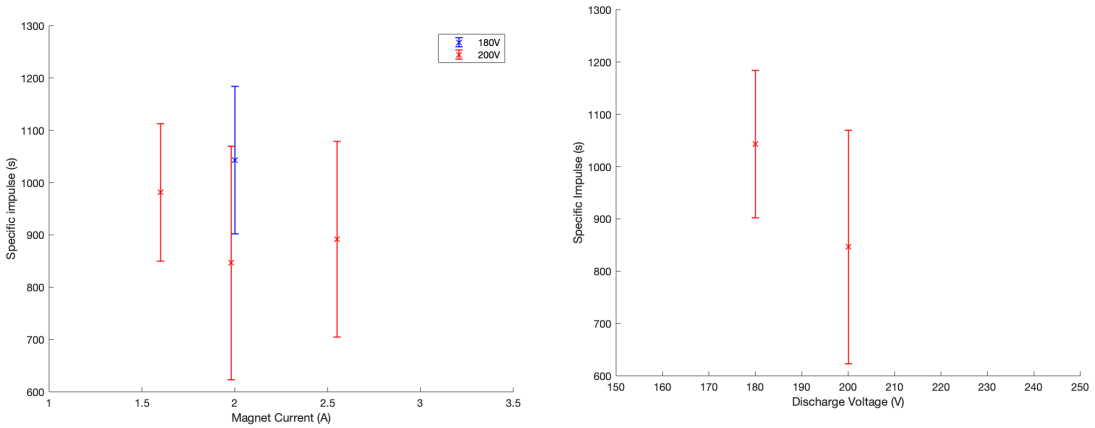

(a) I_{SP} as a function of magnet current (b) Specific impulse as a function of discharge potential

Figure 6.14: I_{SP} trends with averaged calibration curve

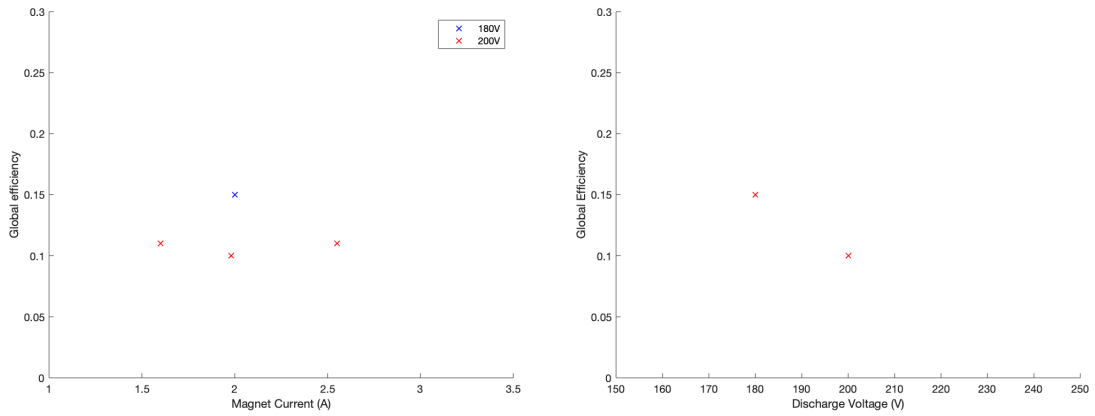

(a) Efficiency as a function of magnet current (b) Efficiency as a function of discharge potential

Figure 6.15: Global efficiency trends with averaged calibration curve

It is dutiful to highlight that, as the displacement values vary not throughout all of the calibration procedure but only in some plateaus and are minimal at the base value once all weights are removed, the code perceives this behaviour as a decrease in the elastic constant of the system, which would be the case if these are an effect of system heating, thus a lower thrust is obtained from calculations. However, if these anomalies are due to thruster instabilities, the increase in displacement would be associated to an increase in thrust, therefore the obtained thrust measurements illustrated in Table 6.2 are conservative as they ignore this increase on the second part of the calibration curve.

Another problem faced during testing was the high background pressure observed in the vacuum chamber during operation. The pumping system struggled to face the increased volume flows, as the chamber settled to base values in the ranges of 1×10^{-4} Torr during operation with a steady 2.06mg/s nitrogen flow. These base pressures are almost an order of magnitude higher than those observed during typical xenon operation. A regeneration of the cryopumps, consisted in heating the panels to make trapped particles evaporate, did not help improve the pumping system's efficiency.

As previously stated, this high background pressure hindered electron confinement and worsened thruster operation. It is therefore believed that operating at lower pressures will result in increased performance and efficiency yet further testing is required. This is emphasized by Figure 6.2, in which the lowest anode currents observed during testing where experienced at lower chamber pressures.

Variation in mass flow rate was hindered by the difficulty in sustaining a stable discharge and limited range achievable by the N_2 mass flow controller available. With lower nitrogen mass flow rates, especially under 80sccm (1.6mg/s), the plasma discharge resulted unstable and easily quenched if the potential was not raised sufficiently.

Higher mass flow rates were not achievable as the controller was limited to a maximum volume flow of 100 sccm, which corresponds to 2.06 mg/s of nitrogen used during testing.

Moreover, further increases in mass flow rate were also avoided in order to prevent surges in anode current during ignition that would damage the cathode.

Other than the instability of the thruster, the calibration technique is affected by some intrinsic sources of errors. It relies on the operator's precision to apply the test load, who's weight measurement is affected by some degree of error, to the thrust stand. Yet another source of error during calibration is linked to the fact that, for practicality, the mass flow rate is not switched off together with the thruster during the final step of calibration. This mass flow rate could provide an additional source of force to the stand, which was measured to be in the range of 3% for typical xenon thrusters [54], working with higher mass flow rates may introduce a greater errors. Further minor errors may be linked to thruster misalignment with respect to the thrust stand which may account for a smaller computed thrust and leakages o propellant in the feed lines, therefore the actual mass flow rate to the thruster might be slightly less than 2.06mg/s.

Conclusion and Future Works

7.1 Achieved results

7.1.1 Overview

The increases in performance observed were achieved thanks to design modifications aimed at enhancing nitrogen ionization. The principal problem in ionizing such molecular propellant resides in the higher first ionization energy and lighter mass, the former being self-explanatory whereas the latter signifies reduced residence times of the faster molecules in the chamber.

Previously tested shorter channel SPT designs proved inadequate in ionizing molecular propellants, as has been demonstrated in a simplified model (see Section 4.2.1) and the losses in performance presented in Table 3.4. This is a consequence of an ionization region ($L_i \approx 2mm$) shorter than the typical ionization mean free path of nitrogen molecules ($\lambda_I \approx 20 - 30mm$). This signifies that the average distance a nitrogen molecule has to travel before being ionized was longer than the distance in which electrons, responsible for the ionization, were trapped, making the probability of ionization extremely low, with mass utilization efficiencies in the range of $\eta_u \approx 6\%$

In order to improve such condition, the chamber was extended along with the peak magnetic field density region, in such way the area ionization region was enahnced to $L_i \approx 30mm$, improving ionization to reach ideal mass utilization efficiencies of $\eta_u \approx 64\%$. The ionization mean free path still represents 98% of the ionization length, therefore further extension is still necessary.

The obtained measurements show good improvement of performance of the long channel Hall thruster for operation with molecular propellants, when compared to previous air breathing electric propulsion experiments. As a result of the increased ionization region within the thruster, thrust levels have improved from 12mN on an air/xenon mixture to 22mN on a 100% nitrogen flow, with specific impulses and efficiencies following the same trend, respectively growing from 792s to 1110s and 6% to 16%.

An encouraging trend was observed as magnet current was raised, this increased magnetic field density, enhancing electron confinement. It is therefore suggested to further

strengthen the magnetic field, now capable of reaching a maximum of 130G peak, of at least up to 200G to observe if these encouraging trends continue. Coupled with the increased magnetic field, the thruster has been observed to work best when the background chamber pressures were low, emphasizing the positive effects of reduced electron mobility on efficiency improvement.

As previously mentioned these performance values are uncorrected for atmospheric flight (see Section 2.3.2) and with much slower propellant inflow speeds than shall be experienced in VLEO missions, typically 8km/s. In fact, the 1110s specific impulse signifies effective exhaust velocities in the range of 11km/s, therefore a net acceleration of 3km/s, which is yet not enough to counter the drag experienced at such altitudes, simulated around 26mN [1].

The high currents observed during testing, even at low discharge voltages, suggest that this technology is expected to operate at best at high powers, both for the discharge and the magnetic circuit, possibly above the kW range. Although further testing must be conducted to observe the effects this power increase has on increasing losses due to dissociative reactions possibly experienced during testing.

In order to exploit at best this technology, numerous improvements are suggested. The main problem encountered was due to cathode emitter degradation, resulting in low plasma densities in the cathode which would lead to instability of keeper voltage and quenching of the neutralizer discharge. Moreover, this technology proves inadequate both for the high currents reached during testing and the eventual presence of oxygen for complete air mixture testing. Therefore new technologies are suggested, employing different materials, such as lanthanium hexaboride, and with higher current limitations.

The pumping system struggled to keep background pressures low with the increased volume flow rate. The cryopumps were seen to rapidly saturate as temperatures of the cryopanels rose above 30K, almost 10K higher than usual operation. During nominal thruster operation with a steady 100 sccm nitrogen flow, pressures as high as 2.5×10^{-4} Torr were recorded, the puffing of the argon to ignite the degraded cathode did not help either. Not only such high pressures signify an increase in collisionality thus more electron mobility and reduction in ionization rate. It also reflects an unrealistic testing environment. As much as this research was centered around optimizing a design for efficient molecular ionization and not to validate this technology realistic operating conditions, the principal problem being the propellant composition and hypersonic inflow speed, much lower pressures are expected when operating in VLEO altitudes, therefore more efficient electron confinement can be expected.

More in depth studies are required on electron temperatures within the long channel configuration, in order to guarantee efficient ionization and limit dissociative reactions where possible. It is possible that this technology may evolve into maximizing the electron temperature, as to guarantee complete dissociation of all molecules and subsequent

ionization of the resulting atoms, this condition may lead to an increase in thrust and specific impulse, yet very high powers would be required and thus possibly lower efficiencies. Trade-off studies must be conducted to identify the ideal working condition.

More measurements must be conducted on the thrust stand in order to validate the trends observed in these first tests and reduce the errors and uncertainties linked to the observed mode drifts and instabilities, as well as understanding the causes.

What could possibly be the most interesting study has unfortunately not been conducted for the limited time and technology available, the variation of performance with mass flow rate. As previously mentioned, nitrogen mass flow rate was limited to 2.06mg/s during testing. This is an fundamental parameter in performance measurement, with increases expected at higher flow rates, and could constitute a big constraint to mission analysis and orbit selection. Lower mass flow rates can also be studied, as low as 70 (1.46mg/s), yet poorer performance is expected, with unsteady discharges that would easily quench.

7.1.2 Performance comparison

In order to evaluate the success of the modifications it is fundamental to compare the measured data to previous simulations and experiments with air-breathing Hall thrusters. Differently from previous experiments, in which Stanford's Z-70 as operated on an air-xenon mixture, the extension of the channel coupled to the enhanced ionization region, allowed the modified thruster to initiate and maintain a plasma discharge without the need of xenon and at lower powers. In fact, the Z-70 struggled to maintain a stable discharge when xenon flow was reduced under 0.16mg/s [34, 36].

Initial testing on Z-70 emphasized the inadequacy of nitrogen to serve as a propellant for electrostatic thrusters, as the efficiency dropped to 6% and thrust to 12.66mN with a 50%-50% air xenon mixture. After modifications performance was pushed to efficiencies over 16% and thrust values ranging from 20-22mN, highlighting the benefit of the modifications. These results are still low compared to typical xenon-operating Hall thrusters, with reference values of the latter ranging as high as 35mN thrust, 1800s specific impulse and 42% global efficiency.

The model presented in Section 4.2.1 predicts increased benefits for further extension of the chamber, as the ionization region is extended, molecular neutral ionization probability is increased, which would encourage additional development of this technology. It does not however, take into consideration dissociative reactions and wall losses that may increase as a result of the additional thruster length. The model simulates a mass utilization efficiency of $\eta_{\mathrm{u,real}} \approx 0.64$ as a result of the modifications, resulting in ion beam currents around 4.4A and discharge currents in the range of 5A, at 2mg/s nitrogen flow rate.

As a result, performance was computed and thrust levels of 29.7mN were simulated, with resulting specific impulses and global efficiencies respectively 1453.9s and 17%. These results are slightly higher than measured as a result of the wall losses and dissociative effects ignored by the model. ’

These reference value allow for an estimate of the real mass utilization efficiency, in fact, as the values of ion charge and mass are unaltered it is possible to say that:

$$\frac{\eta_{u,real}}{\eta_{u,model}} = \frac{I_{b,real}}{I_{b,rmodel}} \tag{7.1}$$

Hypothesizing that the electron beam current entering the thruster is 15% of the ion beam current[48], from a total discharge current of 2.7A as observed in Run 5, an ion beam current of 2.3A is obtained, from which it is possible to estimate the real mass utilization efficiency of $\eta_{\mathrm{u,real}} \approx 0.33$. It is evident that the dissociative effects and other losses result in an almost 50% loss in mass utilization efficiency.

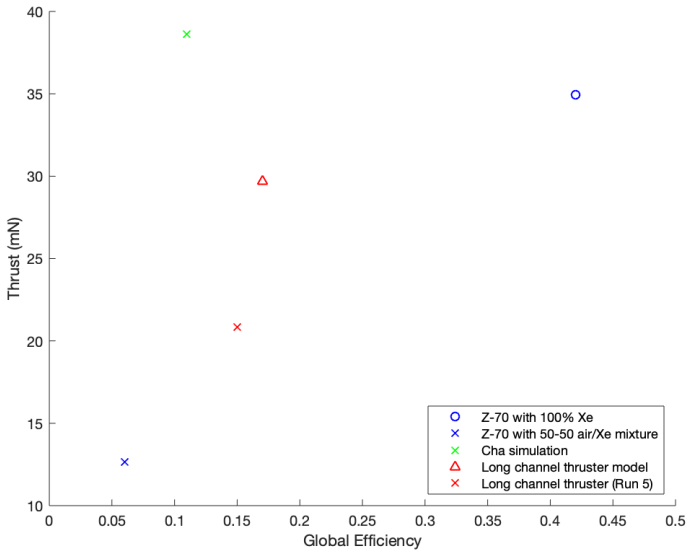

Figure 7.1: Performance comparison

More accurate simulations have been performed by Cha [35], in which hybrid Particle in Cell simulation codes have been used to model the effects of the extended thruster geometry and the relative magnetic field for the ionization of nitrogen molecules. This elaborated PIC model highlighted the benefits of the modifications, as plasma density increased over an order of magnitude compared to previous simulations with SHT geometry.

The simulation also attempted to estimate performance values. Comparing the measured results in Table 6.2 with these simulated values presented in Table 4.2, the latter seem to predict much higher currents and thrust values. In fact the simulation predicts thrust values of 38.6mN and anode currents of 16.5A for 2mg/s nitrogen mass flow rate.

The great currents simulated are a consequence of the difficulty to effectively model electron mobility throughout the channel, it is evident that the simulations predict an electron drift towards the anode much higher than experienced. In the PIC simulations studied [35], the mobility of electrons is implemented through a shear-based transport model. This is a semi-empirical model adopts two fitting parameters that attempts to simulate

electron transport along cross-field direction as an effect of collisions. The shear model is dependant on the inverse of the Hall parameter ω and defined as follows:

$$(\omega_{ce}\tau)_{\text{eff}}^{-1} = (\omega_{ce}\tau)_{\text{clas}}^{-1} + (\omega_{ce}\tau)_{\text{nw}}^{-1} + (\omega_{ce}\tau)_{\text{fluc}}^{-1}\left(\frac{1}{1+(Cs)^2}\right) \tag{7.2}$$

In which, $(\omega_{ce}\tau)_{\text{clas}}^{-1}$ is the effect of neutral collisions, $(\omega_{ce}\tau)_{\text{nw}}^{-1}$ is the near-wall term based on electron-wall collisions and $(\omega_{ce}\tau)_{\text{fluc}}^{-1}$ accounts for the transport due to fluctuations. Finally, the shear rate s is given by:

$$s = \frac{dv_{\text{e},\theta}}{dz} = \frac{dE_{\text{z}}/B_{\text{z}}}{dz} \tag{7.3}$$

Due to the lack of experimental data for the nitrogen Hall thrusters, the fitting parameters $(\omega_{ce}\tau)_{\text{fluc}}^{-1}$ and C were guessed to be similar to those fitted for xenon-optimized SHT and the following values were adopted:

- $(\omega_{ce}\tau)_{\text{fluc}}^{-1} = 5$
- $C = 2 \times 10^{-8}$

It is therefore evident that with the new experimental data acquired, new fitting can be done to the above parameters in order to correct previous simulations.

7.2 Future works and feasibility

Air-breathing electric propulsion is a promising yet far from mature technology. The possibility of orbiting at VLEO altitudes, by harnessing in situ resources of the atmosphere as propellant would allow numerous improvements in earth observation missions, intelligence, scientific and climate change research, internet and communication services and many more. The possibility of using unconventional gasses as propellant also allows dedicated systems to orbit around other planets by exploiting there atmospheres without the need for carrying extra fuel in the interplanetary transit.

In recent years numerous efforts have been made to advance and optimize this technology. Possibly the most notable study has been done by an ESA-SITAEL collaboration [1]. SITAEL has validated a VLEO testing environment through the use of a second Hall thruster (which they refer to as PFG) to generate a mass inflow to the primary air-breathing optimized thruster. The latter is placed on a thrust stand in order to measure the small thrust produced in such an extreme condition.

In the work of Andreussi et al [1], measured thrust values of 6mN, with a 4.7mg/s air mass flow rate generated by the PFG, are reported. As a result of the harsher working conditions, these results are much lower than those measured in this research and, even more importantly, they are lower than the simulated drag values of 26mN generated by their intake. This denotes the still inefficient design and the increased difficulty in ionizing

such a fast inflow, promoting the implementation of a long channel. In fact, this design would not only increase ionization probability and performance, but also allow for less compression by the air intake thus generate less drag.

Future evolutions of this technology would entail even longer channels, as the benefits of an increased ionization region are illustrated in Figures 4.10 and 4.11. To tailor this concept to the hypersonic inflow speeds encountered in VLEO operational orbits a Cylindrical Hall thruster geometry could be adopted, a concept of which is illustrated in Figure 7.2.

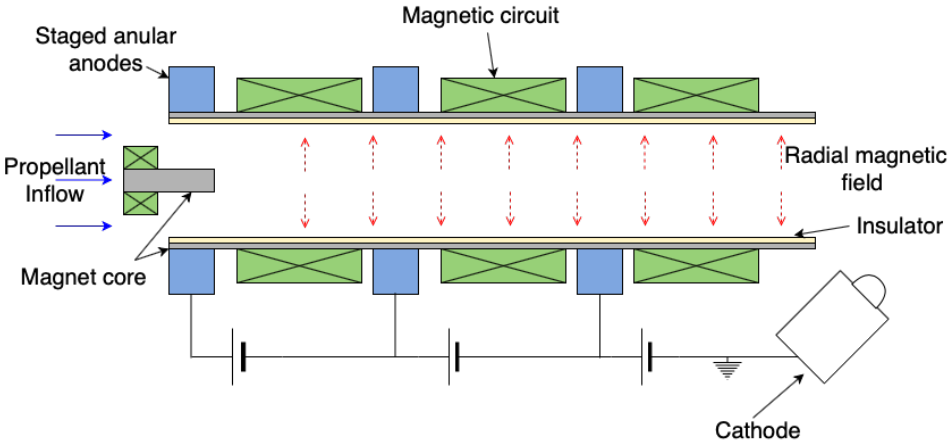

Figure 7.2: Long channel cylindrical Hall thruster concept

This evolution guarantees even more extended magnetic field regions, limiting the exposed chamber surface to reduce thruster erosion. Moreover, this would allow the removal of a gas distributor, feeding the propellant directly from the intake, thus the need to slow it down less resulting in a noticeable decrease in drag.

The staged annular anodes, placed at decreasing potentials from anode to cathode, would allow to apply higher potentials and extend the acceleration region together with the ionization. The potential drop can be optimized to achieve higher ion velocities which would reflect in higher thrust and specific impulses.

Extending the thruster can however prove counterproductive after a certain length. Increasing chamber length results in an inevitable increase in losses due to collision with walls. Not only do these decrease performance, but can result in greater thruster erosion and reduced life times. This however is balanced by the lighter weight of the nitrogen molecules, thus lower momentum when impacting with walls.

Moreover, longer channel wall signify increased secondary electron emission from walls. This phenomenon is difficult to model, highly dependant on material choice and can cause instabilities and unwanted variations in electron energy. A final effect associated to a longer magnetic field is the increased plume divergence as a result of more magnetized ions, not only would this result in decreased performance but plume impingement with the satellite must be avoided for mission success.

Bibliography

[1] Andreussi, Tommaso; Ferrato, Eugenio; Giannetti, Vittorio; Piragino, Antonio; Cifali, Gianluca; Andrenucci, Mariano and Paissoni, Christopher A. *Development Status and Way Forward of SITAEL's Air-breathing Electric Propulsion.* AIAA Propulsion and Energy Forum, 2019

[2] Di Cara, Davina; Gonzalez del Amo, José; Santovincenzo, Andrea; Carnicero Dominguez, Bernardo; Arcioni, Marco; Caldwell, Andrew and Roma, Ilaria. *RAM Electric Propulsion for Low Earth Orbit Operation: an ESA study.* 30th International Electric Propulsion Conference, 2007

[3] Sutton, George P. and Biblarz, Oscar. *Rocket Propulsion Elements.* John Wiley & Sons Inc., 2017.

[4] Wertz, J. R. and Larson W. J. *Space Mission Analysis and Design.* Microcosm Press, 1999.

[5] Choueiri, Edgar. *A Critical History of Electric Propulsion: The First Fifty Years (1906-1956).* Princeton University, 2004.

[6] Hill, Philip G., and Peterson, Carl R. *Mechanics and Thermodynamics of Propulsion.* Addison-Wesley Longman, 2010.

[7] Jahn, Robert G., and Choueiri, Edgar. *Electric Propulsion.* Encyclopedia of Physical Science and Technology, 2003

[8] Lev, Dan; Myers, Roger M.; Lemmer, Kristina M.; Kolbeck, Jonathan; Koizumi, Hiroyuki and Polzin, Kurt *The technological and commercial expansion of electric propulsion.* Acta Astronautica, 2019.

[9] Tikhonravov, Mikhail K. *Works on Rocket Technology by E. K. Tsiolkovsky.* Publishing House of the Defense Ministry, Moscow, 1947.

[10] Goddard, Robert. H. *Method and means for producing electrified jets of gas.*. US Patent No. 1,163,037. Application filed October 1917, granted December 1920.

[11] Oberth, Hermann. *Wege zur Raumschiffahrt* (Ways to Spaceflight). Druck und Verlag von R. Oldenbourg, Munich and Berlin, 1929.

[12] Stuhlinger, Ernst. *Ion Propulsion for Space Flight.* McGraw-Hill, New York, 1964.

[13] Cybulski, Ronald J.; Shellhammer, Daniel M.; LoveII, Robert R.; Domino, Edward J. and Kotnik, Joseph T. *Results From SERT 1 Ion Rocket Flight Test.* NASA Technical Note D2718, 1965.

[14] Morozov, A. I. *Introduction to Plasma Dynamics.* CRC Press, 2013.

[15] Morozov, A. I. *The Conceptual Development of Stationary Plasma Thrusters.* Plasma Physics Reports, 2003.

[16] *Hall-effect thruster webpage*: https://en.wikipedia.org/wiki/Hall-effect_thruster#History

[17] Jahn, Robert G. *Physics of Electric Propulsion.* McGraw-Hill, 1968.

[18] Chen, Francis F. *Introduction to Plasma Physics and Controlled Fusion.* Third Edition. Springer International Publishing Switzerland, 2016

[19] Goebel, Dan M. and Katz, Ira. *Fundamentals of Electric Propulsion: Ion and Hall Thrusters.* JPL Space Science and Technology Series, 2008

[20] Alman, Darren A.; Rovery, Joshua L.; Stubbers, Robert A.; and Jurczyk, Brian E. *Hall Thruster Electron Mobility Investigation using Full 3D Monte Carlo Trajectory Simulations.* 30th International Electric Propulsion Conference, 2007

[21] Zhurin, Viacheslav V.; Kaufman, Harold R. and Robinson, Raymond S. *Physics of Closed Drift Thrusters.* Plasma Sources Science and Technology, 1998.

[22] Keidar, Michael and Beilis, Isak I. *Electron Transport Phenomena in Plasma Devices with E×B Drift.* Special Issue on Nonlocal, Collisionless Electron Transport in Plasmas, 2006.

[23] Choueiri, Edgar. *Fundamental Difference between the Two Variants of Hall Thrusters: SPT and TAL.* 37th Joint Propulsion Conference and Exhibit, 2001.

[24] Hofer, Richard R.; Jankovsky, Robert S. and Gallimore, Alec D. *High-Specific Impulse Hall Thrusters, Part 1: Influence of Current Density and Magnetic Field.* Journal of Propulaion and Power Vol.22, 2006.

[25] Hofer, Richard R. *Development and Characterization of High-Efficiency, High-Specific Impulse Xenon Hall Thrusters.* Ph.D. Dissertation, Aerospace Engineering, University of Michigan, Ann Arbor, Michigan, 2004.

[26] Young, Christopher V.; Cha, Eunsun; Fernandez, Eduardo and Cappelli, Mark A. *Comparison of Hall Thruster Ion Dynamics Between Laser Induced Fluorescence Measurements and a 2-D Hybrid Simulation.* 34th International Electric Propulsion Conference, 2015

[27] Kim, Sang-Wook and Gallimore, Alec D. *Plume Study of a 1.35kW SPT-100 Using an ExB Probe.* Journal of Spacecraft and Rockets Vol.39, 2002

[28] Kim, Vladimir *Main Physical Features and Processes Determining the Performance of Stationary Plasma Thrusters*. Journal of Propulsion and Power Vol.14, 1998

[29] Walsh, Jonathan A. and Berthoud, Lucy *Reducing spacecraft drag in Very Low Earth Orbit through shape optimisation*. 7th European Conference for Aeronautics and Aerospace Sciences, 2017

[30] Welle, Richard P. *Propellant Storage Considerations for Electric Propulsion*. 22nd International Electric Propulsion Conference, 1991.

[31] Tverdokhlebov, Oleg S. and Semenkin, Alexander V. *Iodine propellant for electric propulsion - To be or not to be*. 37th Joint Propulsion Conference and Exhibit, 2001.

[32] Betzendahl, Richard. *The 2014 Rare Gases Market Report*. CryoGas International, 2014.

[33] Lev, Dan R.; Emsellem, Gregory D. and Hallock, Ashley K. *The Rise of the Electric Age for Satellite Propulsion*. New Space journal, 2017.

[34] Gurciullo, Antonio. *Electric Propulsion Technologies for Enabling the use of Molecular Propellants*. Ph.D. Dissertation, Faculty of Engineering and Physical Sciences, University of Surrey, Guilford, Surrey, 2018.

[35] Cha, Eunsun. *Dynamic Models of Electron Transport in Hall Thruster Simuations*. Ph.D. Dissertation, Mechanical Engineering, Stanford University, Stanford, California, 2015.

[36] Gurciullo, Antonio; Fabris, Andrea L. and Cappelli, Mark A. *Ion plume investigation of a Hall Effect Thruster operating with Xe/N_2 and Xe/air mixtures*. Journal of Physics D: Applied Physics, 2019.

[37] Hwang, W.; Kim, Y.K. and Rudd, M. E. *New Model for Electron-Impact Ionization Cross Sections of Molecules*. Journal of Chemical Physics, 1996.

[38] Saporoschenko, Mykola. *Ions in Nitrogens*. Physical Review, 1958.

[39] *Space engineering - Space environment*. Standard ECSS-E-ST-10-04C, ESA-ESTEC, Netherlands, 2008.

[40] Picone, J. M., Hedin, A. E., Drob, D. P., and Aikin, A. C. *NRLMSISE-00 empirical model of the atmosphere: Statistical comparisons and scientific issues*. Journal of Geophysical Research: Space Physics, 2002.

[41] Schönherr, Tony; Komurasaki, Kimiya and Herdrich, Georg. *Analysis of Atmosphere-Breathing Electric Propulsion*. 33rd IEPC, Washington, 2013.

[42] Romano, Francesco. *System Analysis and Test Bed for an Air-Breathing Electric Propulsion System*. Master Thesis, Aerospace Engineering, Università degli Studi di Padova, Padova, 2014.

[43] Jackson, Stephen W. *Design of an Air-Breathing Electric Thruster for CubeSat Applications*. Graduate Thesis, Aerospace Engineering, University of Colorado Boulder, Colorado Springs, 2017.

[44] Fernandez, Eduardo; Cappelli, Mark A., and Mahesh, K. *2D Simulations of Hall Thrusters*. Center for Turbulance Research Annual Research Briefs, 1998.

[45] Scharfe, Michelle K.; Gascon, Nicolas; Cappelli, Mark A. and Fernandez, Eduardo. *Comparison of hybrid Hall thruster model to experimental measurements*. Physics of Plasmas, 2006.

[46] Pekker, L. and Keidar M. *Analysis of Air Breathing Hall Effect Thruster*. AIAA Plasmadynamics and Laser Conference, 2011.

[47] Warner, Noah Z. *Theoretical and Experimental Investigation of Hall Thruster Miniaturization*. PhD dissertation, Massachusetts Institute of Technology, Boston, 2007.

[48] Boeuf, Jean Pierre. *Physics and modeling of Hall thrusters*. Journal of Applied Physics, 2017.

[49] Straub H.C., Renault P., Lindsay B. G., Smith K. A., and Stebbings R. F. *Absolute Partial Cross Sections for Electron-Impact Ionization of* H_2, N_2 *and* O_2 *from Threshold to 1000 eV*. Physical Review A, 1996.

[50] MacDonald-Tenenbaum, Natalia; Pratt, Quinn; Nakles, Michael; Pilgram, Nickolas; Holmes, Michael and Hargus, William A. Jr. *Background Pressure Effects on Ion Velocity Distributions in an SPT-100 Hall Thruster*. Journal of Propulsion and Power, 2019.

[51] Hargus, William A. Jr. *Investigation of the Plasma Acceleration Mechanism within a Coaxial Hall Thruster*. Report N0. TSD-130 Sponsored by US Air Force, 2001.

[52] Smith, Andrew W. *Field Structure and Electron Transport in the Near-Field of Coaxial Hall Thrusters*. Ph.D. Dissertation, Mechanical Engineering, Stanford University, Stanford, California, 2010.

[53] Marcovati, Andrea *Z-70 Hall Thruster Performance Analysis: Experimental Thrust and Plasma Measurements*. MSc Thesis, Aerospace Engineering, Politecnico di Milano, Milan, Italy, 2015.

[54] Young, Christopher V. *The Stanford Diverging Cusped Field Thruster: Design, Construction and Initial Testing*. BSc Thesis, Engineering Physics, Stanford University, Stanford, California, 2010.

[55] Young, Christopher V. *Dynamics of Plasma Discharges used for Space Propulsion*. PhD Dissertation, Mechanical Engineering, Stanford University, Stanford, California, 2016.

[56] Ellis, George. *Control System Design Guide (Fourth Edition)*. Butterworth-Heinemann, 2012.